Gyroscopic dampers in offshore wind turbines

The design of a support structure for a novel turbine technique and the effects of gyroscopic dampers on the dynamic response

Master Thesis

F.M. van Ingen

Delft University of Technology

Gyroscopic dampers in offshore wind turbines

The design of a support structure for a novel turbine technique and the effects of gyroscopic dampers on the dynamic response

by

Floris Matthijs van Ingen

To obtain a Masters degree in Offshore and Dredging Engineering

Supervisors Delft Offshore Turbine:	ing. David Tiemens
	ir. Rob Atkinson
Supervisors TU Delft:	prof. dr. Andrei Metrikine
	dr. ir. Peter Meijers
Institution:	Delft University of Technology
Place:	Delft, 2024

Preface

With the completion of this thesis, my time as a student at the Technical University Delft comes to an end. A period of my life that makes me who I am today. A period of growth, self-development and the discovery of the beauties of the world and everyone on it. A period of loss, sorrow and recognition of the fragility and cruelty of the world. The time it took to complete this thesis has been marked by the latter.

Because of that, it makes me especially proud to have finally completed it. All in my own way. Hoping, this marks a moment to reflect and move forward.

This journey would not have been possible without the many remarkable people in my life, whose support and kindness have made all the difference.

From Delft Offshore Turbine, where Rob Atkinson and David Tiemens have been extremely patient with me. Helping me with wise and tailored advice.

From the TU Delft, where Andrei Metrikine, Mamin Masturi and especially Peter Meijers have given me the opportunity to complete this final step in my own unconventional manner.

My dad, sister, brother and girlfriend, for your unconditional love and support along the way. You helped me to keep my head above the water for a very long time. All, during the most difficult period of our lives.

My friends, who kept making me smile. The best remedy to overcome seemingly never-ending dark times and make them bright again.

And finally, my mother. Who made sure I will never forget that she is proud of me. Who made me believe in myself, something that I will carry on for the rest of my life. Who's love is bottomless.

Mam, ik hou van je. Deze is voor ons.

F.M. van Ingen
Delft, October 2024

Abstract

The rise in global energy demand, combined with the imperative to reduce CO2 emissions, has driven significant investments in renewable energy technologies. Offshore wind energy is a critical part of this transition, given its potential to provide large-scale clean energy. However, one of the main challenges facing the offshore wind industry is the high levelised cost of energy (LCOE), driven primarily by the costs of operation, maintenance, and the construction of support stuctures and foundations. Reducing the LCOE is essential to make offshore wind energy more competitive. Innovations in turbine design and installation techniques can play a key role in achieving this goal. A good example is the introduction of slipjoint connections, which simplify the installation process and reduce material use. Similarly, new turbine concepts, such as the hydraulic pump generator by Delft Offshore Turbine (DOT), aim to reduce the weight and complexity of the rotor nacelle assembly (RNA), potentially cutting both maintenance costs and structural demands.

This thesis investigates the effects of the lighter RNA, due to the innovative hydraulic generator pump, on the support structure. The DOT turbine employs a hydraulic pump directly driven by the rotor, eliminating the need for a gearbox and reducing the RNA weight by up to 50%. Moreover, the hydraulic pump uses significantly less space in the nacelle. This reduction provides an opportunity to enhance the support structure and incorporate dampers in the nacelle to mitigate vibrations caused by environmental loads. In the second half of this research, the potential of a gyroscopic damper to improve the dynamic response of wind turbines subjected to wind and wave loads is explored. The focus lays on the reduction of the undamped side-to-side vibrations.

The research objectives include evaluating the impact of the lighter topside on the design of the support structure and evaluating the effectiveness of gyroscopic dampers in reducing fatigue and wave-induced vibrations. To this end a comparison between a conventional wind turbine support structure and the lighter DOT design is made. The dynamic response of the system is analyzed through ultimate limit state (ULS) and fatigue limit state (FLS) evaluations, using simplified, but accurate, dynamic models. In addition, the performance of the gyroscopic damper is modeled and tested to determine its ability to reduce the steady-state amplitude of side-to-side vibrations.

The results demonstrate that the lighter topside of the DOT turbine reduces steel use for the support structure by 13%, compared to the conventional support structure. Furthermore, the implementation of a passive gyroscopic damper without any damping elements demonstrates a frequency skipping tool that can easily be tuned by altering the gyricity of the spinning disk. In addition to that, when a damping element is added to the gyrostabiliser, a positive effect in damping the side-to-side vibrations is observed. Compared to the undamped case, a reduction of more than 90% of the maximum bending stress at the mudline is achieved. Additionally, due to the added weight and the ability of a spinning disk to resist changing its orientation, the natural frequency of the total system lowers. A sensitivity analysis of gyricity and mass variations confirms the potential benefits of such a damper to improve the structural integrity and extend the lifetime of the turbine. The findings suggest that further optimization of the damper configuration could lead to more reliable and cost-effective offshore wind turbines.

The thesis concludes with recommendations for future research, including the exploration of the effects of lighter topsides on the support structure and the implementation of gyrostabilisers in larger turbines, deeper-water and floating turbine applications.

Contents

Preface i

Abstract ii

Nomenclature v

List of Figures viii

List of Tables x

1 Introduction 1
- 1.1 DOT turbine concept . . . 2
  - 1.1.1 Hydraulic pump. . . . 4
  - 1.1.2 Ripple effect . . . 4
- 1.2 Research objectives . . . 4
- 1.3 Opportunity for dampers . . . 4
- 1.4 Report set-up . . . 5

2 Design Basis 6
- 2.1 Load cases . . . 6
- 2.2 Environmental data . . . 7
  - 2.2.1 Aerodynamic data . . . 8
  - 2.2.2 Hydrodynamic data . . . 11
- 2.3 Soil characteristics . . . 11

3 Support Structure Design 13
- 3.1 Target frequency . . . 14
- 3.2 Initial pile diameters . . . 15
  - 3.2.1 Aerodynamic loading. . . . 15
  - 3.2.2 Hydrodynamic loading . . . 15
- 3.3 Embedded pile length . . . 16
- 3.4 Calculation of natural frequency . . . 17

4 Limit State Analysis 21
- 4.1 Ultimate Limit State . . . 21
  - 4.1.1 Yield check . . . 21
  - 4.1.2 Global buckling check . . . 25
  - 4.1.3 Results ULS analysis . . . 27
- 4.2 Fatigue Limit State . . . 28
  - 4.2.1 Dynamic fatigue model . . . 28
  - 4.2.2 Aerodynamic damping . . . 31
  - 4.2.3 Wave data input FLS . . . 31
  - 4.2.4 Amplitude Frequency Response Function. . . . 32
  - 4.2.5 Fatigue calculation . . . 33
  - 4.2.6 Fatigue Limit State Results and Conclusions . . . 34

5 Gyroscopic Dampers 37
- 5.1 Gyroscopic effects . . . 38
- 5.2 Configuration of a gyrostabiliser . . . 39

6 Gyrostabiliser Modelling **41**
6.1 Support structure . . . 41
6.2 RNA and gyrostabiliser . . . 42
6.3 Systems interaction . . . 45
6.4 Forcing input . . . 45

7 Results **46**
7.1 Gyrostabiliser parameters . . . 47
7.2 Sensitivity analysis . . . 48
7.2.1 Gyricity . . . 49
7.2.2 Mass . . . 50
7.3 Damped gyrostabiliser . . . 51

8 Conclusions and Recommendations **55**
8.1 Conclusions . . . 55
8.1.1 Lighter topside . . . 55
8.1.2 Gyrostabiliser . . . 56
8.2 Recommendations . . . 58

References **61**

A Derivation of critical wave loads **62**

B Derivation of rotational matrix **64**

Nomenclature

Abbreviations

Abbreviation	Definition
AEY	Annual energy yield
AFRF	Amplitude frequency response function
ATMD	Active tuned mass damper
CO2	Carbon dioxide
COE	Cost of energy
CPT	Cone penetration test
DFF	Design fatigue factor
DOT	Delft Offshore Turbine
EOG	Extreme operating gust
ESS	Extreme sea state
ETM	Extreme turbulence model
EWH	Extreme wave height
FLS	Fatigue limit state
JONSWAP	Joint North-Sea wave project
LAT	Lowest astronomical tide
LCD	Liquid column damper
LCOE	Levelised cost of energy
MSL	Mean sea level
NEA	Netherlands Enterprise Agency
NTM	Normal turbulence model
O&M	Operation and maintenance
OWT	Offshore wind turbine
PTMD	Passive tuned mass damper
RNA	Rotor nacelle assembly
SFRF	Stress frequency response function
ULS	Ultimate limit state

Symbols

Symbol	Definition	Unit
c	Blade cord length	[m]
c_{aero}	Aerodynamic damping coefficient	[-]
C_{my}	Moment factor for buckling	[-]
C_T	Thrust coefficient	[-]
D	Accumulated fatigue damage	[-]
DFF	Design fatigue factor	[-]
D_{MP}	Diameter of monopile	[m]
D_R	Rotor diameter	[m]
$D_{SJ,b}$	Diameter of slipjoint bottom	[m]
$D_{SJ,t}$	Diameter of slipjoint top	[m]
$D_{T,b}$	Diameter of tower bottom	[m]
$D_{T,t}$	Diameter of tower top	[m]
F_x	Lateral force in x-direction	[N]

Symbol	Definition	Unit
g	Gravitational acceleration	[m/s²]
H_{m0}	Significant wave height	[m]
H_{max}	Maximum wave height	[m]
I_j	Segment second moment of area	[m⁴]
$J_{RNA,x}$	Moment of inertia of RNA (x-axis)	[m⁴]
$J_{RNA,y}$	Moment of inertia of RNA (y-axis)	[m⁴]
k	Number of stress blocks	[-]
K_L	Lateral spring coefficient	[GN/m]
K_{LR}	Coupling spring coefficient	[GN]
K_{LT}	Lateral spring stiffness	[GN/m]
K_R	Rotational spring coefficient	[GNm/rad]
k_{soil}	Soil stiffness	[N/m]
k_{yy}	Coupling term for bending moments	[-]
L	Lagrangian	[-]
L_{Buck}	Buckling length	[m]
L_{emb}	Embedded length monopile	[m]
L_M	Monopile length	[m]
L_S	Slipjoint length	[m]
L_T	Tower length	[m]
m	Negative inverse slope of the S-N curve	[-]
M_d	Mass gyroscopic disk	[kg]
M_{RNA}	Mass of rotor nacelle assembly	[kg]
M_y	Moment around y-axis	[Nm]
$\Delta M_{y,Ed}$	Moment due to the shift of the centroidal axis	[Nm]
$M_{y,Rk}$	Moment resistance	[Nm]
$M_{z,Rk}$	Moment resistance about z-axis	[Nm]
m_{top}	Mass of topside	[kg]
N	Normal force	[N]
N_b	Number of blades	[-]
N_{cr}	Euler buckling normal force	[N]
N_{Ed}	Design normal force	[N]
N_i	Number of stress cycles to failure at a constant stress range $\Delta\sigma_i$	[-]
n_i	Number of stress cycles for certain stress range	[-]
R	Radius of gyroscopic disk	[m]
P_r	Rated power	[MW]
$T_{p,Hmax}$	Peak wave period associated with H_{max}	[s]
u_c	Current speed	[m/s]
$U_{10,av}$	10-min average wind speed at 100m	[m/s]
U_R	Rated wind speed	[m/s]
U_Z	Wind speed at height Z	[m/s]
W	Elastic section modulus	[m⁴]
V	Topside for-aft horizontal displacement	[m]
$\dot{V}$	Topside for-aft horizontal velocity	[m/s]
$\ddot{V}$	Topside for-aft horizontal acceleration	[m/s^2]
V_Ω	Rotational speed of blade element	[rad/s]
Z_{LAT}	Lowest astronomical tide	[m]
Z_{MSL}	Mean sea level	[m]
α	Wind shear parameter	[-]
η	Fatigue usage factor (1/DFF)	[-]
γ_e	Environmental safety factor	[-]
γ_m	Material factor for S355 steel	[-]
γ_s	Wave spreading factor	[-]

Symbol	Definition	Unit
γ_{M1}	Partial safety factor for resistance of monopiles to instability	[-]
λ	Eigenvalue	[-]
μ_y	Additional term in buckling equations	[-]
ρ	Density	[kg/m^3]
ρ_a	Air density	[kg/m^3]
ρ_m	Displacement at mudline	[m]
$\Delta\sigma_i$	Stress range	[Pa]
σ_{VM}	Von Mises stress	[Pa]
τ	Torque	[Nm]
τ_{xy}	Shear stress	[Pa]
θ	Rotation gyroscopic disk around x-axis	[rad]
θ_m	Rotation at mudline	[°]
ϕ_x	Rotation of topside around x-axis	[rad]
$\dot{\phi}_x$	Rotational velocity of topside around the x-axis	[rad/s]
$\ddot{\phi}_x$	Rotational acceleration of topside around the x-axis	[rad/s^2]
χ	Stiffness ratio between tower and monopile	[-]
χ_z	Reduction factor due to flexural buckling	[-]
ψ	Rotation gyroscopic disk around y-axis	[rad]
ω_w	Wave frequency	[rad/s]
Ω_d	Gyricity disk	[rad/s]

List of Figures

1.1 Yearly average wind speed at 100m height [3] . . . 1
1.2 Distribution of LCOE for offshore wind turbines [5] . . . 2
1.3 Depiction of a geared drivetrain . . . 2
1.4 Schematic overview novel hydraulic DOT pump . . . 3
1.5 Schematic overview of cross-section hydraulic pump . . . 4

2.1 Exact location of OWT in Prinses Amalia Wind Park - source: www.noordzeeloket.nl . . 6
2.2 Power curve of DOT hydraulic pump generator turbine . . . 8
2.3 Average annual yield for several hub heights . . . 9
2.4 Wind speed profile representation . . . 9
2.5 Vertical wind speed profile, with hub height region . . . 10
2.6 Schematic resemblance OWT with equivalent springs . . . 11

3.1 Grouted (left), bolted (middle) and slip joint connection [4] . . . 13
3.2 Frequency diagram . . . 14

4.1 Schematic ULS analysis model . . . 22
4.2 Displacement DOT turbine over full length - ULS case . . . 24
4.3 Moment and shear force DOT turbine - ULS case . . . 25
4.4 Buckling curves . . . 26
4.5 Dynamic model FLS . . . 29
4.6 Joint scatter diagram HKN *(2005-01-01 - 2016-01-01)* . . . 31
4.7 Horizontal displacement topside conventional turbine . . . 32
4.8 Absolute horizontal displacement topside . . . 33
4.9 Stress Frequency Response Function - 1.5m wave . . . 34
4.10 S-N curves for steel in seawater [32] . . . 34
4.11 SFRF side-to-side motion - 1.5m wave . . . 35
4.12 support structure modeshapes . . . 36
4.13 SFRF for different heights above the mudline . . . 36

5.1 Schematics of an aviation instrument using a gyroscope . . . 38
5.2 Visualization of gyroscopic precession due to a torque . . . 39
5.3 gyrostabiliser configuration . . . 39

6.1 Simplified support structure-RNA model . . . 41
6.2 Schematic representation of the 4 degrees of freedom of the flywheel . . . 42
6.3 Topview of flywheel . . . 43
6.4 Joint occurance table of wave direction (WD) and wind-misalignment . . . 45

7.1 Top-view of incoming wave . . . 46
7.2 Stress Frequency Response Functions in side-to-side direction . . . 47
7.3 Results in for-aft direction . . . 48
7.4 Stress Frequency Response Function gyricity alteration | side-to-side direction . . . 49
7.5 Maximum bending stress for different gyricity configurations | side-to-side direction . 49
7.6 Transferred moment from nacelle to gyrostabiliser . . . 50
7.7 Stress Frequency Response Function mass alteration | side-to-side direction . . . 51
7.8 Stress Frequency Response Function - gyricity alteration damped 5000kg gyrostabiliser| side-to-side direction . . . 52

7.9 Stress Frequency Response Function - gyricity alteration damped 7000kg gyrostabiliser| side-to-side direction . . . 52
7.10 Maximum bending stress for different gyricities of damped gyrostabiliser | side-to-side direction . . . 53
7.11 θ frequency response plot . . . 53
7.12 Visualization of linearisation . . . 54

8.1 Stress Frequency Response Function gyricity alteration damped 7000kg gyrostabiliser| side-to-side direction . . . 57

A.1 Wake amplification factor for smooth (solid line) and rough (dotted line) roughness . . 63

B.1 Topview of flywheel . . . 64

List of Tables

1.1 Novel turbine characteristics . . . 3

2.1 MetOcean data Prinses Amalia Wind Park . . . 8
2.2 Soil parameters . . . 12

3.1 ULS load combinations . . . 16
3.2 Soil and spring parameters . . . 16
3.3 Input parameters OWTs for validation . . . 18
3.4 Measured and calculated frequencies . . . 19
3.5 Parameters support structure . . . 19

4.1 ULS results. **below mudline* . . . 27
4.2 Results FLS analysis . . . 35

6.1 Moments of inertia topside . . . 44

8.1 Parameters support structure . . . 56
8.2 Results ULS analysis. **with respect to mudline* . . . 56
8.3 Results FLS analysis . . . 56

1 Introduction

The rise of the global energy demand together with the goals on reducing CO2-emissions, has encouraged organizations to invest in renewable energy sources. The goal for the world to have a net zero emission in 2050 would mean a 37 gigatonnes (Gt) reduction of annual emissions. That is, an increase of 79% in the worldwide share of renewable energy [1]. The Paris agreement states that this is compatible with the target of a global temperature increase of 1.5°C, required to keep the environment from being irreversibly damaged. To meet these sustainability goals, the expansion and improvement of feasible low-carbon technologies is of the highest priority. Offshore wind is a compelling example of a fast-developing technology that is prone to contribute to these goals.

Renewable energy sources, such as wind, acquire a vast potential as it is a clean and unlimited source of energy. The offshore wind industry is one the largest and fastest growing renewable energy sources and has been proven to greatly contribute to the transition from fossil fuels to non-emitting sources. This is mainly due to the higher and more constant wind climate at seas compared to the land climate, see figure 1.1. Offshore wind turbines (OWTs) have the potential to produce much more energy than their terrestrial counterparts. The potential energy contained in offshore sites around the world is more than 10 times the global energy demand in 2040 [2]. This, together with the reduced visual horizon pollution caused by the onshore turbines, makes them a logical investment for countries that strive to produce and use more green energy.

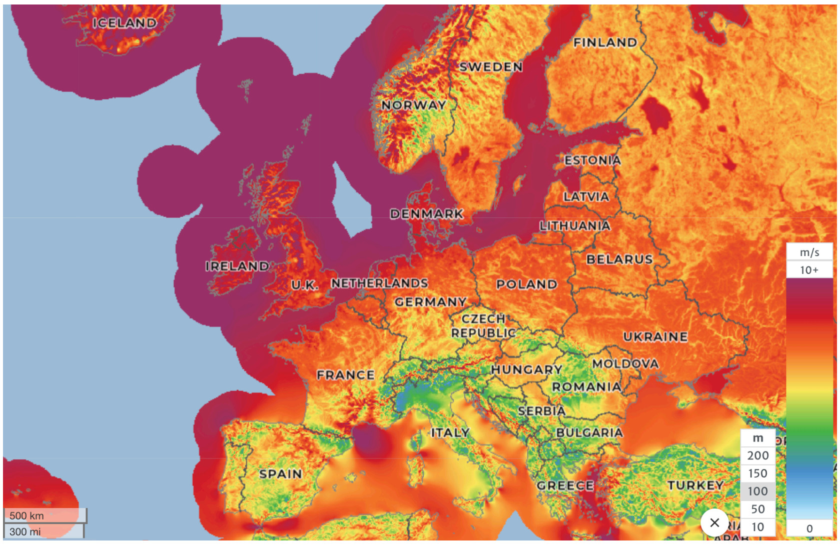

Figure 1.1: Yearly average wind speed at 100m height [3]

The biggest drawback of offshore wind farms is the high cost of energy. To compare different energy harvesting techniques the levelised cost of energy (LCOE) is introduced. A number that includes the total investment costs, the costs of operation and maintenance and the earnings over the lifetime of the turbine. The distribution of the components over the lifespan of the turbine is shown in figure 1.2, where we see that the biggest contributors to the LCOE are the operation and maintenance (O&M), turbine and support structure & foundation. Improvement of reliability and therefore reducing maintenance costs has a significant impact on the LCOE. A lower LCOE will make it more attractive to construct offshore wind farms. New techniques and optimizations within the offshore wind industry are realised frequently to reduce the LCOE and accelerate the sustainable energy transition. An example of a method to lower the LCOE is to apply smarter installation techniques. A distinctive example of this is the slip joint [4], a connection method between the support structure and the turbine to save costly installation time and materials. Section 3 in this thesis provides the reader with more information regarding this technique.

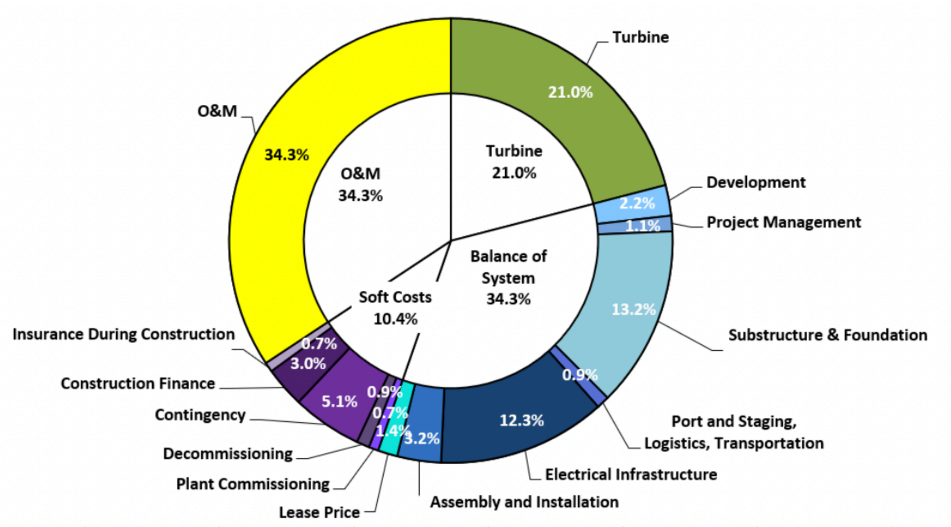

Figure 1.2: Distribution of LCOE for offshore wind turbines [5]

1.1. DOT turbine concept

Currently, a large amount of new bottom founded offshore wind turbines are placed all over the world. These all have approximately the same design and used technology, which originated from the smaller onshore turbines. As the turbines went offshore and grew bigger over the years - and are expected to scale more in the upcoming years - it is foreseen that the weight of the top of the turbine will become too large for a feasible design. This is mostly a function of the volume and weight of the gearbox needed to transfer the energy from the rotor into a low torque and high speed rotation in the generator [6], depicted in figure 1.3. Therefore, new turbine designs with a variety of different working principles are developed on regular basis. One of these is the patented hydraulic pump design of Delft Offshore Turbine (DOT), depicted in figure 1.4.

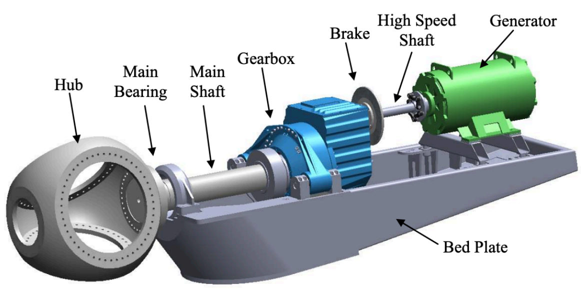

Figure 1.3: Depiction of a geared drivetrain

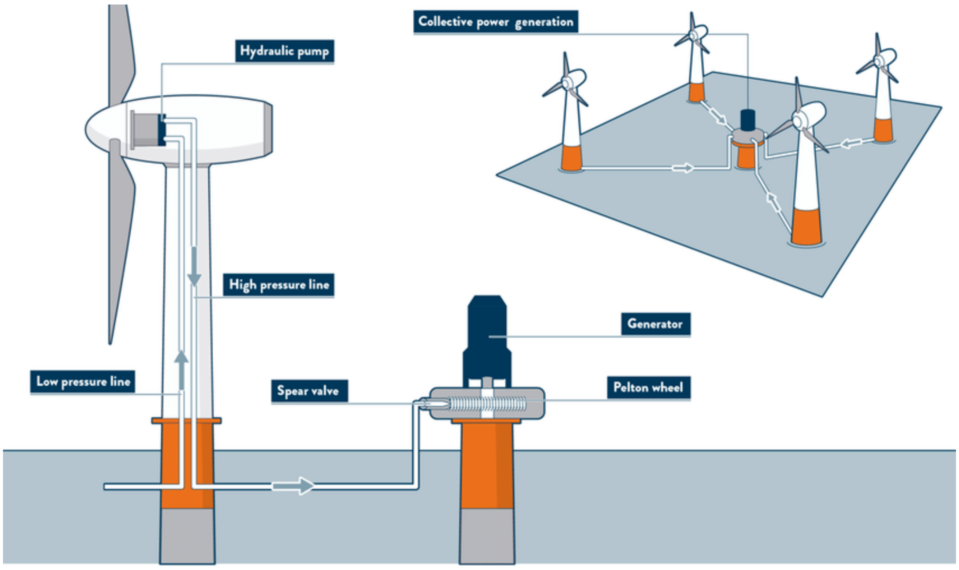

Figure 1.4: Schematic overview novel hydraulic DOT pump

The idea uses one hydraulic pump directly connected to the slowly rotating rotor, replacing high maintenance components as the gearbox and generator all together, while saving up to 50% of the original weight of the rotor nacelle assembly (RNA). The hydraulic pump pumps up seawater through the low pressure line and pressurizes is in the hydraulic pump. The electricity is generated by a separate generator attached to a Pelton wheel. This method of energy generation lends itself to design a configuration where several OWTs can interact with a collective power generator. An overview of the relevant RNA parameters of the turbine are shown in table 1.1.

Table 1.1: Novel turbine characteristics

Parameter	Symbol	Value	Unit
Rated power	P_r	2.5	MW
Rated wind speed	U_r	13	m/s
Rotor diameter	D_R	100	m
Mass hydraulic pump	m_{pump}	26	t
Mass nacelle	m_{nac}	18	t
Mass hub	m_{hub}	20	t
Mass blades	m_{blades}	9.1	t

1.1.1. Hydraulic pump

The hydraulic pump pressurizing the water via pistons. The cross-section of the pump is shown in figure 1.5, where the orange parts are the pistons. The outer grey cam ring transfers the rotational energy of the rotor to the upward motion of the cylinders. These cylinders pressurize the water when being compressed and suck in the water when being decompressed. This is the working principle of the rotary piston hydraulic pump.

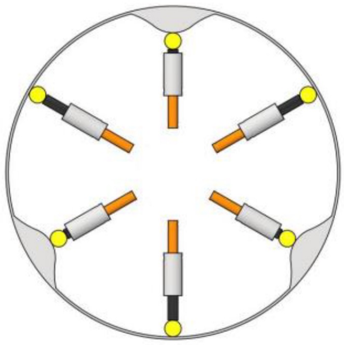

Figure 1.5: Schematic overview of cross-section hydraulic pump

1.1.2. Ripple effect

The compressing and decompressing of the cylinders in the pump generate a ripple effect within the system with a frequency of approximately 18Hz at rated power. This frequency is far from the expected natural frequencies of the system, so no excitation from this ripple effect will be expected. The approximation of the magnitude of the ripple is 2-5% of the total generated energy. Based on these two parameters, it is not expected that the ripple effect has a significant effect on the structural integrity of the system. Therefore, it will not be integrated in this research.

1.2. Research objectives

The optimization quest of the offshore wind turbine is constantly going on. The DOT turbine concept contributes to this by innovating the generator and aiming for a more reliable system. In addition to that, the lighter topside has a positive influence on the amount of material required for a structurally integer support structure. Besides this it gives the opportunity to utilize a damper in the topside, due to weight and size benefits.

Hence, the objectives of this research thesis are to firstly analyze the extend of effects of the lighter topside on the design of the support structure. And successively, to analyse the feasibility of a damper in the form of a gyroscope as these effects are fairly unknown. This results in the following research questions:

> *"What are the effects of a lighter topside on the support structure of a bottom founded offshore wind turbine?"*
>
> *"How effective are gyroscopic dampers in reducing wave-induced vibrations in bottom founded offshore wind turbines?"*

1.3. Opportunity for dampers

Using a damper can improve the dynamic response of the turbine under offshore environmental loads. This can, just like the lighter topside, contribute to a more structurally efficient support structure. It is expected that the lighter topside has a significant effect on the ultimate- and fatigue load toughness of the support structure. This is further elaborated in chapter 4.

Dampers in offshore wind turbines have many different forms, a handful is introduced in chapter 5. All of them have one thing in common, the additional weight and volume added to the structure. Because the DOT turbine design is reduced in weight and volume compared to the conventional electrical turbine, the implementation of a damper in the RNA could have major benefits to the overall structure.

Especially for larger turbines in deeper water, the environmental loads on the turbine increase. Wind and waves can cause significant structural vibrations, leading to higher fatigue loads in several parts of the structure. Minimizing these vibrations can lead to more reliable systems and allows for larger turbines to be placed in more remote waters. The damping of vibrations contributes to maintaining a consistent angle of incidence of the wind on the rotor. Deviations from perpendicular wind incidence induce moments on the topside, leading to vibrations throughout the tower, which are mitigated through the damping mechanism. Consequently, by ensuring a more uniform angle of incidence, the efficiency of the turbine is enhanced, resulting in an increased energy output.

In this paper, the utilization and feasibility of a gyroscopic damper will be explored. The use of this mechanism as a damper in an OWT has been briefly researched [7], but will be explored further in this thesis.

1.4. Report set-up

This report is structured to initially design a support structure for the DOT hydraulic generator pump, simultaneously with a support structure for a wind turbine with a conventional electrical generator. This is done to show the effects of the lighter topside on the support structure and its limiting factors. Later, the mechanism of a gyroscopic damper is explained. A dynamic model is set up and the effectiveness of the gyroscopic damper is tested.

In chapter 2 the basis of the design in given, on which the two foundations are based. This design cycle is shown in chapter 3. In chapter 4 the support structures are subjected to the ultimate limit state (ULS) and fatigue limit state (FLS) checks to pinpoint constraining factors. After this, the research on and mechanisms of a gyroscopic damper is explained in chapter 5. Chapter 6 shows the implementation of the gyroscopic damper in the dynamic wind turbine model, followed by the results in chapter 7. Finally, the conclusions and recommendations of the research are given in chapter 8.

2
Design Basis

The main goal for the foundation is to transfer all the loads acting on the wind turbine to the soil safely and within the acceptable deformations. This is governed by the Limit State Design philosophy, where we look at the largest possible loads acting on the system. These loads originate from the environmental climate the turbine operates in. In this case, the site location is in the Princess Amalia Wind Park, a wind park in operation since 2008, located about 23 kilometers west of Ijmuiden, North-Holland, The Netherlands. The global area of the park and the exact location of the turbine placement are depicted in figure 2.1. The characteristics of the wind turbine, the load cases and the environmental data together form the basis of the support structure design. First, the load cases are explained, then the origin of the environmental data and the adequate use of it is elaborated. Later, these loads are used throughout the paper for the limit state analysis and testing of the implemented damper.

The majority of the site data are provided by the DOT, other data is collected from open sources. As the turbine is located at the edge of the site, the influence of turbulence generated by surrounding turbines is neglected in this analysis.

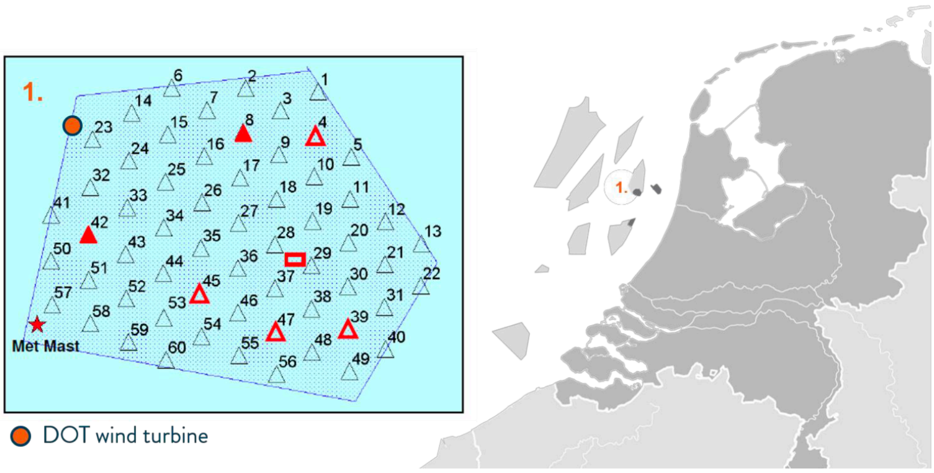

Figure 2.1: Exact location of OWT in Prinses Amalia Wind Park - source: www.noordzeeloket.nl

2.1. Load cases

The relevant standards [8], [9], [10] report numerous amounts of load cases that need to be considered to ensure the safety of the wind turbines during its lifetime. These load cases state a combination of environmental conditions. The wind conditions that are considered are as follows:

1. Normal turbulence scenario: in this condition we consider the Normal Turbulence Model (NTM) at the rated wind speed (U_R), where the highest thrust force is expected. The NTM standard deviation is stated in IEC [10].
2. Extreme turbulence scenario: in this condition we consider the Extreme Turbulence Model (ETM) at the rated wind speed (U_R). The ETM standard deviation of wind speed is again stated in IEC [10].
3. Extreme gust at rated wind speed scenario: this condition considers the 50-year EOG (extreme operating gust), described in 2.2.1, during rated wind speed (U_R) [10].
4. Extreme gust at cut-out wind speed scenario: this condition considers the 50-year EOG, described in 2.2.1, during a wind speed just below the cut-out wind speed. This EOG speed is different from the EOG at rated wind speed [10].

With the given wave heights given in table 2.1, the considered wave conditions are:

1. 1-year Extreme Sea State (ESS): this wave condition considers a wave acting on the support structure with a height equivalent to the 1-year significant wave height ($H_{m0,1}$).
2. 1-year Extreme Wave Height (EWH): this wave condition considers a wave acting on the support structure with a height equivalent to the 1-year maximum wave height ($H_{max,1}$).
3. 50-year Extreme Sea State (ESS): this wave condition considers a wave acting on the support structure with a height equivalent to the 50-year significant wave height ($H_{m0,50}$).
4. 50-year Extreme Wave Height (EWH): this wave condition considers a wave acting on the support structure with a height equivalent to the 50-year maximum wave height ($H_{max,50}$).

It is expected that the largest wind load occurs during the extreme gust at rated wind speed scenario and the highest wave load occurs during the 50-year extreme wave height scenario. It can be easily seen that the largest load on the support structure is a combination of these two. In practice, the probability of these two scenarios to happen simultaneously is negligible [8]. In this thesis, for ULS analysis, the two conservative combinations below are considered.

1. Extreme Turbulence Model (ETM) at rated wind speed, combined with the 50-year Extreme Wave Height (EWH).
2. The 50-year Extreme Operating Gust (EOG), combined with the 1-year Extreme Wave Height (EWH).

In the following section, we elaborate on these two wind conditions and two wave conditions.

2.2. Environmental data

A large part of the required environmental data can be extracted directly from the site itself. The wind and water data used in this research comes mainly from the Netherlands Enterprise Agency (NEA) [11]. NEA is an open source database providing private individuals and companies with a complete data set of wind and water statistics. This set consists of data from 1979 to 2018. The most essential parameters are summarized in table 2.1. The soil characteristics are provided by DOT and are derived from an extensive geotechnical investigation report from a third party Fugro and are elaborated in section 2.3.

Table 2.1: MetOcean data Prinses Amalia Wind Park

Parameter	**Symbol**	**1-year value**	**50-year value**	**Unit**
Mean Sea Level (MSL)	Z_{MSL}	24.4	-	m
Lowest Astronomical Tide (LAT)	Z_{LAT}	23.3	-	m
10-min average wind speed 100m	$U_{10,\text{av}}$	33.1	41.0	m/s
Average current speed	u_c	1.0	1.1	m/s
Significant wave height	H_{m0}	5.6	7.3	m
Peak wave period ass. with H_{m0}	$T_{P,Hm0}$	10.1	11.9	s
Maximum wave height	H_{max}	10.4	14.0	m
Peak wave period ass. with H_{max}	$T_{P,Hmax}$	9.2	10.2	s
Wind shear parameter	α	0.14	-	[-]
JONSWAP peak enhancement factor	γ	2.2	-	[-]

Both the wind shear parameter and the JONSWAP (JOint North-Sea WAve Project) peak enhancement factor are provided by DOT and are a result of measurements.

2.2.1. Aerodynamic data

The wind condition is a critical design input for the offshore wind turbine. It determines the total energy yield of the system, but also is the main contributor to the extreme forces acting on the support structure. Firstly, on the basis of the set turbine characteristics, power curve and wind condition, the approximate hub height is determined. The common power curve of the 2.5MW DOT hydraulic generator is shown in figure 2.2.

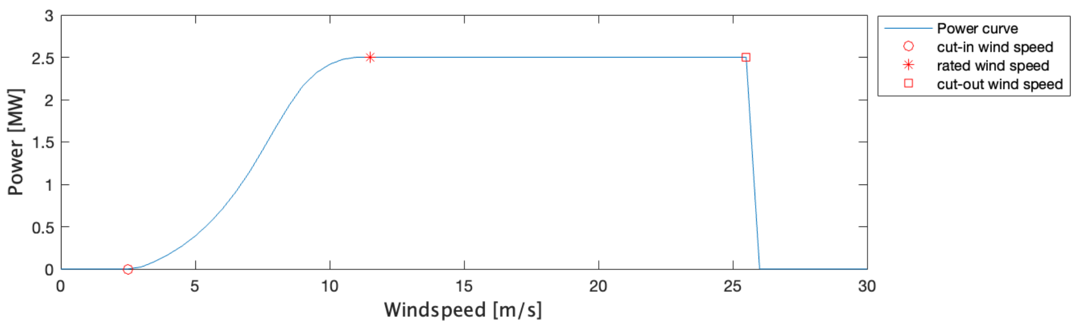

Figure 2.2: Power curve of DOT hydraulic pump generator turbine

Hub height

The height of the hub above the water level is a result of the wind distribution at the site and the power curve of the turbine. In this case, the rotor size is fixed, where this can also be varied to design the configuration with the lowest cost of energy (COE) [12]. Therefore, we exclusively base it on the annual energy yield (AEY). The AEY is the product of the power curve and the Weibull distribution of the wind at the location. The average annual energy yield, as illustrated in figure 2.3, represents the total energy output of the 2.5 MW turbine over the course of a year. From this analysis, it can be observed that the optimal hub height is approximately 70 meters. Further increases in hub height does not result in a proportional increase in energy yield sufficient to justify the additional costs associated with a taller support structure. The precise hub height will be determined in chapter 3.

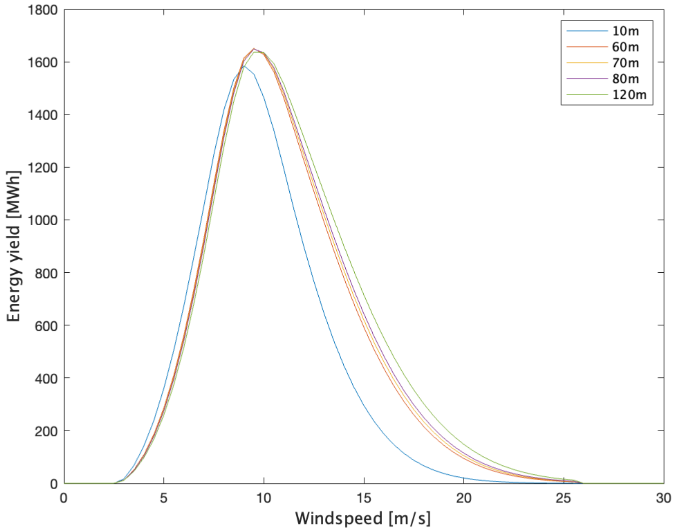

Figure 2.3: Average annual yield for several hub heights

The data set states the 10-minute average at a height of 100 meters above MSL. The mean wind speed profile, depicted in figure 2.4, can be plotted using the power law equation [13]:

$$\frac{u_z}{u_{ref}} = \left(\frac{z}{z_{ref}}\right)^{\alpha}, \tag{2.1}$$

where:

U_Z	= the wind speed at height Z [m/s]
U_{ref}	= the wind speed at reference height [m/s]
z_{ref}	= the reference height [m]
α	= the wind shear parameter [-]

This can be done for the rated wind speed, 1 year maximum and 50 year maximum, where the 1 year and 5 year maximum wind speed is the maximum wind speed statistically occurring every 1 or 50 years, respectively. For the latter meaning that, annually the change of exceeding is 1/50 or 2%. The rated wind speed profile shows the wind speed profile over the height of the support structure with a wind speed of 13 m/s at hub height. These extrapolated wind shear profiles are shown in figure 2.5.

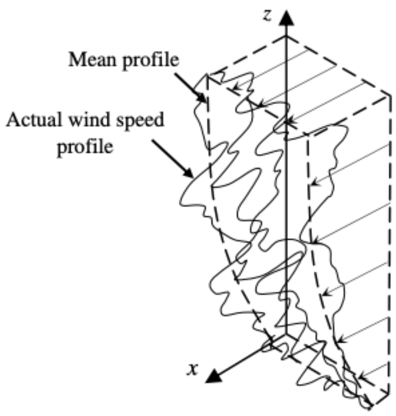

Figure 2.4: Wind speed profile representation

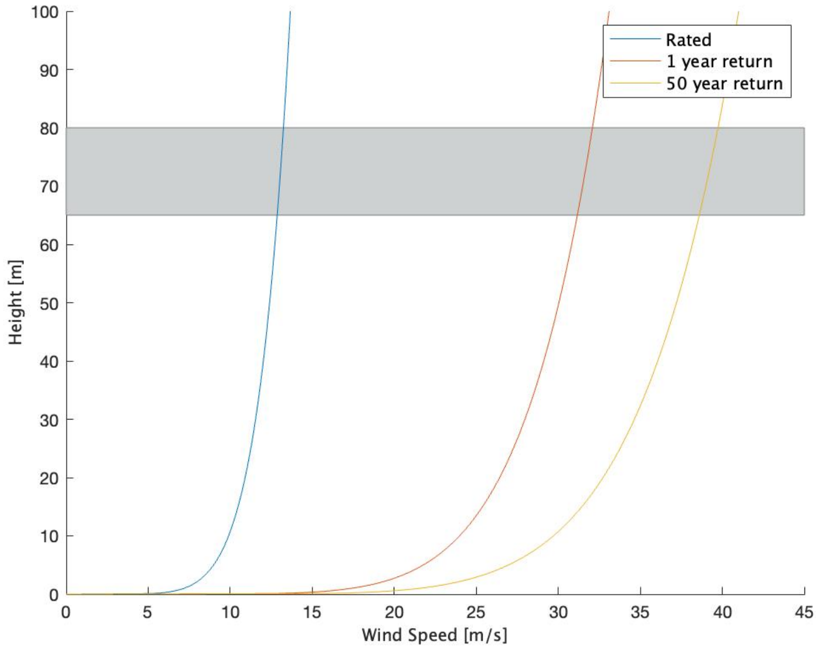

Figure 2.5: Vertical wind speed profile, with hub height region

The mean wind profile is depicted in figure 2.4, where it can be seen that this is not an evident representation of the reality. The actual wind speed profile consists of a heavy gust governed profile. Therefore, the turbulence is an important design consideration. We apply two models to represent the turbulence: the extreme operating gust at the rated wind speed:

$$u_{EOG} = \min\left\{1.35\left(U_{10,1-\text{ year}} - U_R\right); \frac{3.3\sigma_{U,c}}{1 + \frac{0.1D}{\Lambda_1}}\right\}, \tag{2.2}$$

where:

U_R	= the rated wind speed of the turbine [m/s]
$U_{10,1\text{-}year}$	= the 10 minute average wind speed with a 1 year return period at hub height [m/s]
$\sigma_{U,c}$	= the characteristic standard deviation $=0.11U_{10,1\text{-}year}$ [-]
D	= the rotor diameter [m]
Λ_1	$= L_K/8$, with L_K being the integral scale parameter [m]

and the extreme turbulence model:

$$\sigma_{U,ETM} = cI_{\text{ref}}\left[0.072\left(\frac{U_{\text{avg}}}{c} + 3\right)\left(\frac{U_R}{c} - 4\right) + 10\right] \tag{2.3}$$

where, c is a constant of 2 m/s [10], I_{ref} is the reference turbulence intensity at 15 m/s. This value is estimated to be 0.15 [10]. U_{avg} is the annual average wind speed at hub height, being 9.2 m/s.

It is expected that the maximum wind load occurs during rated wind conditions with a 50-year EOG impacting the rotor. During this event the actuation of the blade pitching is not fast enough to minimize the impact [8].

According to the DNV-OS-J101 [14] the integral scale parameter L_K is 340.2 meters. The calculated EOG can be added on top of the wind speed profile of figure 2.5 to obtain the maximum wind speed. This is used in chapter 3 to calculate the largest overturning moment.

2.2.2. Hydrodynamic data

The severity of the hydrodynamic environment can be captured in several parameters, which are used to calculate the maximum loads on the submerged support structure caused by the waves. A summary of the most significant provided values of the sea state are given in table 2.1. Here, it is relevant to note that the significant and extreme wave height have different meanings. Where the extreme wave height is the single highest wave in a 3-hour sea state, the significant wave height is the average of the highest one third of all waves in the same sea state. The water current velocity is significantly lower and are therefore not considered in this case.

These hydrodynamic loads together with the load cases in 2.1 give the maximum loads originating from the sea environment.

2.3. Soil characteristics

The soil characteristics play a significant role in the dynamic behaviour of an OWT. Especially for turbines placed in shallow water as the DOT tower, soil stiffness plays a consequential role in its dynamic nature [15]. An extensive investigation regarding the soil is therefore very important. DOT features soil data, obtained by a third party through a cone penetration test (CPT). For confidential reasons the exact data can not be shared in this thesis. Together with this and the fact that soil behaviour is not the focus of this research, the effects of the soil are modelled as a set of equivalent springs located at the mudline. Figure 2.6 shows the equivalent springs: K_R (rotational stiffness), K_L (lateral stiffness), K_{LR} (cross coupling) and K_V (vertical stiffness). For this example of a small turbine, it is not expected that the pile bearing capacity is governing. Therefore, the vertical stiffness is in this case not considered, as we assume the system is very stiff in the vertical direction.

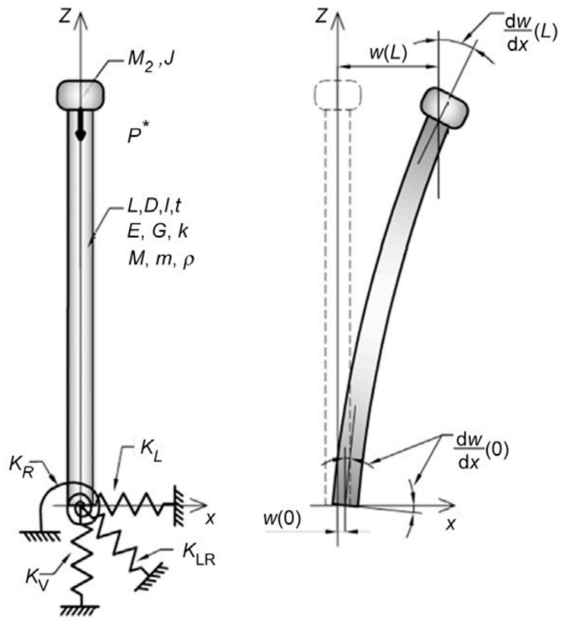

Figure 2.6: Schematic resemblance OWT with equivalent springs

The vast majority of the soil consists of clean to silty sand for the first 20 meters below the mudline. This soil has an average unit weight of 17 kN/m^3, which linearly increases over the depth.

The values of the equivalent springs are determined according to Davis and Poulos [16], where the equations for the spring coefficients for rigid piles in linearly in-homogeneous soil are given in the following set of equations:

$$
\begin{aligned}
K_L &= \frac{1}{2} L_P^2 n_h \\
K_{LR} &= -\frac{1}{3} L_P^3 n_h \\
K_R &= \frac{1}{4} L_P^4 n_h
\end{aligned}
\tag{2.4}
$$

Here L_P is the, to be determined, embedded pile length of the monopile and n_h is the coefficient of subgrade reaction [17], which can be evaluated via

$$
n_h = \frac{A\gamma'}{1.35} \tag{2.5}
$$

Here, A is in the range of 300-1000 for medium sand and 100-300 for loose sand, here we use 600 as the sand is of medium density. γ' is the average soil weight, which is already stated above. Finally, it is necessary to verify whether the assumption of rigid piles is acceptable. This can be done by checking the boundaries from the two equations [18]:

$$
\begin{aligned}
\text{Slender if:} \quad & L_p > \frac{4EI_p}{n_h} \\
\text{Rigid if:} \quad & L_p < \frac{2EI_p}{n_h}
\end{aligned}
\tag{2.6}
$$

Here the E is the Young's modulus of the steel and I_P is the second moment of area of the pile. Making use of equations 2.4 to 2.6, the spring coefficients can be determined as a function of the embedded length. The required embedded length and its resulting values for the equivalent springs are assessed in section 3.3.

Due to the loading cycles, the stiffness of the soil changes over time. This is not captured in the modelling of the soil-structure interaction as linear springs. To check for ULS in the future, some safety factor should be applied [19], but for this initial design this is omitted for now. The calculated parameters are summarized in table 2.2.

Table 2.2: Soil parameters

Parameter	Symbol	value	Unit
Average soil weight	γ'	17	kN/m^3
Soil parameter	A	600	-
Internal angle of friction	ψ'	43	°

3

Support Structure Design

The aim of this research is to show the effects of a lighter topside on the support structure. Based on the design basis, an initial support structure design will be set up [18]. The values given as example throughout this chapter are for the DOT hydraulic generator. At the end of this chapter the effects of using a conventional heavier generator on the support structure will be assessed. For comparability reasons, the tower dimensions of the two support structures will be kept the same, only the slipjoint and monopile dimensions will be altered for the different topsides.

In the next chapter, the initial support structure designs will be tested on their ultimate limit state (ULS) capacities and a fatigue limit state (FLS) analysis will be done over the life span. With both checks the support structure dimensions will be altered accordingly.

Slip joint
Besides the development of the hydraulic low speed pump, DOT has realised other new innovative components for wind turbines. One of these components is the slip joint, depicted in figure 3.1. The slipjoint is included in this research as it is an integral part of the DOT design and therefore makes the support structure design more realistic.

This simplified method of connecting the foundation monopile to the turbine tower makes use of the friction between the two conical shapes. In comparison with the two conventional methods, grouted and bolted, the slip joint does not use any additional materials as bolts or grouting. But its greatest advantage is, that this method reduces the installation time offshore [4].

This connection method will be used in the design of the support structures. As the mechanics of the slip joint are not in the scope of this research, the conical slip joint will be represented as a part between the turbine and foundation with twice the wall thickness of the tower and an expanding angle between 0.5° and 1.5°.

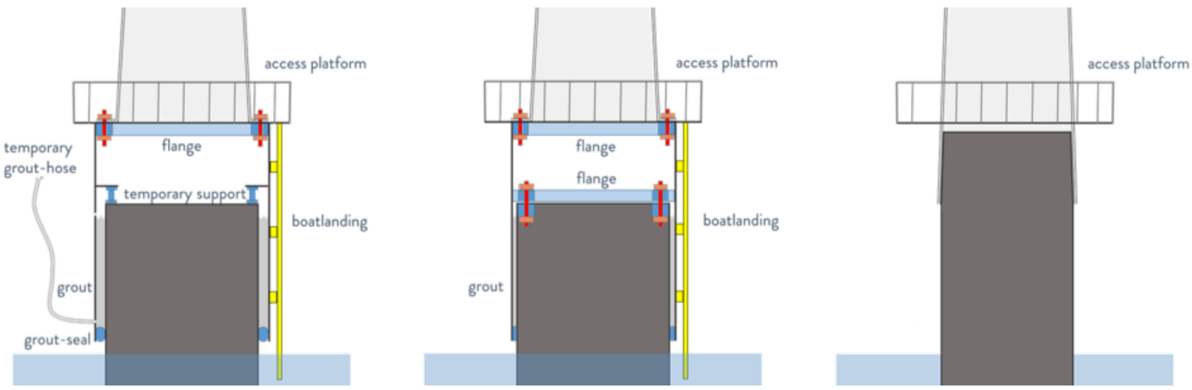

Figure 3.1: Grouted (left), bolted (middle) and slip joint connection [4]

The following steps will be conducted to construct a suitable support structure for the novel turbine design:

1. *Target frequency* - the target natural frequency is set, depending on the environmental loading and rotor characteristics.
2. *Initial pile diameter* - guess the initial pile diameter based on the maximum overturning moment as the mudline due to the wind load and the structural yield criteria of the material. With this diameter the hydrodynamic loads on the monopile can be computed.
3. *Embedded pile length* - Based on the geotechnical data and maximum allowable deformations at the mudline, the embedded length of the monopile can be determined.
4. *Calculation of natural frequency* - the natural frequency of the initial support structure is determined via the stepped tower method.
5. *Support structure optimization* - Iterative optimization of the initial support structure configuration, based on the ultimate limit state (ULS) and fatigue limit state (FLS) and calculated natural frequency.

3.1. Target frequency

The target natural frequency (f_n) of the system is an important design parameter. When the system is dynamically loaded with a frequency close to the natural frequency of the system, the dynamic response is amplified, possibly resulting in structural and material damages. Therefore, it is very common to design the support structure in such a way that the natural frequency does not coincide with the frequencies of the external loads acting on the system. In this study: wind, wave and rotor loads are considered.

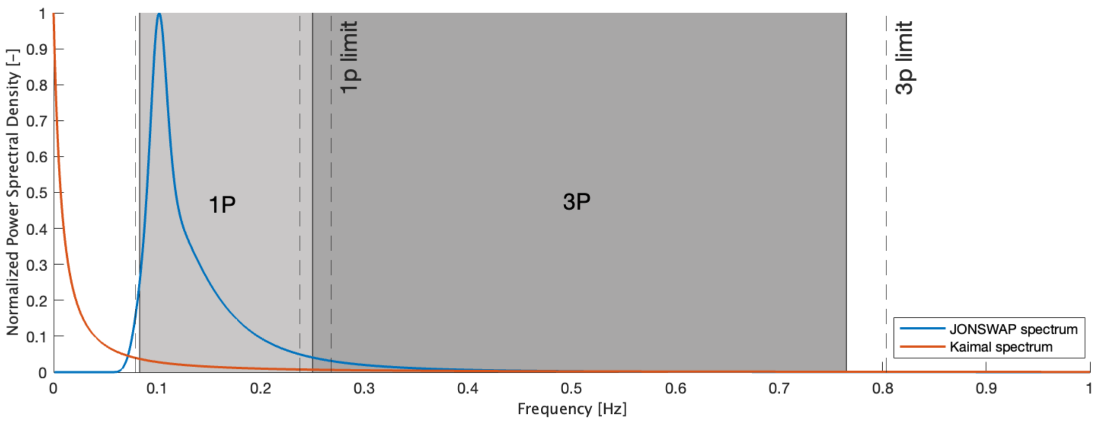

Figure 3.2: Frequency diagram

Figure 3.2 shows the frequencies of the considered forces acting on the turbine. The wind forcing is captured in the Kaimal spectrum and the waves are represented by the JONSWAP spectrum, both according to the DNV standards [14]. It is practice to set the target structural natural frequency above the the frequency domain of the waves. Normally, the target frequency is set between the ranges of the 1P and 3P, the rotor rotational and blade passing frequency respectively. As in this case these ranges overlap, the target natural frequency is set in the lower region of the 3P blade passing frequency range. To still bypass the resonance, the method of frequency skipping it used [20]. During frequency skipping, the torque in the hydraulic pump is externally altered when the rotor frequency approaches the natural excitation frequency. This way the 3P blade passing frequency that coincides with the natural frequency is omitted. In the lower region of the 3P blade passing frequency the rotational speed of the rotor is lowest, hence the energy is lowest in the rotor. Applying frequency skipping in this frequency range is therefore easiest and has the lowest risk. Concluding, the target natural frequency of the system is set to 0.27 hertz.

3.2. Initial pile diameters

To set the initial diameters of the monopile, the maximum overturning moment at the mudline due to the aerodynamic load is calculated. Once the diameter of the submerged monopile is known, the hydrodynamic forces can be generated. The dominating load cases for this initial analysis are the ETM and 50-year EWH, and EOG and 1-year EWH combinations. The results of this iterative process are shown in table 3.1.

3.2.1. Aerodynamic loading

To establish the initial diameter of the monopile, the maximum thrust force is calculated. This force can be calculated, in a simplified manner, with equation

$$F_{\text{wind },EOG} = T_{EOG} = \frac{1}{2}\rho_a A_R C_T \left(U_R + u_{EOG}\right)^2, \tag{3.1}$$

where, U_R is the maximum wind speed hitting the rotor swept area A_R and C_T is the thrust coefficient, which can be conservatively estimated as $7/U_R$ [21].
The overturning moment at the mudline, while applying the correct load factor of γ_L = 1.35 according to the standards [8], can then evidently be calculated by

$$M_{wind,EOG} = T_{EOG}(S + z_{hub})\gamma_L. \tag{3.2}$$

The loads and moments are given in table 3.1.
From this, the initial dimensions of the pile can easily be found using the following equation:

$$\sigma_m = \frac{M_{wind,EOG} * D_P}{2I_P} < \frac{f_{yk}}{\gamma_M} \tag{3.3}$$

where, I_P is the moment of inertia of the pile, f_{yk} is the yield stress in the S355 steel and γ_M is the factor of material = 1.1. Through equations 3.1 to 3.3 we find the initial pile dimensions and are then: D_P **= 4.25 [m] and** t_P **= 0.04 [m]**.

3.2.2. Hydrodynamic loading

Using the initial dimensions of the monopile, the critical hydrodynamic loads can be calculated. For this simplified wave load approximation, the Morison equation is used [22]. This equation is based on the linear Airy wave theory for which the surface elevation η, horizontal particle velocity w and horizontal particle acceleration $\dot{w}$ are given in the characteristic equations 3.4, 3.5 and 3.6, respectively.

$$\eta(x,t) = \frac{H_m}{2}\cos\left(\frac{2\pi t}{T_S} - kx\right) \tag{3.4}$$

$$w(x,z,t) = \frac{\pi H_m \cosh(k(S+z))}{T_S \sinh(kS)}\cos\left(\frac{2\pi t}{T_S} - kx\right) \tag{3.5}$$

$$\dot{w}(x,z,t) = \frac{-2\pi^2 H_m \cosh(k(S+z))}{T_S^2 \sinh(kS)}\sin\left(\frac{2\pi t}{T_S} - kx\right) \tag{3.6}$$

where, x is the horizontal coordinate along the direction of wave propagation. Here, x = 0 is the location of the monopile. k is the wave number, which can be obtained from the dispersion relation:

$$\omega^2 = gk\,tanh(kS) \;\text{ with }\; \omega = \frac{2\pi}{T_S}. \tag{3.7}$$

The complete derivation for obtaining the foundation loads can be found in Appendix A. The final wave loads are summarized in table 3.1. In this simplified approach to determining foundation loads, it is conservative to consider the design wave load as the sum of the drag and inertia loads, as these loads do not occur simultaneously in reality.

The application point of the extreme wave is at 1/3 below the highest point of the wave. The wave-induced moment can then be simply computed. The same stress check, given in equation 3.3, can then be performed for the hydrodynamic loading.

Table 3.1: ULS load combinations

Load	Extreme Wind Scenario ETM and 50-year EWH	Extreme Wind Scenario EOG at U_R and 1-year EWH
Maximum wind load [MN]	0.98	1.30
Maximum wind moment [MNm]	139.57	184.87
Maximum wave load [MN]	3.49	2.64
Maximum wave moment [MNm]	81.95	58.83
Total load [MN]	4.47	3.94
Total overturning moment [MNm]	221.52	243.69

These total loads lead to new pile dimensions, therefore changing the hydrodynamic loads again. This iterative process is solved to find the required pile dimensions. **Where: D_P = 4.75 [m] and t_P = 0.044 [m]**.

3.3. Embedded pile length

Typically, the limiting factor for maximum lateral loads is the material yield strength of the pile. A check has to be performed to ensure that the foundation is able to carry the load. This is done by calculating the lateral deflection and rotation at the mudline [18].

The deflection ρ_m and rotation θ_m can be easily calculated using the equivalent springs at the mudline, depicted in figure 2.6. The stiffness model can be written as a stiffness matrix:

$$\begin{bmatrix} F_x \\ M_y \end{bmatrix} = \begin{bmatrix} K_L & K_{LR} \\ K_{LR} & K_R \end{bmatrix} \begin{bmatrix} \rho_m \\ \theta_m \end{bmatrix} \tag{3.8}$$

Where F_x is the maximum lateral force in the for-aft direction and M_y is the maximum overturning moment around the y-axis, both summarized in table 3.1. K_L,K_{LR} and K_R are evaluated in section 2.3 and are dependant on the embedded length of the monopile. The deformations can be determined in an iterative manner, with a limitation for rigid behaving monopiles in sandy soils of 0.5° [23]. The determined springs coefficients, required embedded length and accompanying deformations at the mudline are given in table 3.2.

Because both mudline deformations are well within their respective limits, the negligence of the axial forcing component is valid.

Table 3.2: Soil and spring parameters

Parameter	Symbol	value	Unit
Longitudinal spring coefficient	K_L	1.22	GN/m
Coupling spring coefficient	K_{LR}	-1.47	GN
Rotational spring coefficient	K_R	19.80	GNm/rad
Embedded length	L_{emb}	18	m
Lateral displacement at mudline	ρ_m	0.014	m
Rotation at mudline	θ_m	0.171	°

3.4. Calculation of natural frequency

As explained in Section 3.1, the first eigenfrequency, also called the natural frequency, of a system is an important parameter for the dynamic stability of any loaded structure. To determine the natural frequency of the OWT, the fixed base natural frequency is calculated and corrected by several design coefficients [18].

$$f_n = f_{fb} C_L C_S C_R \tag{3.9}$$

where,f_n is the fixed base natural frequency, C_L and C_R are the lateral and rotational foundation flexibility coefficients and C_S is the flexibility coefficient of the support structure. Here, the stepped tower method is used to express this first natural frequency of a fixed base system (f_{FB}) [24]. The analytical expression for the natural period is given as

$$T_n^2 = \frac{4\pi^2 (M_{top} + m_{eq} L) L^3}{3EI_{eq}} \frac{48}{\pi^4}, \tag{3.10}$$

from which the natural frequency can be easily derived with $f_{FB} = 1/T_n$.
Here:

m_{top}	= the mass of the topside [kg]
m_{eq}	= the equivalent mass per unit length [kg/m]
I_{eq}	= the equivalent second moment of area [m^3]
E	= the elastisticy modulus steel (210 GPa)
L	= the total length of the system [m]

The system is split up into equal 10 cm length segments. The second moment of area and mass per segment is calculated and used to calculate their equivalent adaptions of the entire system with the following two equations:

$$I_{eq} = \frac{\sum_{j=1}^{n} I_j l_j \cos^2\left(\frac{\pi x_j}{2L}\right)}{L}, \tag{3.11}$$

$$m_{eq} = \frac{\sum_{j=1}^{n} m_j l_j \left(1 - \cos\left(\frac{\pi x_j}{2L}\right)\right)^2}{L}, \tag{3.12}$$

where:

I$_j$	= the segment second moment of area of [m^4]
l$_j$	= the segment length [m]
x$_j$	= the distance from the segment to the mudline [m]
m$_j$	= the segment mass [kg]

The fixed base frequency has been cross checked by comparing the result with the analytical result of a continue cantilever beam, where the results for a 20m cantilever beam, with segment length 0.1m, are 3. 8% higher than the analytically computed value. This is deemed functional for this engineering purpose.

The rotational and lateral flexibility coefficients account for the foundation stiffness. Their expressions can be found in the following equations:

$$C_R = 1 - \frac{1}{1 + 0.6(\eta_R - \frac{\eta_{LR}^2}{\eta_L})}, \tag{3.13}$$

$$C_L = 1 - \frac{1}{1 + 0.5(\eta_L - \frac{\eta_{LR}^2}{\eta_R})}. \tag{3.14}$$

These coefficients are defined by the dimensionless foundation stiffness values η_L, η_{LR} and η_R. It can be easily seen that the natural frequency again is a function of the equivalent springs and, therefore, the embedded length. L_T is the length of the tower.

$$\eta_L = \frac{K_R L_T}{EI_{eq}} \quad (3.15) \qquad \eta_{LR} = \frac{K_{LR} L_T}{EI_{eq}} \quad (3.16) \qquad \eta_R = \frac{K_R L_T}{EI_{eq}} \quad (3.17)$$

The support structure flexibility coefficient is calculated using the non-embedded monopile length from the slipjoint to the mudline (L_S). It is calculated using two dimensionless coefficients that express the stiffness ratio between the tower and monopile, $\chi = EI_T/EI_P$. Where, EI_T is the bending stiffness of the tower and EI_P is the bending stiffness of the non-embedded monopile. And finally, the length ratio, $\phi = L_S/L$, where L is the total length of the system. The support structure flexibility coefficient can then be derived using equation

$$C_S = \sqrt{\frac{1}{1 + (1+\phi)^3\chi - \chi}}. \quad (3.18)$$

By calculating the natural frequencies of offshore wind turbines where this is empirically measured, the proposed method can be validated. The input parameters are summarized in table 3.3 [25], [26].

Table 3.3: Input parameters OWTs for validation

Parameters	**Symbol**	**Irene Vorrink**	**Kentish Flats**	**Lely A2**	**North Hoyle**	**Walney 1**	**Unit**
Top mass	m_{top}	35.7	130.8	32	100	234.5	ton
Density steel	ρ_{steel}	7860	7860	7860	7860	7860	kg/m^3
Tower length	L_T	44.5	60.06	37.9	67	67.3	m
Diameter tower top	$D_{T,t}$	1.7	2.3	1.9	2.3	3	m
Diameter tower bottom	$D_{T,b}$	3.5	4.45	3.2	4	5	m
Tower wall thickness	t_T	13	22	13	35	40	mm
support structure length	L_{ss}	5.2	16	12.1	7	37.3	m
support structure diameter	D_{ss}	3.5	4.3	3.2	4	6	m
support structure wall thickness	t_{ss}	28	45	35	50	80	mm
Embedded length	L_{emb}	19	29.5	13.5	33	23.5	m
Young's Modulus	E	210	210	210	210	210	GPa
Submerged unit weight soil	γ'	9.76	10	9.76	9.76	10	kN/m^3
Soil density indicator	A_{soil}	600	1500	600	600	1500	-

The calculated frequencies are presented in table 3.4. Equations 2.4 and 2.5 are altered for slender monopile designs as outlined in equation 2.6. Here, the slenderness or rigidity of the embedded monopile is a function of its dimensions and the characteristics of the soil. It can be seen that the support structure of OWT Irene Vorrink can not be classified as slender or rigid, as falls outside the ranges.

The inability to classify the OWT Irene Vorrink's support structure means that the suggested model does not adequately assess its natural frequency. Furthermore, the computed frequencies are slightly overestimated. However, despite these limitations, when complying with equation 2.6 for slender or rigid configurations, the model is deemed applicable for engineering purposes.

Table 3.4: Measured and calculated frequencies

OWT ID	Slender / Rigid	Measured f_0 [Hz]	Calculated f_0 [Hz]	Error [%]
Lely A2	Rigid	0.634	0.640	0.9
Irene Vorrink	-	0.546	0.670	18.5
Kentish Flats	Slender	0.339	0.351	3.4
Walney 1	Rigid	0.350	0.353	0.8
North Hoyle	Slender	0.350	0.358	2.2

The natural frequency of the system can conclusively be calculated filling in equation 3.9 using the formerly determined initial parameters of the monopile. The governing tower parameters are optimized for the minimal material used to still satisfy the target frequency. An angle of 0.5-1.5° of the slipjoint with the vertical axis needs to be guaranteed with a wall thickness of twice the thickness of the tower. The described manner of calculating the parameters can be solved iterative, to be within the given dynamical and structural boundaries. The found parameters of the DOT and conventional support structure are presented in table 3.5.

To correctly visualise the effects of a lighter topside on the monopile dimensions, the tower dimensions shall be kept equal for both cases. Because of that the method of altering the support structure dimensions is as follows:

1. Increase monopile diameter by increasing the slipjoint angle.
2. Increase monopile wall thickness.

Table 3.5: Parameters support structure

Parameter	Symbol	DOT	Conventional	Unit
Tower length	L_T	65	65	m
Slipjoint length	L_{SJ}	9	9	m
Monopile length	L_{MP}	31	31	m
Embedded length	L_{emb}	18	18	m
Diameter tower top	$D_{T,t}$	3	3	m
Diameter tower bottom	$D_{T,b}$	5.2	5.2	m
Diameter slipjoint top	$D_{SJ,t}$	5.2	5.2	m
Diameter slipjoint bottom	$D_{SJ,b}$	5.29	5.44	m
Diameter monopile	D_{MP}	5.29	5.44	m
Wall thickness tower	t_t	30	30	mm
Wall thickness slipjoint	t_{SJ}	60	60	mm
Wall thickness monopile	t_{MP}	50	58	mm
Slipjoint angle	α_{SJ}	0.6	1.5	°

Altering the weight of the topside has a significant effect on the natural frequency of the turbine, which can be easily concluded by looking at equation 3.10. Substituting the 50% heavier topsidfe lowers the natural frequency. An additional volume of steel of 13% is required to meet the natural frequency, thus showing the advantage of a lighter topside.

These two designs will both be further analysed in the following chapter on their ultimate and fatigue limit states to show the technical challenges to come with this novel turbine design.

4
Limit State Analysis

In the coming sections, on the basis of the ultimate limit state (ULS) and fatigue limit state (FLS), the support structure will be tested and optimized in more detail. A distinction between the conventional and lighter topside weight will be made in the coming sections. This will manifest the effects of the lighter topside on the support structure and reveal the possible new limiting factors.

4.1. Ultimate Limit State

The ULS design check for monopile-based support structures primarily relates to the check of tubular structures. For this the Von Mises yield check and global buckling check are required [27]. DNV standard also state for a local buckling check. This is omitted in this thesis, as it requires a more detailed design [28]. Because we are looking for the impact of a more slender support structure on the overall ULS performance, the states of the bolted and welded connections are also not considered in this research. The following analysis will be performed for both the DOT and conventional design.

4.1.1. Yield check

The first performed check is the Von Misis stress check [29]. Here the maximum occurring stresses in the support structure are compared to the yield strength of the material used, in this case S355 steel. The Von Mises stress can be expressed as a function of the maximum stresses caused by axial forces, shear forces and overturning moments:

$$\sigma_{VM} = \sqrt{\sigma_X^2 + \sigma_Y^2 - \sigma_X \sigma_Y + 3\tau_{XY}^2} \tag{4.1}$$

For the present study, it is sufficient to only consider the axial and shear stress caused in one direction. Meaning, we only consider the shear force and bending in the for-aft direction, when the maximum stress occurs. The simplified equation therefore becomes

$$\sigma_{VM} = \sqrt{\sigma_X^2 + 3\tau_{XY}^2} \tag{4.2}$$

Here σ_X is the axial stress consists of a normal force component and an overturning moment component, given by

$$\sigma_X = \frac{N}{A}\gamma_g + \frac{M}{W}\gamma_e \tag{4.3}$$

The normal force (N) is caused by the own weight of the system. The moment (M) is a result of the environmental loading, as described in section 2.1.

where: N = Normal force [N]
A = Segment cross section [m^2]
M = Moment [Nm]
W = Segment elastic section modulus [m^3]
γ_g = Permanent load safety factor = 1.1
γ_e = Environmental load safety factor = 1.35

The shear stress in equation 4.1, τ_{xy}, can be calculated with:

$$\tau_{xy} = \frac{2V}{A}\gamma_e, \tag{4.4}$$

where V is the shear force at a certain height.

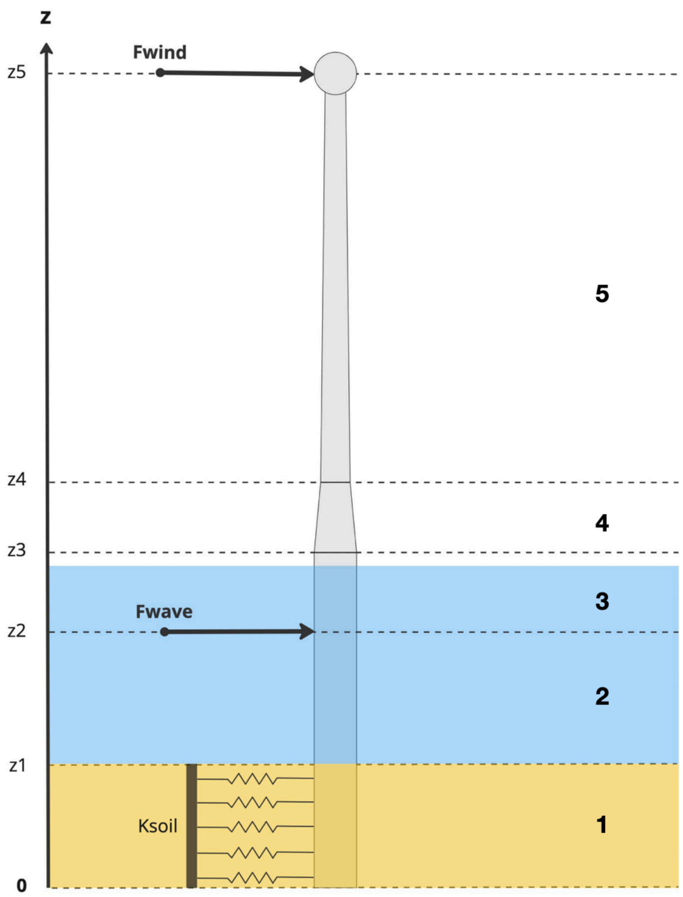

Figure 4.1: Schematic ULS analysis model

The Von Mises stress is a function of the shear force, moment and normal force along the height of the system, caused by the ultimate limit state environmental condition. To determine the shear force and moment, a static model is set up. This system is shown in figure 4.1. Due to the static nature of the ultimate limit state response, the time dependant physics, such as damping, can be neglected. The wave force is simplified and is modelled as a concentrated force the equivalent point of application, which is 1/3 of the water depth below the waterline [8]. The wind forcing hitting the tower and the current forcing acting on the submerged support structure are not included in this analysis, as they are negligible [28]. As the diameter of the monopile is updated in an iterative way, the wave forcing is also updated accordingly.

Once the model is set up, the maximum displacement of the OWT to the ULS load case, as described in section 2.1, can be calculated. Through the correlations 4.5 and 4.6, between displacement and bending stiffness, the maximum shear and moment can be determined.

$$M = -EI\frac{\partial^2 u}{\partial z^2} \quad (4.5) \qquad\qquad Q = \frac{\partial M}{\partial z} \quad (4.6)$$

The model consists of 5 beam element, chosen in such a way that the forces act upon the boundaries of the beam. Also the surrounding medium, and support structure parts change at the boundaries of the beams. For beam 4 and 5, the slipjoint and the tower respectively, the average parameters such a diameter and moment of inertia, are used for the model. For the notation above, using the Euler-Bernouilli beam theory, the equations of motion for each segment can be written as:

$$\begin{aligned}
EI_5\frac{\partial^4 u_5}{\partial z^4} + \rho A_5 Lg\frac{\partial^2 u_5}{\partial z^2} &= 0 \quad z_4 \leq z \leq L \\
EI_4\frac{\partial^4 u_4}{\partial z^4} + \rho A_4 Lg\frac{\partial^2 u_4}{\partial z^2} &= 0 \quad z_3 \leq z \leq z_4 \\
EI_3\frac{\partial^4 u_3}{\partial z^4} + \rho A_3 Lg\frac{\partial^2 u_3}{\partial z^2} &= 0 \quad z_2 \leq z \leq z_3 \\
EI_2\frac{\partial^4 u_2}{\partial z^4} + \rho A_2 Lg\frac{\partial^2 u_2}{\partial z^2} &= 0 \quad z_1 \leq z \leq z_2 \\
EI_1\frac{\partial^4 u_1}{\partial z^4} + \rho A_1 Lg\frac{\partial^2 u_1}{\partial z^2} + k_{\text{soil}}\, u_1 &= 0 \quad 0 \leq z \leq z_1
\end{aligned} \tag{4.7}$$

The set of fourth order differential equations 4.7 can be solved by assuming the correct general solution for each corresponding segment and implementing these in the boundary and interface conditions of the system. The boundary conditions at the ends of the system, z=0 and z=L, are given as:

$$\left.\frac{\partial^2 u_{1,5}}{\partial z^2}\right|_{z=0,L} = \left.\frac{\partial^3 u_1}{\partial z^3}\right|_{z=0} = 0 \tag{4.8}$$

$$-EI_5 \left.\frac{\partial^3 u_5}{\partial z^3}\right|_{z=L} = F_{wind} \tag{4.9}$$

The interface conditions between the sequential beams 1 to 5 state that the displacements, rotations, shear forces and moments are equal between all the connecting beam segments. The interface conditions at the locations: z1, z3 and z4 are given as:

$$u_n(z_n) = u_{n+1}(z_n) \tag{4.10}$$

$$\left.\frac{\partial u_n}{\partial z}\right|_{z=z_n} = \left.\frac{\partial u_{n+1}}{\partial z}\right|_{z=z_n} \tag{4.11}$$

$$\left.\frac{\partial^2 u_{1,3,4}}{\partial z^3}\right|_{z=z_{1,3,4}} = \left.\frac{\partial^2 u_{2,4,5}}{\partial z^3}\right|_{z=z_{1,3,4}} \tag{4.12}$$

$$\left.\frac{\partial^3 u_n}{\partial z^2}\right|_{z=z_n} = \left.\frac{\partial^3 u_{n+1}}{\partial z^2}\right|_{z=z_n} \tag{4.13}$$

At the height z=z2, where the wave force affects, the wave force appears in the equilibrium:

$$- EI_2 \left. \frac{\partial^3 u_2}{\partial z^3} \right|_{z=z2} + F_{wind} = -EI_3 \left. \frac{\partial^3 u_3}{\partial z^3} \right|_{z=z2} \tag{4.14}$$

Since segments 2, 3, 4, and 5 are not subjected to any external loading, the general solution to the governing differential equations is given by the corresponding homogeneous equations:

$$u_n(z) = A_n + B_n z + C_n \sin\left(\sqrt{\frac{m_n g}{EI_n}} z\right) + D_n \cos\left(\sqrt{\frac{m_n g}{EI_n}} z\right), \tag{4.15}$$

where, m_n is the mass of segment n. The equations of motion of the segment that is submerged in the soil can be rewritten as the fourth order differential equation:

$$\frac{\partial^4 u_1}{\partial z^4} + \alpha^2 \frac{\partial^2 u_1}{\partial z^2} + \beta u_1(z), \tag{4.16}$$

where, $\alpha = \frac{m_1 g}{EI_1}$ and $\beta = \frac{k_{soil}}{EI_1}$. For equation 4.16, the general solution can be formulated as:

$$u(z) = \sum_{n=1}^{4} C_n e^{i\lambda_n z} \tag{4.17}$$

for which the fourth-order characteristic equation is defined as:

$$\lambda^4 + \alpha^2 \lambda^2 + \beta = 0. \tag{4.18}$$

For this equation, the four eigenvalues λ can be found, and the solution for segment 5 can be written as:

$$u_1(z) = A_1 e^{(\lambda_1 z)} + B_1 e^{(-\lambda_1 z)} + C_1 e^{(\lambda_2 z)} + D_1 e^{(-\lambda_2 z)}. \tag{4.19}$$

The general solutions to the differential equations can be applied to the system's boundary conditions, allowing us to solve the unknown constants. This completes the set of equations describing the displacement of the entire system under the ultimate limit state environmental forces. The displacement of the DOT turbine is illustrated in figure 4.2.

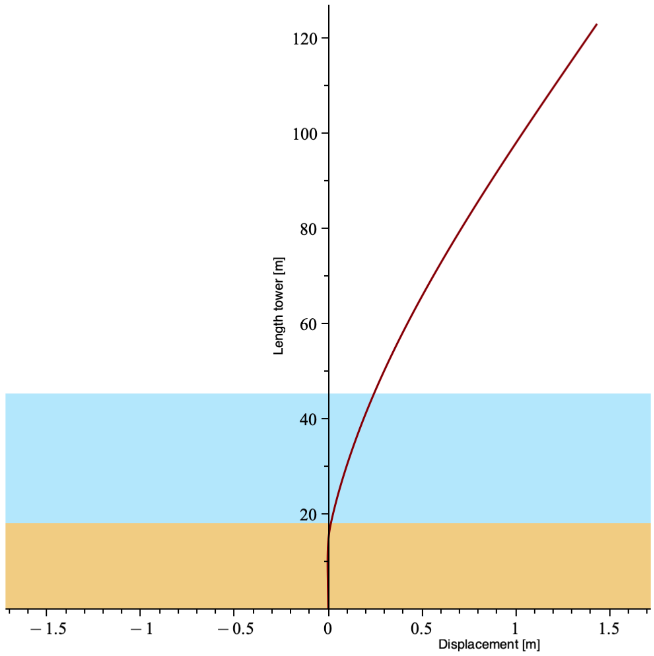

Figure 4.2: Displacement DOT turbine over full length - ULS case

With the relation of displacement and tower stiffness in equations 4.5 and 4.6, the moment and shear force along the length of the tower can also be calculated and is depicted in figures 4.3a and 4.3b.

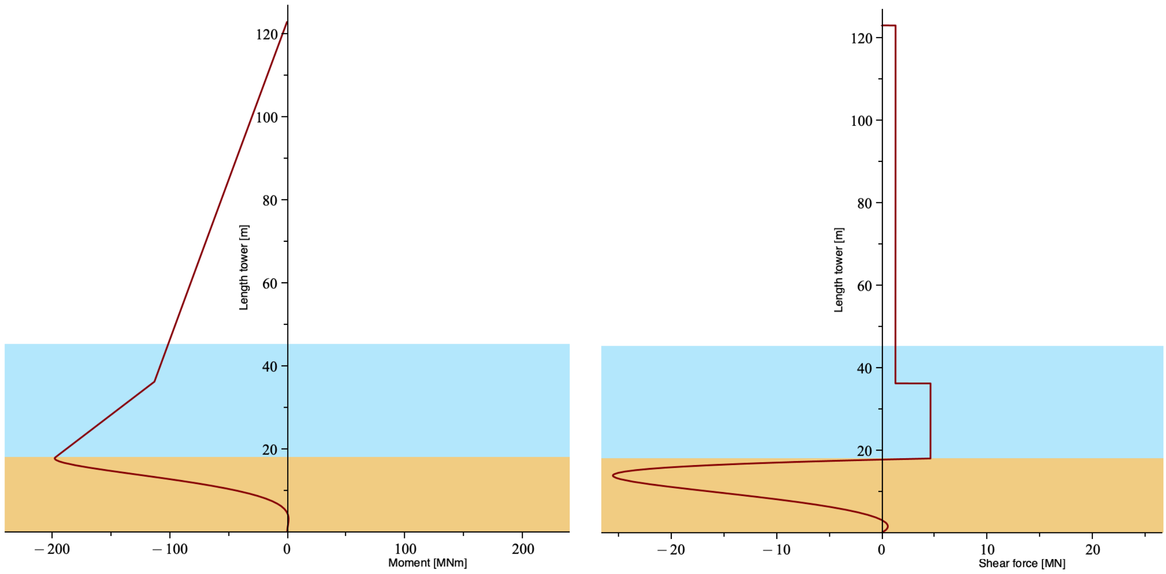

(a) Moment

(b) Shear force

Figure 4.3: Moment and shear force DOT turbine - ULS case

As expected, the maximum moment and shear force occur below the mudline, approximately 1 times the diameter of the monopile [18]. With the moment, shear force and normal force known along the length of the structure, the Von Mises stress can then be computed using equation 4.2. For each 10cm segment that the model consists of, the Von Mises check,

$$\frac{\sigma_{VM}}{f_y \gamma_m} \leq 1, \tag{4.20}$$

can be performed. Here, f_y is the yield strength of the S355 steel. For plate material between 25mm and 50mm thickness, the yield strength is reduced to 335MPa [30]. The material factor γ_m is 1.1 [-].

4.1.2. Global buckling check

Secondly, the global buckling check is performed following Eurocode [27]. The equations for the global buckling check of members subjected to combined bending and axial compression are given as the two equations:

$$\frac{N_{Ed}}{\frac{\chi_y N_{Rk}}{\gamma_{M1}}} + k_{zy} \frac{M_{y,Ed} + \Delta M_{y,\mathrm{Ed}}}{\chi_{LT} \frac{M_{y,Rk}}{\gamma_{M1}}} + k_{yz} \frac{M_{z,\mathrm{Ed}} + \Delta M_{z,\mathrm{Ed}}}{\frac{M_{z,Rk}}{\gamma_{M1}}} \leq 1, \tag{4.21}$$

$$\frac{N_{Ed}}{\frac{\chi_z N_{Rk}}{\gamma_{M1}}} + k_{yy} \frac{M_{y,Ed} + \Delta M_{y,\mathrm{Ed}}}{\chi_{LT} \frac{M_{y,Rk}}{\gamma_{M1}}} + k_{zz} \frac{M_{z,\mathrm{Ed}} + \Delta M_{z,\mathrm{Ed}}}{\frac{M_{z,Rk}}{\gamma_{M1}}} \leq 1. \tag{4.22}$$

Since only bending moments in one direction are considered, and torsional moments are neglected, the equations can be simplified to the single unity check given by:

$$\frac{N}{\frac{\chi_z N_{Rk}}{\gamma_{M1}}} + k_{yy} \frac{M_y + \Delta M_{y,\mathrm{Ed}}}{\chi_{LT} \frac{M_{y,Rk}}{\gamma_{M1}}} \leq 1 \tag{4.23}$$

where: N = Normal force [N]
M_y = Moment [Nm]
ΔM_y = Moment due to the shift of the centroidal axis [Nm]
χ_z = reduction factor due to flexural buckling
$\gamma_m 1$ = partial safety factor for resistance of monopiles to instability = 1.1 [27]
N_{Rk} and $M_{y,Rk}$ = resistances for normal force and moment.

The normal force resistance (N_{Rk}) and moment resistance ($M_{y,Rk}$) can be determined by:

$$N_{Rk} = \frac{Af_y}{\gamma_m} \tag{4.24}$$

$$M_{y,Rk} = \frac{D^3 - (D-2t)^3}{6}\frac{f_y}{\gamma_m}. \tag{4.25}$$

The reduction factor χ_z can be determined from figure 4.4. For hollow sections of S355 steel, curve *a* shall be used [27]. The non-dimensional slenderness parameter λ can be calculated by equation:

$$\lambda = \sqrt{\frac{Af_y}{N_{cr}}}. \tag{4.26}$$

In equation 4.26, N_{cr} is the normal Euler buckling force. This can be calculated via

$$N_{cr} = \frac{\pi^2 EI}{L_{buck}^2} \tag{4.27}$$

where, L_{buck} is the buckling length equal to twice the total length of the system.

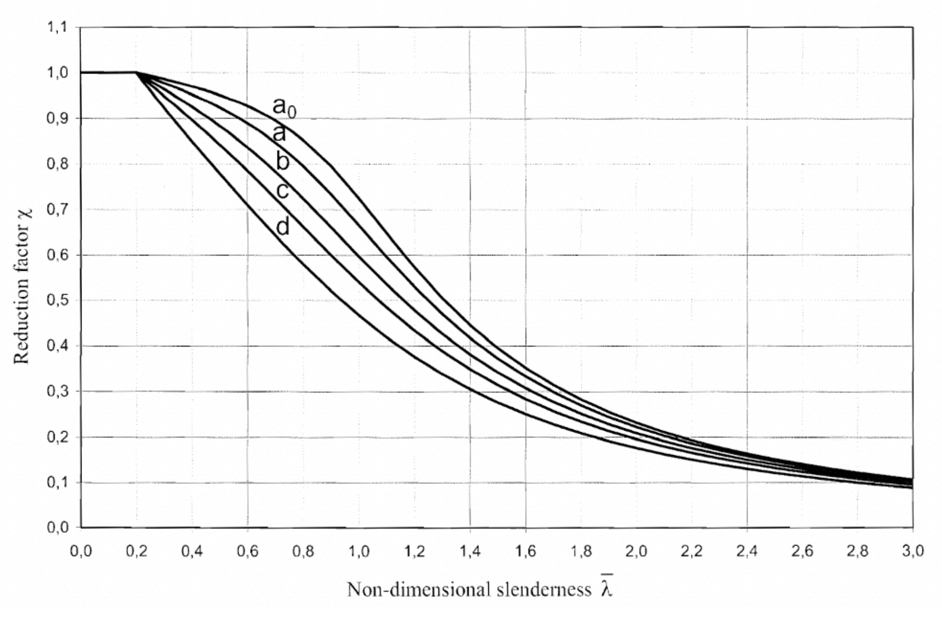

Figure 4.4: Buckling curves

The coupling term k_{yy} for the assumption that the section has elastic cross-sectional properties [27], can be found via:

$$k_{yy} = C_{my}C_{mLT}\frac{\mu_y}{1 - \frac{N_{Ed}}{N_{cr}}}. \tag{4.28}$$

Here, C_{my} can be calculated using the equation:

$$C_{my} = 1 - \frac{N}{N_{cr}}. \tag{4.29}$$

The moment factor C_{mLt} is 1.0 [27]. And finally, the additional term μ_y, that can be found through equation:

$$\mu_y = \frac{1 - \frac{N_{Ed}}{N_{cr}}}{1 - \chi \frac{N_{Ed}}{N_{cr}}}. \tag{4.30}$$

4.1.3. Results ULS analysis

Both checks were conducted along the entire length of the structure, with the results presented in Table 4.1. While both designs passed the tests, it is noteworthy that the yield check for the DOT design is close to the defined limit.

Table 4.1: ULS results. **below mudline*

	DOT	conventional
Von Mises yield check [-]	0.967	0.821
Max. Von Mises yield location* [m]	-1.2	-1.2
Global buckling check [-]	0.882	0.779
Max. global buckling location* [m]	-0.3	-0.3

Based on the ultimate limit state analysis, it can be concluded that the current DOT design is constrained by the yield criterion. In contrast, the conventional turbine design appears to be overdimensioned in terms of structural checks but is limited by its natural frequency constraints.

Both design shall now be further investigated for the fatigue limit state.

4.2. Fatigue Limit State

Turbines experience vibrations throughout their entire operational lifetime due to environmental loads. Even small vibrations within the linear elastic deformation range contribute to material fatigue [31]. That is, even for the smallest vibrations, the material, although it is on micromechanical level, is failing. Fatigue is the most common cause of failures in engineering systems, and therefore an adequate analysis of the fatigue limit state (FLS) is required.

The fatigue calculation is performed according to the DNV standards [32]. Here, the fatigue life is calculated on the basis of the S-N fatigue approach, where the assumption of linear cumulative damage is in place. The Palmgren-Miner rule can be used to calculate the accumulated fatigue damage resulting from the sum of stress reactions due to the wave forcing over its design lifetime. The Palmer-Miner rule is given as:

$$D = \sum_{i=1}^{k} \frac{n_i}{N_i} = \frac{1}{\bar{a}} \sum_{i=1}^{k} n_i \cdot (\Delta\sigma)^m \leq \eta = \frac{1}{DFF} \tag{4.31}$$

where:

	D	= accumulated fatigue damage
	n_i	= number of stress cycles for certain stress range
	N_i	= number of stress cycles to failure at a constant stress range $\Delta\sigma_i$
	$\bar{a}$	= intercept of the design S-N curve with the log N axis
	m	= negative inverse slope of the S-N curve
	k	= number of stress blocks
	η	= fatigue usage factor = 1/DFF
	DFF	= design fatigue factor.

To compute the accumulated fatigue damage over the lifetime of the turbine, the dynamic response to a wave load should be calculated. The method for this is described in section 4.2.1. The input for the computation is given in section 4.2.3 and the calculation and results are given in sections 4.2.5 and 4.2.6.

For this analysis the design fatigue factor is assumed to be 1 [33], meaning a 5-year inspection interval that is carried out afloat is in place. Wind forcing is neglected in this analysis, because it is assumed constant. As we are looking into the differences between the two designs and their fatigue behaviour over the lifetime, for simplicity we only consider the power production load case. In this load case, the wind turbine is in operation and connected to the electrical grid.

4.2.1. Dynamic fatigue model

To find the dynamic response to the environmental forces, a dynamic model is set up, shown in figure 4.5. Fatigue is a predominantly dynamic phenomenon, aspects as mass, structural stiffness, soil stiffness and damping should be included. The topmass with inertia, represents the RNA and the rotational spring at the mudline is already calculated with equation 2.4. The model consists of 4 segments. Segments 1 and 2 are chosen in such a way again, that the wave force is located at an intersection. Segments 3 and 4 represent the slipjoint and tower, respectively. For both the slipjoint and tower, the average of the linear increasing diameter of the structural part is used.

The effects of the hydrodynamic added mass for the submerged part is neglected in this research. It is proven that the effects of the hydrodynamic added mass on the natural frequency is very small [34]. Its effect on the first mode shape is in the range of 0-2%. Because we are mainly interested in the behaviour of the natural freuquency, the hydrodynamic added mass can be neglected.

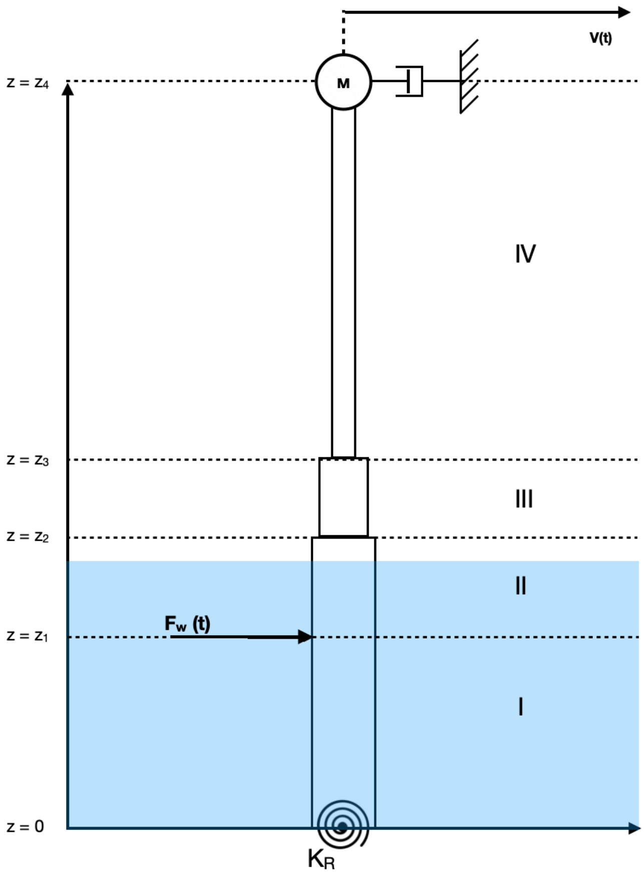

Figure 4.5: Dynamic model FLS

The damper shown in the figure represents the aerodynamic damping of the rotor. Besides the aerodynamic damping, there is also hydrodynamic, structural and soil damping. The influence of these is negligible compared to the aerodynamic damping and is therefore not included.

The governing equations of motion for the system are set up via the Lagrangian method [35]. Here, the derivation of the equations of motion for an elastic system interacting with a moving object is introduced, these equations given by equations:

$$\lambda_{u_n} - \frac{\partial}{\partial t}\lambda_{\dot{u_n}} - \frac{\partial}{\partial z}\lambda_{u_{n_z}} + \frac{\partial^2}{\partial z^2}\lambda_{u_{n_{zz}}} + \frac{\partial^2}{\partial z \partial t}\lambda_{\dot{u_{n_z}}} + \overline{q} = 0; z \neq L, n = 1..4 \tag{4.32}$$

$$L_V - \frac{d}{dt}L_{\dot{V}} + Q - R_{\dot{V}} = \left[-\frac{\delta}{\delta x}\lambda_{\overline{u_{4_{zz}}}}\right]; z = L \tag{4.33}$$

$$L_{\phi} - \frac{d}{dt}L_{\dot{\phi}} + M = \left[\lambda_{\overline{u_{4_{zz}}}}\right]; z = L \tag{4.34}$$

Due to the inclusion of damping at the topside, equation 4.33 is expanded with the Rayleigh dissipation function R. The dot-notation is the definition of the time derivative of that variable. The sub-notation is the partial derivative with respect to the sub-notated variable.

In these equations λ is the beams Lagrangian density function, described in equation 4.35, and L is the Lagrangian of the topside of the system. For a topside, that can be expressed as a concentrated mass with rotating inertia, the Lagrangian can be given as equation 4.36.

$$\lambda = \frac{1}{2}\rho A\dot{u}_n(z,t)^2 - \frac{1}{2}EI\mathrm{u}_{\mathrm{n}_{zz}}(z,t)^2 \tag{4.35}$$

$$L = \frac{1}{2}m\dot{V}(t)^2 + \frac{1}{2}J\dot{\phi}(t)^2 \tag{4.36}$$

Q and M are the shear force and moment at the location of the topside (z=L). $V(t)$ is the horizontal displacement of the topside and $\phi(t)$ is the rotation of the topside. m and J are the mass and moment of inertia around the tower axis of the RNA. The Rayleigh dissipation function R is given as:

$$R = \frac{1}{2}c_{aero}\dot{V}^2, \tag{4.37}$$

where, c_{aero} is the aerodynamic damping coefficient in this case.

Evaluating for the functions 4.32, 4.33 and 4.34 for the system specific beam Lagrangian density function, topside Lagrangian and Rayleigh dissipation function, the following well known governing equations are found:

$$\rho A_n \frac{\delta^2 u_n}{\delta t^2} + EI_n \frac{\delta^4 u_n}{\delta z^4} = 0; n = 1..4, \tag{4.38}$$

$$m\ddot{V} - EI_4 \frac{\delta^3 u_4}{\delta z^3}\bigg|_{z=L} - c\dot{V} = 0, \tag{4.39}$$

$$J\ddot{\phi}_x + EI_4 \frac{\delta^2 u_4}{\delta z^2}\bigg|_{z=L} = 0. \tag{4.40}$$

We find the Euler-Bernouilli beam equations for beams 1 to 4 (4.38) and the force and moment equilibrium at the location of the topside z=L (equations 4.39 and 4.40).

The latter two equations act as compatibility conditions for the beam at the location z=L. The compatibility conditions at z=0 are given by:

$$u_1(0) = 0, \tag{4.41}$$

$$EI_1 \frac{\partial^2 u_1}{\partial z^2}\bigg|_{z=0} = k_r \frac{\partial u_1}{\partial z}\bigg|_{z=0}. \tag{4.42}$$

The interface conditions between the segment are of the same form as equations 4.10 - 4.14. Finally, the compatibility conditions between beam segment 4 and the topside are given by the equations:

$$V(t) = u_4(L, t), \tag{4.43}$$

$$\phi_x(t) = \frac{\partial u_4(z, t)}{\partial z}\bigg|_{z=L}, \tag{4.44}$$

implying the fixed connection between the beam and the topside. Because the wave excitation is assumed to be purely harmonic, the general steady-state solution to this boundary value problem can be written as:

$$u_n(z, t) = U_n(z)e^{I\omega t}, \tag{4.45}$$

where ω is the frequency of the forcing. Filling in this general solution in the system above, the governing equations of motion in the frequency domain can be found.

4.2.2. Aerodynamic damping

Consider a tower top in motion for a simple illustration of aerodynamic damping. As it moves into the wind, the blades experience a slight increase in wind speed. This movement results in an additional aerodynamic force that opposes the motion of the tower top, reducing its eventual displacement. Similarly, when the tower top moves backward, the aerodynamic force decreases, minimizing its motions. This phenomenon is called aerodynamic damping as it is a function of the velocity. It should be mentioned that aerodynamic damping only occurs during power production. An analytical expression, for a constant rotation speed turbine, for the aerodynamic damping ratio is:

$$\xi_{AD} = \frac{c_{aero}}{c_{\text{crit}}} = \frac{\frac{1}{2} N \rho_a V_\Omega c \frac{\partial C_L}{\partial \alpha}}{2 m \omega_n}, \tag{4.46}$$

where:
- ρ_a = air density [kg/m^3]
- N = number of blades [-]
- V_Ω = rotational speed of the blade element [rad/s]
- c = blade chord length [m]
- $\frac{\delta C_L}{\delta \alpha}$ = lift coefficient derivative = 1 [-]

The critical damping coefficient: $c_{crit} = 2m\omega_n$ [36]. And thus we can derive the equation for the aerodynamic damping c_{aero}. The aerodynamic damping for a 100m diameter rotor is calculated to be 216475 Nm/s.

4.2.3. Wave data input FLS

In this study only the harmonic wave force is considered as input, being the main contributor to the structural fatigue. The wave force is again simulated as a harmonic point force at 1/3 below the water level. The water level is considered to be constant.

T_p (s) \ H_{m0} (m)	[0-1[	[1-2[	[2-3[	[3-4[	[4-5[	[5-6[	[6-7[	[7-8[
[1-2[	112	-	-	-	-	-	-	-
[2-3[	2685	-	-	-	-	-	-	-
[3-4[	8202	315	-	-	-	-	-	-
[4-5[	9413	4400	1	-	-	-	-	-
[5-6[	6220	11534	197	-	-	-	-	-
[6-7[	4326	9277	4625	12	-	-	-	-
[7-8[	2674	3503	5220	1568	2	-	-	-
[8-9[	2175	2044	1314	1880	489	5	-	-
[9-10[	1825	1107	371	443	340	67	2	-
[10-11[	1885	810	80	68	100	61	1	-
[11-12[	1183	784	34	1	30	38	14	-
[12-13[	873	607	35	1	1	5	4	-
[13-14[	666	330	15	-	-	1	2	-
[14-15[	584	264	10	-	-	-	-	-
[15-16[	489	73	7	-	-	-	-	-
[16-17[	379	55	4	-	-	-	-	-
[17-18[	219	7	-	-	-	-	-	-
[18-19[	129	11	-	-	-	-	-	-
[19-20[	76	10	-	-	-	-	-	-

Figure 4.6: Joint scatter diagram HKN *(2005-01-01 - 2016-01-01)*

For the fatigue analysis we are interested in the steady-state response of the beam to the waves. As input for the wave forcing, the scatter diagram, shown in figure 4.6 at the location, of significant wave height and peak period is used. This is obtained from The Netherlands Enterprise Agency (RVO), which publicly provides the site environmental characteristics. The omnidirectional scatter diagram, capturing data from 2005 to 2016, represents bin occurrences based on 1-hour averages [37]. For this analysis, utilizing the omnidirectional scatter diagram is a conservative approach, as it assumes that all bending stresses accumulated over the lifetime are concentrated at a single point. In reality, wave forces are applied from multiple directions, resulting in a more distributed stress profile. The wave force, as a function of height and period, can be calculated via the method described in Appendix A.

For the analysis the average of each bin is used. It should be noted that taking the average of the period for each bin, could have a negative effect on the accuracy. As different wave periods, and thus frequencies, result in different dynamic reactions, especially around the natural frequency of the system.

4.2.4. Amplitude Frequency Response Function

The horizontal displacement of the topside of the structure, in the frequency domain, to a 1.5 meter wave is depicted in figure 4.7. Due to the introduction of damping, the solution has a real and an imaginary part. It can be clearly concluded that around the natural frequencies the imaginary part becomes governing as the system is mainly driven by the aerodynamic damping. The magnitude of the maximum steady-state response to the harmonic loads can be derived as the absolute value of the real and imaginary part.

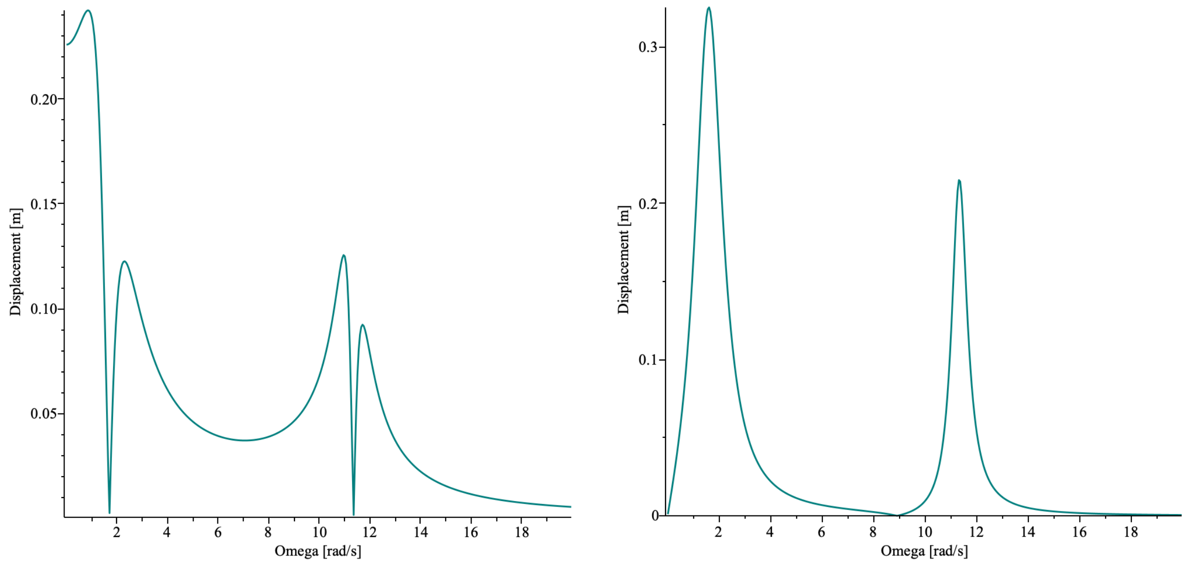

(a) Real part

(b) Imaginary part

Figure 4.7: Horizontal displacement topside conventional turbine

The total magnitude of the displacement to the same wave, for a range of forcing frequencies, of both the conventional and DOT-design are plotted in figure 4.8. The first and second eigenfrequencies can be identified from the peaks in the response. The natural frequencies of the two designs coincide at 1.7 rad/s (=0.27Hz). The second eigenfrequency differs slightly. This can be clarified when we look at the mode shape of the vibration. The second mode shape mainly vibrates in the middle parts of the structure, where the moment of inertia of both designs differentiate.

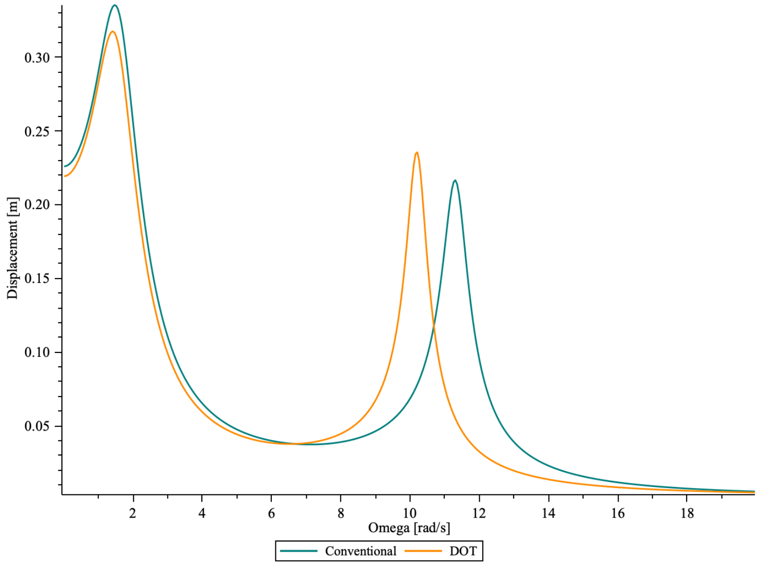

Figure 4.8: Absolute horizontal displacement topside

4.2.5. Fatigue calculation

With the complete dynamic model and the wave input, we can find the stress ranges for each wave frequency. Looking at figure 4.3a we find that the maximum bending stress occurs around the mudline. With equation

$$\sigma_x = \frac{M}{W}\gamma_e\gamma_s, \tag{4.47}$$

the maximum bending stress can be calculated. Here, M is the bending moment, which can be derived from the displacement along the length of the system with the relationship described in equation 4.5. W is the elastic section modulus. γ_e is the environmental safety factor, which is equal to 1.0 [8], and γ_s is the wave spreading factor. For this analysis the wave spreading factor is set to 0.85, which is the average factor for the Northern North Sea. The maximum bending stress as a result to a 1.5m wave for a frequency range can be calculated, the results for both turbines is depicted in figure 4.9. The wave frequency ranges from 1.5s to 19.5s, being equal to 4.2 rad/s to 0.32 rad/s, therefore the plotted frequency range is from 0 to 5 rad/s.

From equation A.8 in Appendix A it can be easily seen that the wave force scales linearly with the wave height for an inertia dominated wave. Therefore, the bending stress can also be scaled linearly with the wave height. Together with the joint scatter diagram the occurrences of stress ranges over the design life time of the turbine can be computed.

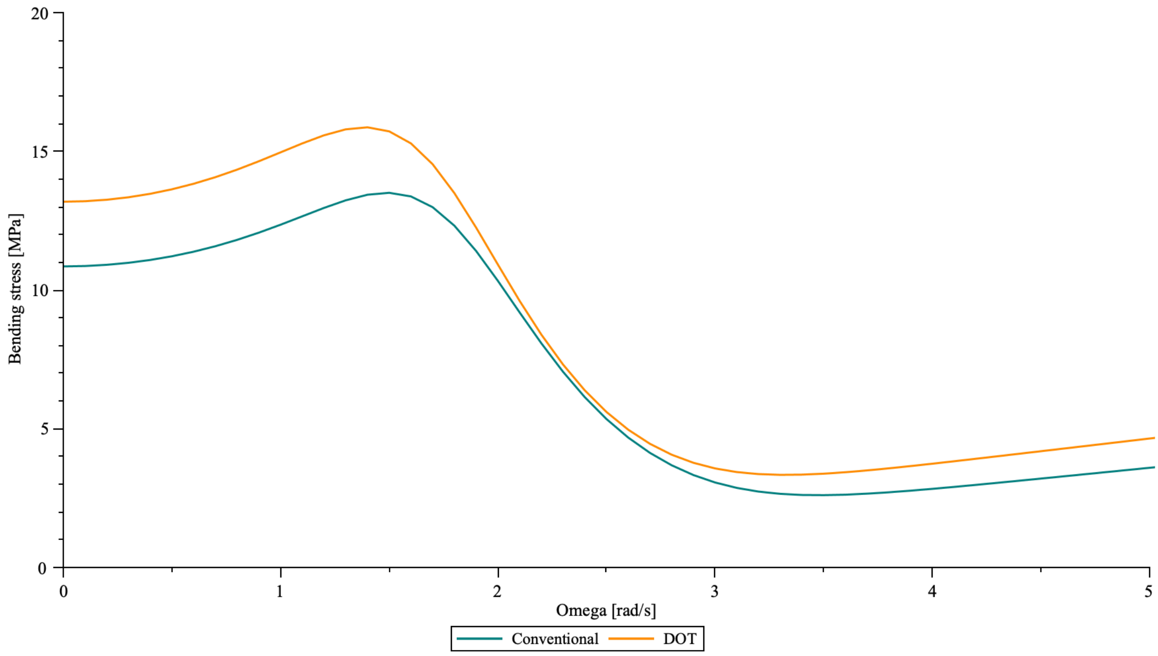

Figure 4.9: Stress Frequency Response Function - 1.5m wave

For tubular structures submerged in seawater with cathodic protection to reduce corrosion the S-N curves are shown in figure 4.10. The S-N curves are obtained from fatigue tests and can be found in the relevant standard [32]. The curves relate the stress range (S) with the number of cycle (N) for the material to fail.

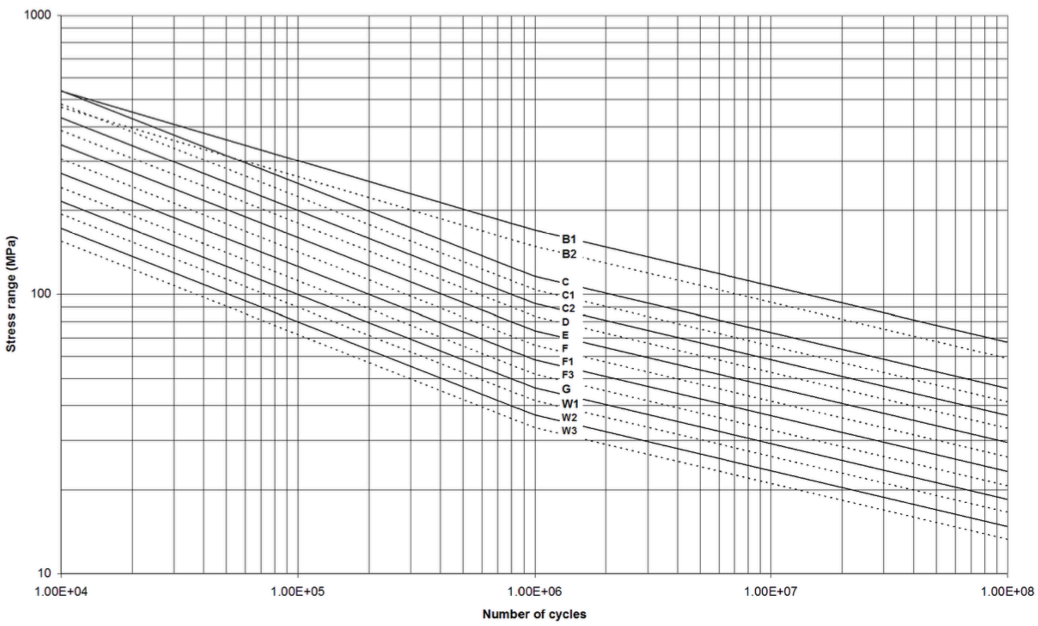

Figure 4.10: S-N curves for steel in seawater [32]

4.2.6. Fatigue Limit State Results and Conclusions

For this case the results of the fatigue analysis are summarized in table 4.2. The unity check can not exceed 1.0 to pass the test. Because the DOT turbine has a slimmer monopile, the resulting stress is greater compared to the conventional turbine. This easily visible from figure 4.9. The DOT turbine only passes the test for the higher grade steal B2, where the conventional turbine also stays within the limits for the lower grade steel C.

Table 4.2: Results FLS analysis

S-N curve	DOT	Conventional
B2	0.35	0.23
C	1.22	0.78
C1	2.11	1.35
C2	3.72	2.39

As previously noted, the wave input for the fatigue limit state check is considered purely unidirectional. However, this approach overlooks a significant effect. When wind-wave misalignment occurs, the wind and wave forces are not aligned. The rotor, along with the associated aerodynamic damping, is aimed to be oriented perpendicular to the incoming wind. Consequently, the aerodynamic damping, which plays a crucial role in mitigating fatigue vibrations induced by wave action, is not aligned with the incoming waves. The side-to-side motion has insignificant aerodynamic damping. This way the structure is prone to large side-to-side vibrations. [38]

Any wind-wave misalignment would induce an undamped vibration. This is depicted in figure 4.11, where the bending stress response in the non-damped side-to-side direction of the DOT turbine is plotted. In line with the expectations, the response, especially around the natural frequency, increases significantly.

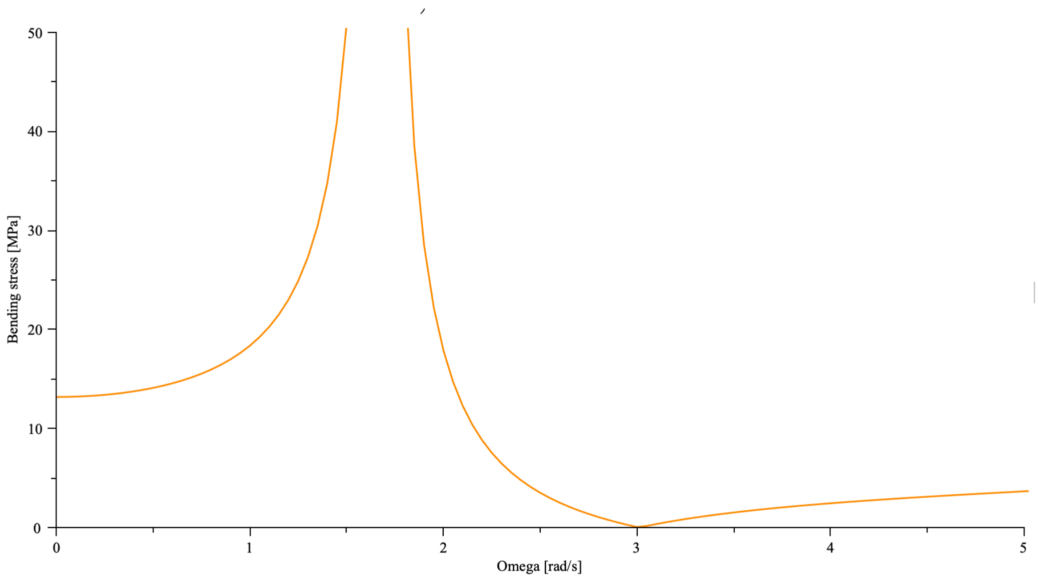

Figure 4.11: SFRF side-to-side motion - 1.5m wave

Interestingly, it is observed that the bending stress located at the mudline almost goes to zero for a forcing frequency of 3 radians per second. This can be explained by looking at the different mode-shapes of the vibrations for different forcing frequencies. Figure 4.12 shows the vibrating modeshape of the DOT-turbine for 5 different forcing frequencies Ω. For the forcing frequency Ω = 2 radians per second, the bending at the mudline is almost zero. Notably, when Ω is 2 radians per second, the displacement is at its maximum, which aligns with the system's proximity to its natural frequency.

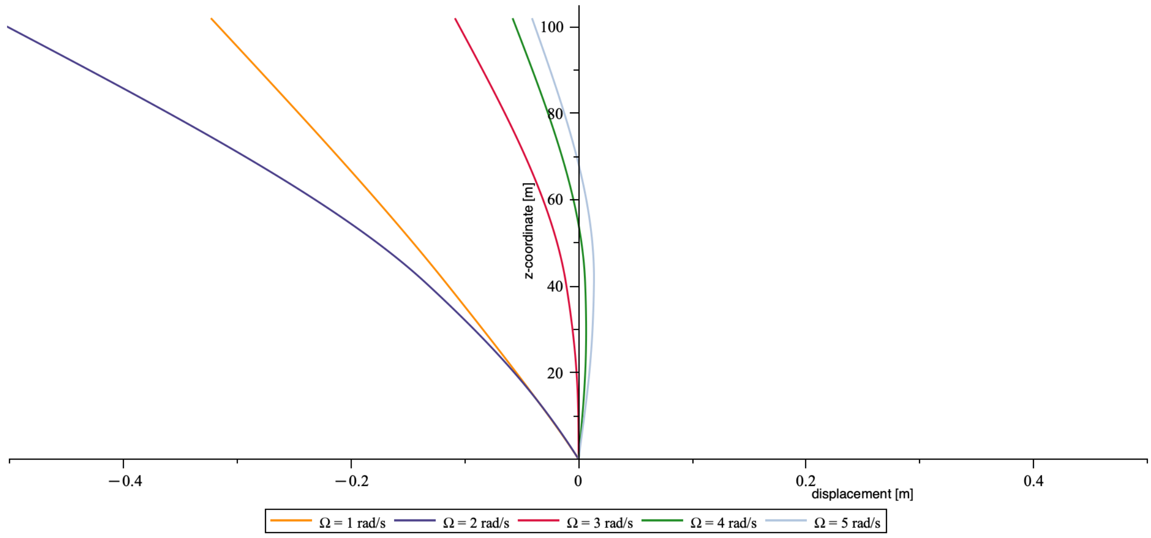

Figure 4.12: support structure modeshapes

Looking at the higher frequencies, the tower bending shifts higher up the turbine. Consequently, the maximum stress frequency response function varies depending on the location along the turbine, as shown in figure 4.13. For Ω being higher than the natural frequency, the bending stress increases as we move further above the mudline. In contrast, for forcing frequencies lower than the natural frequency, performing the FLS check at the mudline is conservative. From the scatter diagram in figure 4.6 it can be derived that only 6% of all wave-induced bending stresses are undervalued from the maximum at the mudline. Consequently, 94% of the bending cycles are equal or overvalued. Therefore, the FLS evaluation at the mudline can be considered conservative, and is thus valid for the total system.

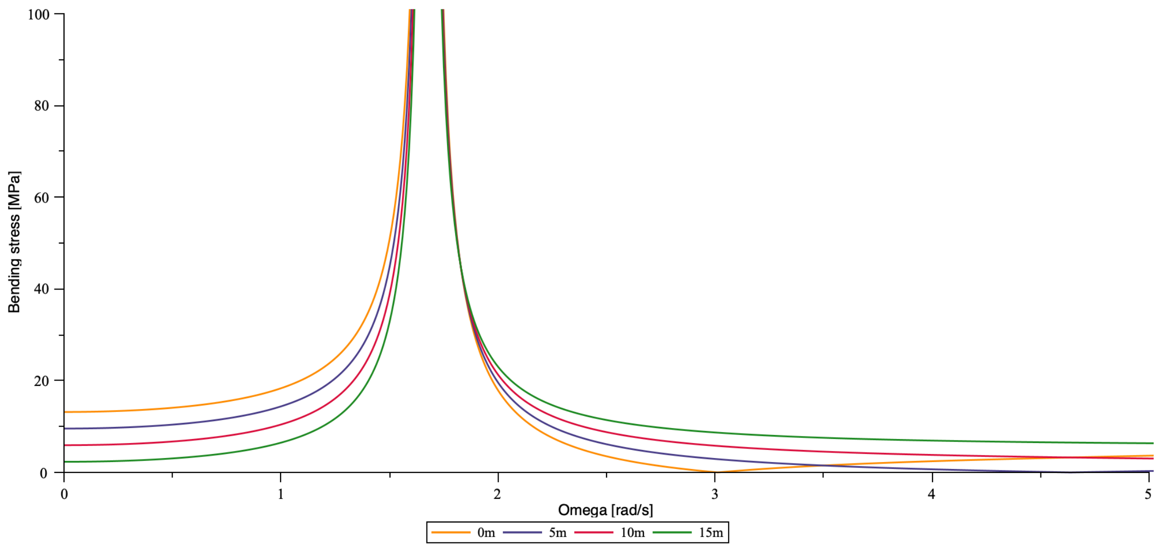

Figure 4.13: SFRF for different heights above the mudline

There are several existing techniques to reduce undamped side-to-side vibrations. Some examples are: individual pitch control [39], acceleration feedback control [40] and structural control like mass dampers. The latter are shortly introduced in chapter 5. With the same goal to reduce the response in the side-to-side direction, in the next chapters the effectiveness of a gyroscopic damper is researched.

5
Gyroscopic Dampers

The use of dampers in offshore wind turbines is not a novelty and has been studied by many researchers. The techniques vary from simple passive tuned mass dampers (PTMD) [41] to active tuned mass dampers (ATMD) [42] and liquid column dampers (LCD) [43]. All of these methods share the same goal: to improve stability and reliability, reducing the required material and maintenance. A major downside of these techniques is the added weight to the structure. As shown in chapter 4, this added weight increases the amount of steel required.

Given that the topside of the DOT turbine is 50% lighter than a conventional turbine, the negative side effect of adding extra weight on the topside of the system is therefore (partially) nullified. Apart from the added complexity, the implementation of a damper in the topside of an offshore wind turbine can have great benefits. The damper reduces the transmission force and the displacement of the system, which means that the maximum displacement of the maximum limit state is smaller. However, dampers mainly reduce fatigue loads on the support structure during the lifetime of the turbine. This can result in a more optimal support structure design. In addition to this, due to the reduced response of the top side generated by cycling loads such as wind and waves, the interaction between the blades and the incoming wind becomes more stable, improving the efficiency of the turbines [44].

A technique that has not yet been extensively studied is the use of a gyroscope as a damper in offshore wind turbines. The primary advantage of gyrostabilisers is their ability to generate damping with significantly less added mass compared to conventional dampers, because of the use of spinning energy. Conventional dampers work by resisting motion, and the principle behind this lies in inertia — an object's resistance to changes in its state of motion, as first described by Newton. Moving a large mass requires considerable force, which is why conventional dampers rely on significant mass to absorb vibrations. However, when an object spins at high speeds, it is also resistant to motion, known as gyroscopic inertia. This means a spinning object can achieve the same damping effect with far less mass, making spinning dampers more efficient and compact.

Additionally, the damping direction can be precisely controlled by adjusting the configuration of the system Finally, the damping can be easily tuned by varying the rotational speed of the gyroscope.

In the studies where gyrostabilisers have been researched, only the for-aft movement in the time domain is assessed [7]. In this research, the orientation and configuration of the gyrostabiliser are chosen to reduce the motion in the undamped side-to-side direction, to reduce the fatigue load in that direction.

In this chapter, the dynamics of a gyroscope are explained, followed by the introduction of the gyrostabiliser configuration that is proposed in this research.

5.1. Gyroscopic effects

There are two main gyroscopic effects: its rigidity in space and precession. The use of these effects for dynamic systems date back to the 1800's, where the rigidity in space effect is used for navigational purposes [45], [46]. Today, this technique can still be found in flight instruments in airplanes, as shown in figure 5.1. Here, due to the rotational inertia of the gyroscope, the instrument always remains level to the earth, independent of the movement and orientation of the airplane. Using this effect, the pilot is always able to visualize the orientation of the aircraft. Other uses of the rigidity in space effect, involve the stabilization of film-making equipment using the same effect [47].

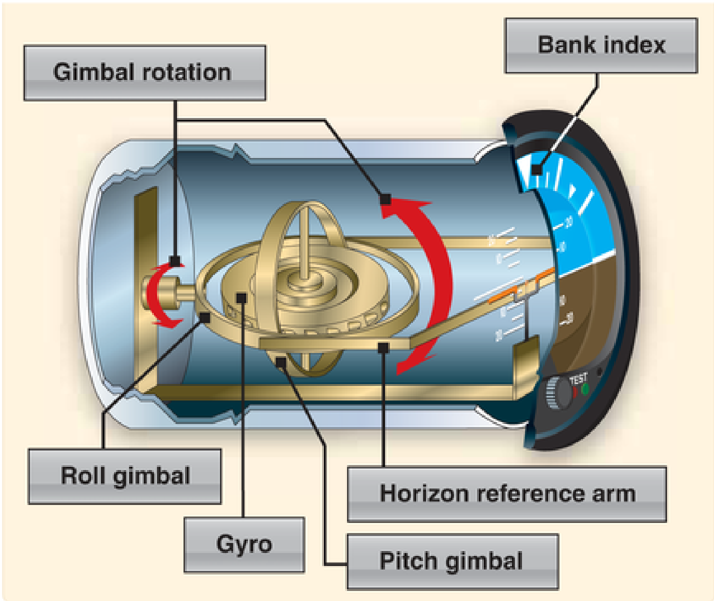

Figure 5.1: Schematics of an aviation instrument using a gyroscope

Precession

Precession is the characteristic change in orientation of a rotating gyroscope when an external force or torque is applied. This behaviour, known as gyroscopic precession, causes the gyroscope to move in a direction that is perpendicular to the applied force, which can be difficult to intuitively grasp. Despite its complexity, gyroscopic precession has several practical and useful applications. A visual representation of torque-induced gyroscopic precession is shown in figure 5.2. Here, L is the angular momentum of the disk around its rotational axis. F_z is the applied force at the edge of the disk, which has a torque around the y-axis of $\tau = F_z * r$, where r is the radius of the disk. The change in the angular momentum around the perpendicular x-axis, due to this torque, is called gyroscopic precession.

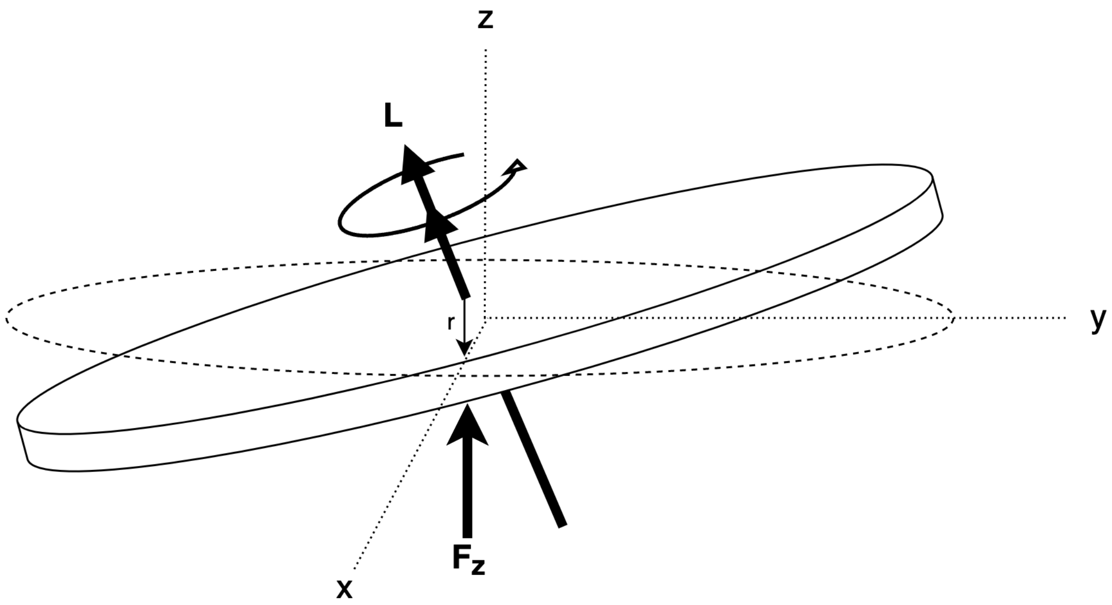

Figure 5.2: Visualization of gyroscopic precession due to a torque

The change of the angular momentum as function of the applied torque can easily be derived from the equation:

$$\tau = \frac{d\mathbf{L}}{dt}. \tag{5.1}$$

5.2. Configuration of a gyrostabiliser

The configuration of the vertical gyrostabiliser (named vertical gyrostabiliser after the orientation of the axle where the disk spins around) is depicted in figure 5.3. The spinning disk with gyricity Ω around the z-axis can rotate freely around the x-axis but is restricted to rotate around the y-axis. Consider the configuration shown in figure 5.3 to be fixed inside the nacelle of the OWT. Due to the restriction around the y-axis, the angle θ is equal to the rotation of the nacelle. This is equal to the rotation of the tower at the location of the topside. The restriction also transfers the moment from the tower to the gyrostabiliser. This moment induces the precession around the x-axis, which is denominated as a variable ϕ.

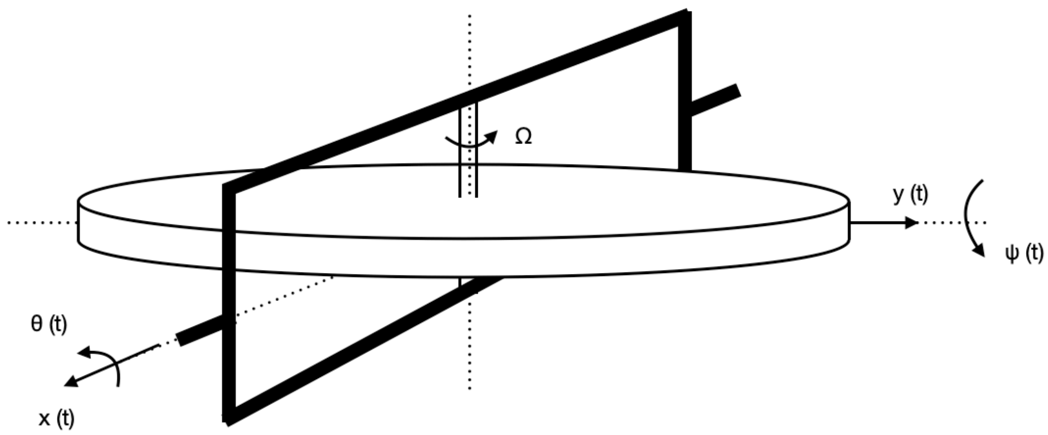

Figure 5.3: gyrostabiliser configuration

This configuration causes the moments in the side-to-side direction, around the y-axis, to be transferred into a rotation of the gyrostabiliser with angle θ, thereby reducing the vibrations in the side-to-side orientation. The restricting rods are assumed to be infinitely stiff and weightless for the sake of simplicity.

Unlike conventional passive mass dampers, this passive gyrostabiliser does not rely on an energy-dissipating system. In typical passive mass dampers, a damping element is used to dissipate energy and mitigate vibrations. However, a damper is not implemented in this case because the precession of the gyrostabiliser is expected to effectively transfer the topside displacement into rotational motion, significantly reducing the vibrations in the undamped side-to-side direction.

6

Gyrostabiliser Modelling

To test the feasibility of the gyrostabiliser in the DOT offshore wind turbine design, a model is set up. The model is split up into two subsystems: the RNA including the gyrostabiliser and the support structure, that is the: tower, slipjoint and monopile. The support structure model and its equations of motions are similar to the dynamic fatigue model, introduced in section 4.2.1, but is expanded to also include the vibrations in the side-to-side direction. The equations of motion of the RNA including the gyrostabiliser are also derived using the Lagrangian mechanism.

6.1. Support structure

For this analysis a beam model with vibrations in the x- and y-direction is set up. The vibrations in the x- and y-direction coindice with the side-to-side and for-aft motion of the tower, respectively. A schematic overview of the model is shown in figure 6.1.

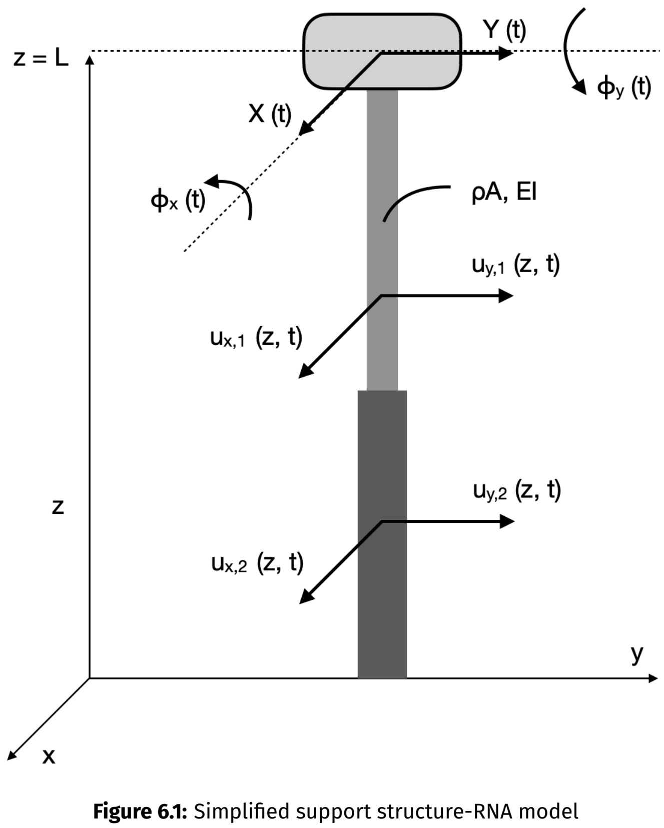

Figure 6.1: Simplified support structure-RNA model

The support structure consists of two beams. Beam 1 represents the tower and slipjoint, where the average cross-area (A), bending stiffness (EI) and density (ρ) are used for the homogeneous beam. Beam 2 denotes the monopile and has the same parameters as the DOT monopile. It is apparent that the compatibility conditions between the top beam and nacelle: $u_x(L,t)$ = X(t), $u_y(L,t)$ = Y(t), $u'_x(L,t) = \phi_y(t)$ and $u'_y(L,t) = \phi_x(t)$ are in place. At the mudline, the soil is represented by the rotational spring given in table 2.3.

$$\rho A \frac{\partial^2 u_{x,y}(z,t)}{\partial t^2} + EI \frac{\partial^4 u_{x,y}(z,t)}{\partial z^4} = 0 \tag{6.1}$$

The equations of motion for the beams, in x- and y-direction, are described by equation 6.1. Here, the axial forcing component is omitted for the fatigue analysis, as the bending stress cycles are governing.

The method of solving equation 6.1 is similar to the method described in section 4.2.1. The differences occur in the equation describing the horizontal balance of forces 4.39. At the location of the gyrostabiliser in the side-to-side direction, there is no aerodynamic damping. Besides this, the moment of inertia of the topside differs in both directions. These values are provided by DOT and are given in table 6.1.

6.2. RNA and gyrostabiliser

The equations of motion for the gyroscope are derived through the Lagragian approach, which is based on the kinetic and potential energy of the system. To obtain the equations of motion for all degrees of freedom, the Lagrangian equation reads:

$$\frac{d}{dt}\frac{\partial L}{\partial \dot{q}_i} - \frac{\partial L}{\partial q_i} = 0, \tag{6.2}$$

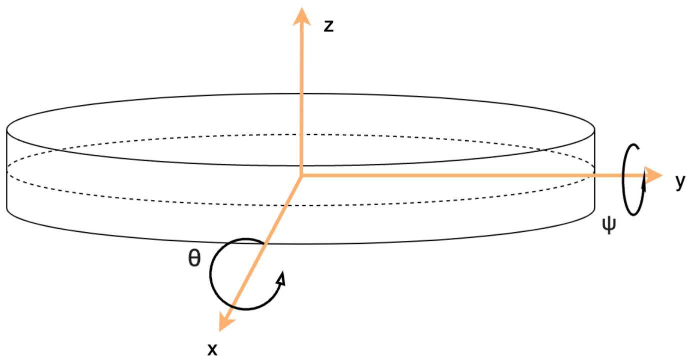

Figure 6.2: Schematic representation of the 4 degrees of freedom of the flywheel

where q_i are the degrees of freedom with $i = 1,2,3,4$. These are referring to the four degrees of freedom seen in figure 6.2, namely: x, y, θ and ψ, respectively. L is the Lagrangian of the RNA and gyrostabiliser system. A function of the kinetic and potential energy of the system:

$$L = T - V \tag{6.3}$$

As we are in the assumption of small vibrations, we can assume that the vertical displacement along the z-axis of the gyrostabiliser is 0. That is, the centre of mass of the disk is stationary in the vertical z-direction, this way only the kinetic term (T) remains in equation 6.3. So, the kinetic energy of a spinning disk with two translational and two rotational degrees of freedom needs to be set up. Assuming a constant thickness of the flywheel, we can describe the kinetic energy expressed in the global coordinate system as

$$T = \frac{1}{2}\frac{M_d}{\pi R^2}\iint_0^{R2\pi} \left(\dot{s}_f^g \cdot \dot{s}_f^g\right) r dr d\eta \tag{6.4}$$

where, we recognize the well-known form for the kinetic energy of a mass: $\frac{1}{2}mv^2$, where:

M_d = the mass of the flywheel [kg]
R = the radius of the flywheel [m]
$\vec{s}_f^g$ = the position vector, from the centre of the flywheel to an arbitrary point on the disk, expressed in the global coordinate system (superscript g), see figure 6.3
η = the angle of the position vector within the flywheel-fixed coordinate system. [rad]
r = the length of vector s [m]

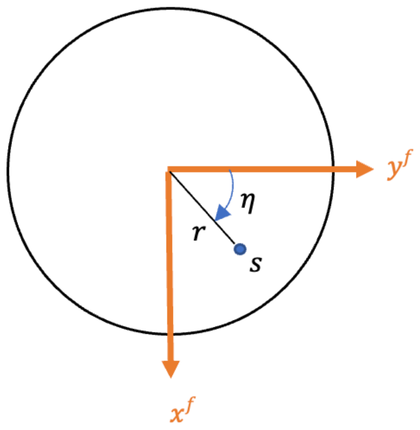

Figure 6.3: Topview of flywheel

Expressing the position vector $\vec{s}_f^f$ in the flywheel fixed coordinate system f, shown in figure 6.3, and by making use of the polar coordinate system gives:

$$\vec{s}_f^f = \begin{bmatrix} r\cos\eta \\ r\sin\eta \\ 0 \end{bmatrix}, \tag{6.5}$$

To express this vector in the global orientated coordinate system, one must multiply this with a rotational matrix. This rotational matrix consists of the multiplication of 3 rotational matrices around the 3 rotational degrees of freedom: η, ψ and θ. η can be seen in figure 6.3 and ψ and θ can be seen in figure 6.2. The derivation of the rotational matrix can be found in Appendix B, but for brevity the definition of Rot_{tot}:

$$Rot_{tot} = \begin{bmatrix} \cos(\eta)\cos(\psi) & -\sin(\eta)\cos(\theta) + \cos(\eta)\sin(\psi)\sin(\theta) & \sin(\eta)\sin(\theta) + \cos(\eta)\sin(\psi)\cos(\theta) \\ \sin(\eta)\cos(\psi) & \cos(\eta)\cos(\theta) + \sin(\eta)\sin(\psi)\sin(\theta) & -\cos(\eta)\sin(\theta) + \sin(\eta)\sin(\psi)\cos(\theta) \\ -\sin(\psi) & \cos(\psi)\sin(\theta) & \cos(\psi)\cos(\theta) \end{bmatrix} \tag{6.6}$$

Including the translational degrees of freedom x and y, the vector $\vec{s}_f^g$ of an arbitrary point on the flywheel in the global coordinate system is given as

$$\vec{s}_f^g = \begin{bmatrix} x(t) \\ y(t) \\ 0 \end{bmatrix} + R_{rot} \cdot \vec{s}_f^f \tag{6.7}$$

To find the velocity vector in the global frame, we simply take the time derivative of this expression. Substitution of this velocity vector in 6.4 followed by integration over the surface of the flywheel and multiplication of the thickness gives the Lagrangian of the flywheel.

$$L_{gyro} = \frac{1}{8}(M_d \left(r^2 \left(\cos(\psi)^2 \cos(\theta)^2 + 1\right) \dot{\eta}^2 - 2r^2 \left(\cos(\psi) \cos(\theta) \sin(\theta) \dot{\psi} + \right.\right.$$
$$\left.\sin(\psi)\dot{\theta}\dot{\eta} - r^2 \left(\cos(\theta)^2 - 2\right) \psi^2 + r^2\dot{\theta}^2 + 4\dot{x}^2 + 4\dot{y}^2 \tag{6.8}$$

As we assume the system small vibrations, we can applying the approximation of small angles, where $\cos(\theta) \approx 1$ and $\sin(\theta) \approx \theta$. Recognizing that the term $\dot{\eta}$ in the Lagrangian is the rotational velocity of the flywheel, expressed as the gyricity of the disk Ω, equation 6.8 can be simplified to

$$L_{gyro} = \frac{M_d \left(2r^2\Omega^2 - 2r^2 \left(\theta\dot{\psi} + \psi\dot{\theta}\right)\Omega + r^2\dot{\psi}^2 + r^2\dot{\theta}^2 + 4\dot{x}^2 + 4\dot{y}^2\right)}{8}. \tag{6.9}$$

To complete the Lagrangian that also includes the RNA, we include the kinetic energy of the RNA. The degrees of freedom are shown in figure 6.1. Y and X are the horizontal displacement of the topside, where ϕ_y and ϕ_x are the rotations of the topside around the respective axis. Then we find the following Lagrangian expression for the whole system:

$$L_{tot} = \frac{M_d \left(2r^2\Omega^2 - 2r^2 \left(\theta\dot{\psi} + \psi\dot{\theta}\right)\Omega + r^2\dot{\psi}^2 + r^2\dot{\theta}^2 + 4\dot{x}^2 + 4\dot{y}^2\right)}{8} + \frac{M_{RNA}(\dot{X}^2 + \dot{Y}^2)}{2} + \frac{J_{RNA,x}\phi_x^2}{2} + \frac{J_{RNA,y}\phi_y^2}{2} \tag{6.10}$$

Where, M_{RNA} is the mass of the rotor-nacelle-assembly. $J_{RNA,x}$ and $J_{RNA,y}$ are the moment of inertia of the RNA around their respective axis. These are provided by DOT and are given in table 6.1.

Table 6.1: Moments of inertia topside

Unit	**Value** $[m^4]$
$J_{RNA,x}$	4370612
$J_{RNA,y}$	7082284

Using the Lagrangian equation 6.10, where we partially derive equation 6.9 to the 5 degrees of freedom: X, Y, ϕ_x, ϕ_y and θ. This way, the five equations of motion, 6.11 - 6.15, for the RNA and gyrostabiliser system are established. Here it can be seen that the is no direct interaction between the beam and the degree of freedom θ.

$$- EI_2 \left.\frac{\delta^3 u_{2,y}}{\delta z^3}\right|_{z=L} + (M_d + M_{RNA})\ddot{Y} - c\dot{Y} = 0 \tag{6.11}$$

$$- EI_2 \left.\frac{\delta^3 u_{2,x}}{\delta z^3}\right|_{z=L} + (M_d + M_{RNA})\ddot{X} = 0 \tag{6.12}$$

$$- EI_2 \left.\frac{\delta^2 u_{2,x}}{\delta z^2}\right|_{z=L} + \frac{\left(M_d r^2 + 2J_{RNA,y}\right)\ddot{\phi}_y}{2} - \frac{M_d r^2\dot{\theta}\Omega}{2} = 0 \tag{6.13}$$

$$- EI_2 \left.\frac{\delta^2 u_{2,y}}{\delta z^2}\right|_{z=L} + J_{RNA,x}\ddot{\phi}_x = 0 \tag{6.14}$$

$$- \frac{r^2 Md \left(\dot{\phi}_y\Omega - \frac{\ddot{\theta}(t)}{2}\right)}{2} = 0 \tag{6.15}$$

From equations 6.11 and 6.12, it can be quickly concluded that the gyrostabiliser acts as a lumped topmass in the translational directions. From equations 6.13 and 6.15, we observe that the gyricity term Ω is the mathematical and physical coupling between the rotation around one axis and its reaction about an axis perpendicular to it, or in term of gyroscopes: precession. In mechanical systems, a velocity term in the equations of motion is normally related to a damping effect. But in this case, no energy is dissipated from the system. The energy is solely transferred into a different direction.

Equations 6.11-6.14 act as the boundary conditions for the beam at the location of the topside. Where equation described the motion 6.15 of the separate degree of freedom θ.

6.3. Systems interaction

Similarly to equations 4.43 and 4.44, at the location of the topside, the deflection and rotation of the beam are equal to the vertical displacement and rotation of the RNA. These continuity conditions also hold for the displacement and rotation in the side-to-side direction.

The gyrostabiliser and beam interact via the internal moment, see equation 4.5 of the beam at the location of the gyroscope. This translates into the angle ϕ_y of the RNA to be equal to the angle ψ of the gyrostabiliser.

In the frequency domain, the two systems in both x- and y-direction, can be solved simultaneously together with the equation of motion for θ, to find the steady-state beam vibrations and the steady-state angle θ of the gyrostabiliser. Here, we also assume the steady-state solution for the angle θ to be of the form:

$$\theta(t) = \Theta_0 e^{I\omega t} \tag{6.16}$$

in which ω is the forcing frequency. Using the continuity conditions at the top side location and filling in the general solutions 4.45 for the beam elements and the general solution 6.16 for the degree of freedom of θ, in the boundary conditions of the beam a system of 17 equations with 17 unknowns is found. This set can be solved in the same manner as described in section 4.2.1.

6.4. Forcing input

To investigate the effects of wave-wind misalignment, it is essential to analyze joint probability scatter diagrams of wind and wave data. These diagrams provide a statistical overview of the simultaneous occurrences of wind and wave conditions, thus we can check for misalignment cases. The joint probability scatter diagram for the turbine location is given in figure 6.4 and is from the same RVO source as mentioned before [37].

WD (°N-from) \ Misalignment (°)	[-195--165[	[-165--135[	[-135--105[	[-105--75[	[-75--45[	[-45--15[	[-15-15[	[15-45[	[45-75[	[75-105[	[105-135[	[135-165[
[-15-15[	0.00	0.15	1.12	1.75	3.79	31.19	60.64	1.28	0.06	0.01	0.00	0.01
[15-45[	0.23	0.95	1.25	2.25	11.73	58.69	24.75	0.06	0.01	0.00	0.02	0.05
[45-75[	1.10	0.96	1.84	8.23	24.34	59.22	3.77	0.10	0.05	0.04	0.06	0.30
[75-105[	1.17	1.66	6.43	13.55	17.91	42.87	13.01	0.90	0.41	0.27	0.46	1.36
[105-135[	2.58	8.30	10.70	6.77	5.76	10.45	34.68	12.69	2.17	1.74	2.32	1.85
[135-165[	10.33	7.43	2.53	1.06	0.99	1.72	16.48	37.17	8.85	5.39	3.53	4.52
[165-195[	3.98	0.70	0.22	0.12	0.15	0.55	13.37	52.40	10.78	4.83	5.07	7.83
[195-225[	0.26	0.04	0.03	0.02	0.07	0.62	38.05	41.04	7.22	5.22	5.42	2.01
[225-255[	0.02	0.01	0.01	0.01	0.07	1.87	63.13	18.07	8.78	6.00	1.84	0.19
[255-285[	0.01	0.00	0.01	0.04	0.47	12.53	43.37	29.71	11.07	2.57	0.22	0.01
[285-315[	-	0.00	0.03	0.27	3.32	9.76	48.23	34.01	4.17	0.19	0.01	0.01
[315-345[	0.01	0.00	0.21	1.48	3.08	10.40	71.17	13.33	0.31	0.01	-	-

Figure 6.4: Joint occurance table of wave direction (WD) and wind-misalignment

For this study, only an unfavorable case is analyzed where there is a 45-degree misalignment between the incoming wind and waves. This specific angle of misalignment is chosen because it represents a scenario in which the aerodynamic damping is significantly misaligned with the wave forcing. Again, the calculated force for a 1.5 meter (H_{m0}) and wave period of 3.5 seconds is used as input.

7 Results

In this chapter, we present and analyze the results obtained from testing the gyrostabiliser designed to reduce undamped side-to-side vibrations in the DOT-design turbine. The primary goal of these numerical experiments is to check the effectiveness of the gyrostabiliser in minimizing side-to-side vibrations and thus minimizing the bending stress at the mudline.

The results discussed here are generated through the dynamic model described in chapter 6. Similarly to the FLS, to reduce computation time the solution is determined using a semi-analytical approach. To be able to thoroughly investigate the effects of the gyrostabiliser on the manner of vibrating of the structure, several other characteristics also are extracted from the model: the natural frequency, the first mode shape, the amplitude and stress frequency response functions in the for-aft direction.

All results have the same wave-force input described in section 6.4. A top-view representation of the incoming wave direction is shown in figure 7.1. The displacement in Y-direction is called the for-aft motion of the turbine. The displacement in X-direction is named the side-to-side motion. In the coming chapter we are mainly interested in this side-to-side motion of the turbine.

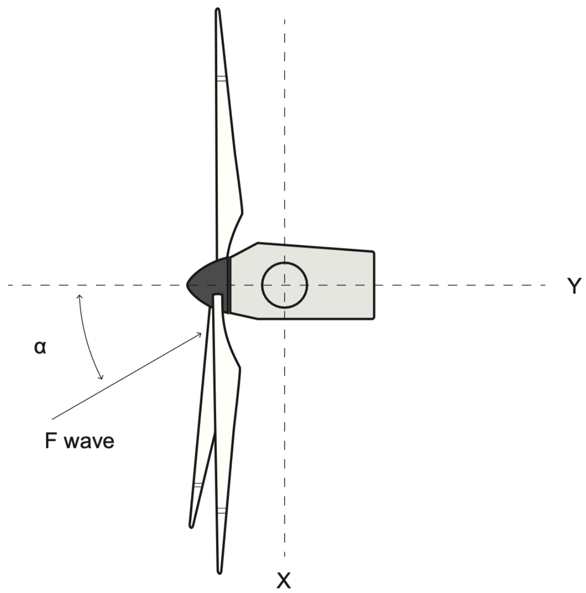

Figure 7.1: Top-view of incoming wave

First, some initial parameters of the gyrostabiliser system are acquired. Secondly, to identify the optimal setup, we evaluate multiple configurations by varying key parameters such as gyroscopic mass and angular velocity. The performance of each configuration was assessed on the basis of its ability to reduce lateral vibrations, as well as the associated bending stress on the structure. Finally, an energy dissipation element is added to the system.

7.1. Gyrostabiliser parameters

When looking at equations of motion 6.11-6.15, we find that the force balance of the gyrostabiliser depends on its mass M_d, radius r and gyricity Ω_d. Regarding the mass, conventional PTMD's are in the region of 1-2% of the total mass of the structure [41], [42]. A mass of 0.75% of the total mass of the structure is chosen, resulting in a disk with a mass of 5000kg. The radius of the disk is based on the dimensions of the nacelle and is set to be 1.5 meters. Finally, the initial gyricity of the disk is chosen to be 50 radians per second. The stress frequency response functions (SFRF) at the mudline, in the side-to-side direction, of the system with and without the gyrostabiliser are depicted in figure 7.2.

It is clear that the gyrostabiliser, in this configuration, does not reduce the magnitude of the maximum bending stress at the mudline. Since the analysis is performed in the frequency domain, only the the steady-state response is captured. However, from literature, it is observed that the transient vibrations are damped by the gyrostabiliser [7].

Although it appears that the response increases, this is not necessarily the case as it might be related to the discretization of the frequency axis in the followed semi-analytical approach. Given the stepsize of 0.01 radians per second, the undamped vibration, within that stepsize-bin the amplitude goes to infinity.

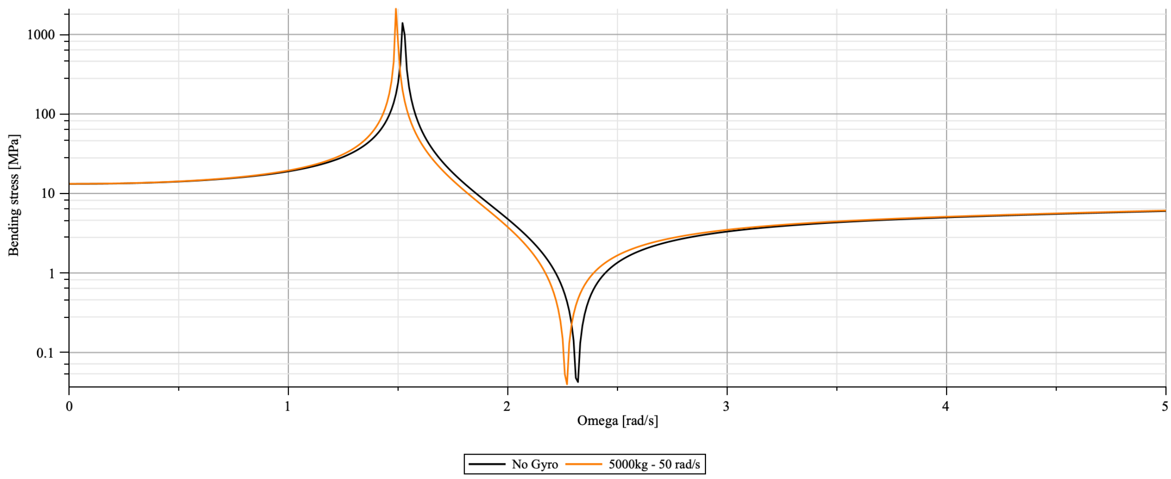

Figure 7.2: Stress Frequency Response Functions in side-to-side direction

In the for-aft direction, no effect is expected of the precession of the gyrostabiliser. The results of the displacement and bending stress in the for-aft direction are depicted in figure 7.3. The expected effect of the added weight can be observed. There is no direct effect of the spinning velocity of the disk on the dynamics in y-direction. From now on, only the results in the side-to-side direction shall be evaluated.

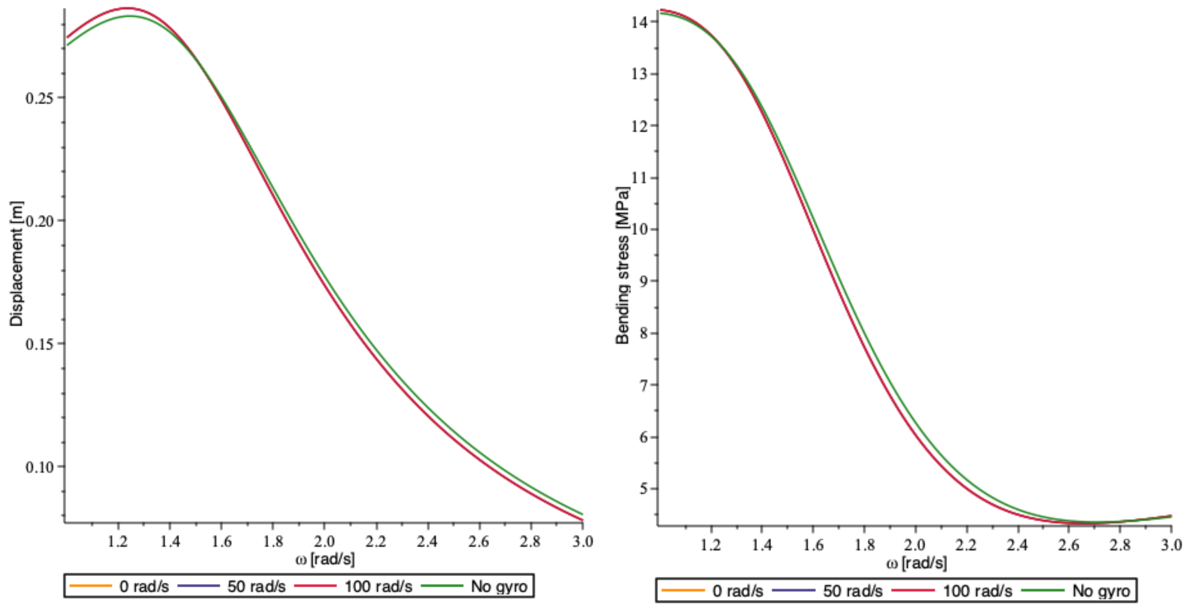

(a) Amplitude frequency response function

(b) Stress frequency response function

Figure 7.3: Results in for-aft direction

The observed shift in the frequency response peaks indicates a change in the natural frequency of the system, likely due to the added weight in the topside. To gain a clearer understanding of this shift and its implications, a sensitivity analysis is conducted. This analysis explores the impact of varying gyrostabiliser weight and gyricity on the natural frequency and performance of the gyrostabiliser.

7.2. Sensitivity analysis

The sensitivity analysis involves evaluating the performance of the gyrostabiliser in various configurations. Parameters such as mass and gyricity are systematically modified to show the effectiveness of the gyrostabiliser in reducing bending stress at the mudline.

In figure 7.2, it can be seen that the peaks are within a certain range of frequencies. Because we are mainly interested in these peaks, we only plot the results in the forcing frequency range of 1-3 radians per second. This way, the accuracy of the semi-analytical solution can be increased while maintaining a sensible computation time.

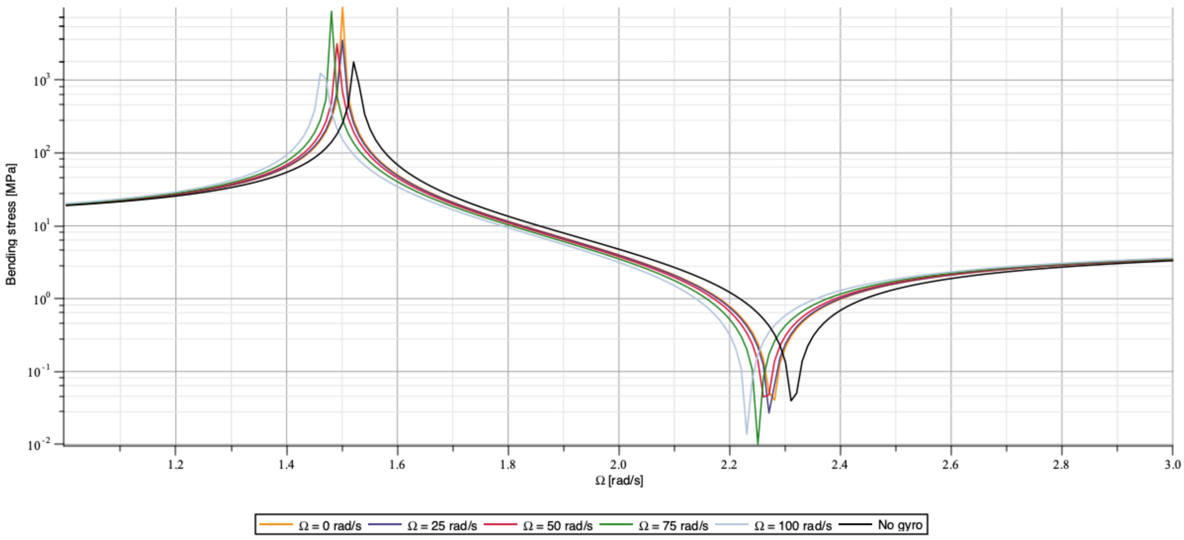

Figure 7.4: Stress Frequency Response Function gyricity alteration | side-to-side direction

7.2.1. Gyricity

Figure 7.4 shows the side-to-side response in the frequency domain for a variety of gyricities of the gyrostabiliser. For a clear comparison, the case of no gyrostabiliser is also included. There is no significant reduction of bending stress visible for the system including the gyrostabiliser. Again, the shift in natural frequency is clearly visible.

Also, it is clear that the maximum value of the stress response varies with changes in gyricity. To investigate this further, the maximum SFRF value is extracted and plotted as a function of gyricity. For a clear comparison, the scenario without a gyrostabiliser installed was also included in the analysis. It was observed that in only a limited number of gyricities, the maximum stress response decreased relative to the base case. From figure 7.5, it can be seen that for several gyricity values the response exhibits a significant spike. This analysis only shows the maximum values of the SFRF and does not say anything about the response at the other frequencies.

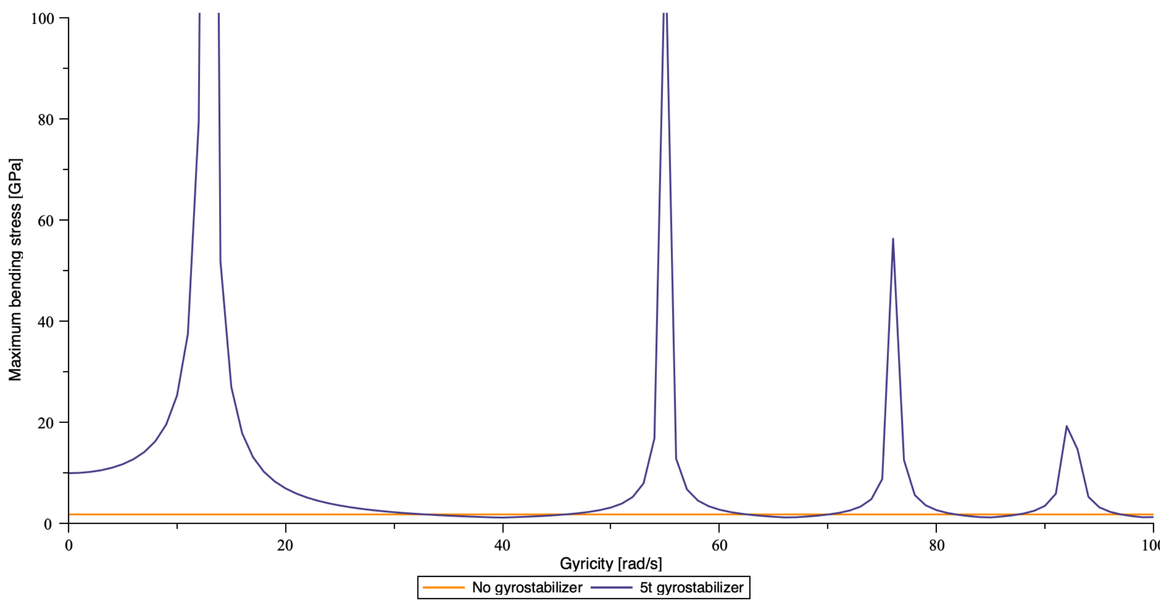

Figure 7.5: Maximum bending stress for different gyricity configurations | side-to-side direction

This behaviour indicates that the natural frequencies of the damper system around the θ axis coincides with the natural frequency of the total system. The natural frequency of the damper is called the precession frequency of the spinning disk. The precession frequency under a known torque is given as [48]:

$$\omega_p = \frac{\tau}{I\Omega}, \tag{7.1}$$

ω_p is the precession frequency in radians per second, I is the second moment of the disk around its rotational axis, Ω denotes the gyricity of the disk in radians per second, τ represents the torque applied to the gyroscope, in this case the internal moment due to the bending of the tower.

To find the configuration of structure and damper, where the natural frequencies of the total system and gyrostabiliser coincide, the equations for both should be set equal and solved for Ω. As seen in figures 7.5, the natural frequency of the system depends on the gyricity and disk mass. This is also true for the frequency of precession.

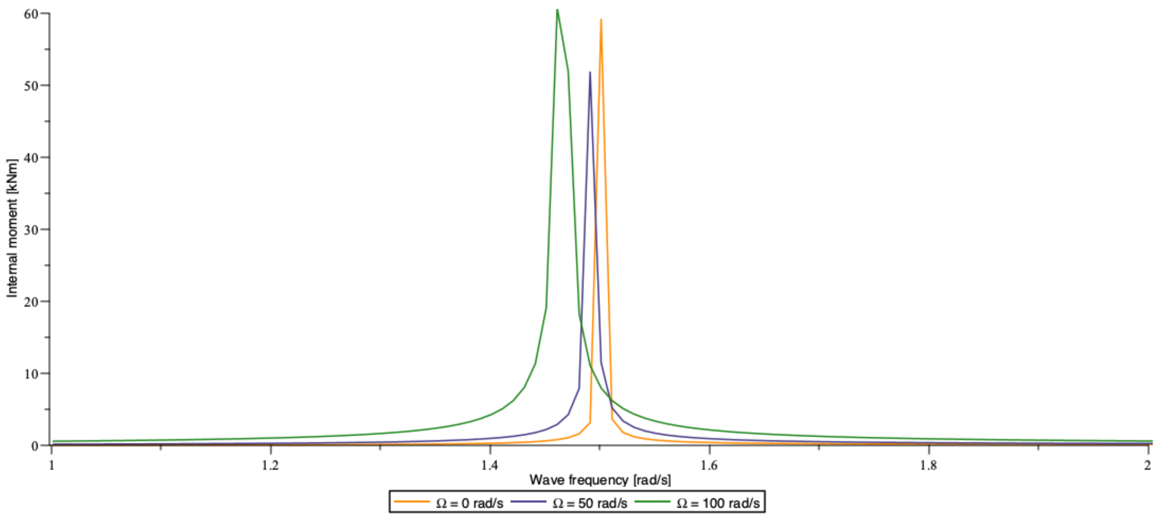

Figure 7.6: Transferred moment from nacelle to gyrostabiliser

Finally, we can look at the internal moment, or torque, at the location of the gyrostabiliser. The torque exerted on the gyrostabiliser as a result of the wave forcing varies over the wave frequencies and is also dependent on the gyricity, as shown in figure 7.6. With this, the gyricities where the precession frequency is equal to the natural frequency of the system can be found. In this thesis no equation for the natural frequency of the system, with gyrostabiliser, is set up. The full derivation and analyis is left for future research.

7.2.2. Mass

Altering the mass of the disk affects the energy stored in the rotating disk. A disk with increased rotational kinetic energy exhibits greater resistance to changes in orientation, thus influencing the overall system response. Additionally, increasing the mass on the topside leads to a reduction in the system's natural frequency. The corresponding response plots of the bending stress at the mudline with a disk gyricity of 50 radians per second, are presented in figure 7.7.

Again, a clear shift in natural frequency is observed. The significantly larger displacement for the 7000kg can also be explained by the natural frequency of the gyrostabiliser to coincide with the systems. Looking at equation 7.1, it can be quickly seen that increasing the mass, decreases the precession frequency. Where the mass of 7000 kilograms, the natural frequency of the gyrostabiliser becomes 1.48 radians per second.

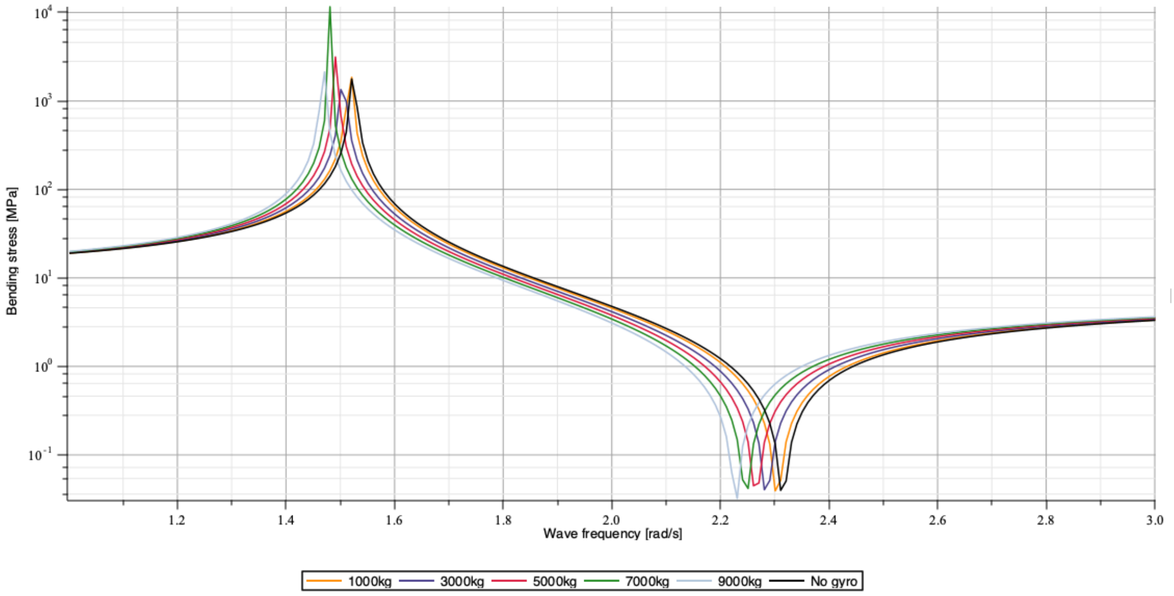

Figure 7.7: Stress Frequency Response Function mass alteration | side-to-side direction

The passive gyrostabiliser, while a useful tool in various engineering applications, does not serve as an absolute stress-reducing technique. This limitation becomes apparent when analyzing its performance in the frequency domain, particularly during the steady-state dominated assessments, such as the FLS checks. The crux of the issue lies in the inability of the passive gyrostabiliser to adequately dampen stress responses under steady-state conditions. The gyrostabilisers ability to dampen vibrations in a certain direction, originates from its rigidity in space. More clearly, its ability to resist change in orientation. To effectuate a change in orientation, the rotating mass should be accelerated. In the steady-state response, all masses are in a steady sinusoidal motion, in phase with the sinusoidal wave forcing. However, it is known from literature, when the motion of the nacelle and the precession of the gyrostabiliser are not in phase, we do experience damping of the vibration [7].

However, the passive gyrostabiliser can function effectively as a frequency skipping tool. By altering the gyricity, it is possible to shift the natural frequencies of the system. This frequency manipulation allows the system to ”skip” over resonant frequencies that would otherwise induce high-stress responses. Similar approaches are already in place in existing wind turbines. By adjusting the pitch of the blade or the torque of the generator [39], the resonating frequencies are omitted. The gyricity of the gyrostabiliser could be included in the controllable parameters to achieve an effective frequency skipping strategy.

The frequency skipping tool is used to avoid resonant conditions and thereby contribute to reducing the stress within the system. This would mean, adding a system that can detect incoming wave frequencies. By actively setting the rotational speed of the disk, the passive system becomes an active system.

7.3. Damped gyrostabiliser

To our current setup, a rotational damper and a spring mechanism around the θ-degree of freedom are added. The main reason for incorporating these elements is to dissipate some of the energy of the system and control the rotation θ of the disk. This way, the response of the system will be reduced. The damper and spring will help to better control the dynamic behavior of the system and manage its overall stability.

The bending stress at the mudline resulting from the same 1.5m wave is shown in figure 7.8. Here, a clear reduction of bending stress can be seen as a result of the gyrostabiliser. Especially for higher gyricities, the reduction is significant. As expected, by using a disk with a higher mass, the effectiveness increased. This is visualized in figure 7.9.

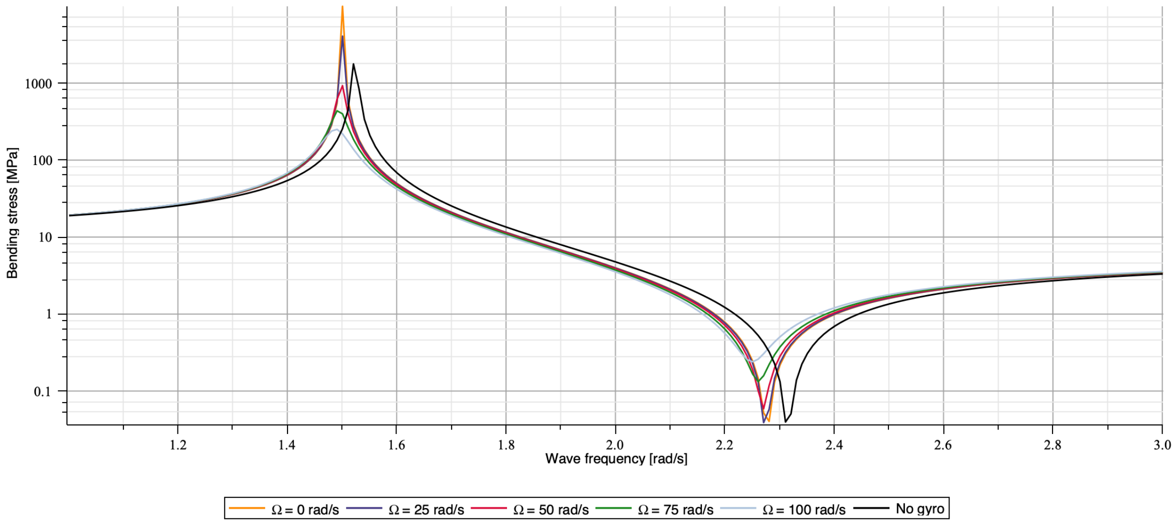

Figure 7.8: Stress Frequency Response Function - gyricity alteration damped 5000kg gyrostabiliser| side-to-side direction

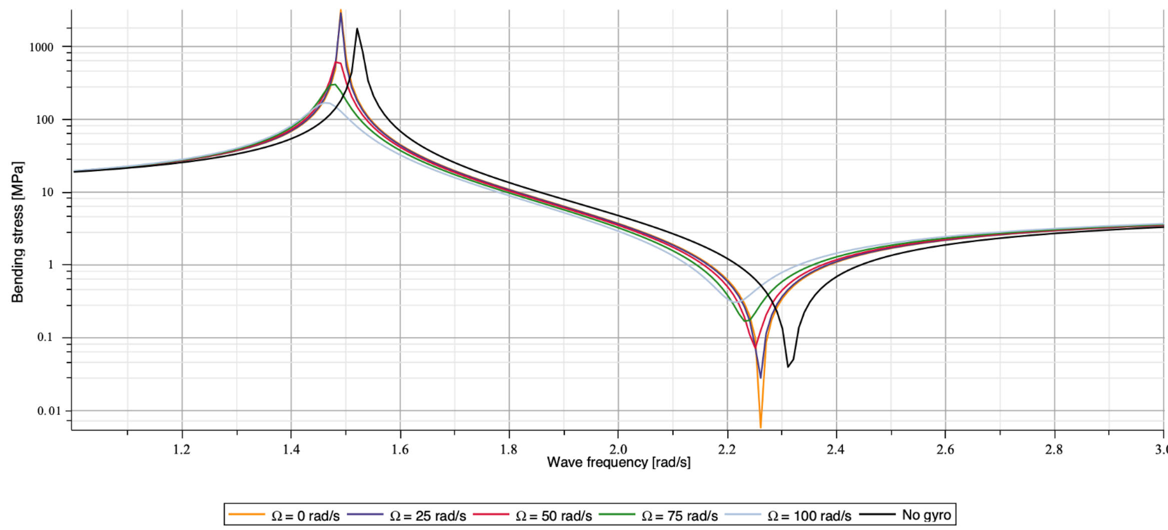

Figure 7.9: Stress Frequency Response Function - gyricity alteration damped 7000kg gyrostabiliser| side-to-side direction

With this configuration, a reduction of the maximum bending stress at the mudline of 90.3% is achieved. This is compared to the undamped case, where no gyrostabiliser is included. The maximum value occurs at a lower forcing frequency, due to the added weight in the topside and the damping effect originating from the .

Again, the maximum bending stress over the wave frequency range 1-3 radians per second is taken and plotted against the gyricity of the disk. The results of bending stress at the mudline for the damped gyrostabiliser system are depicted in figure 7.10.

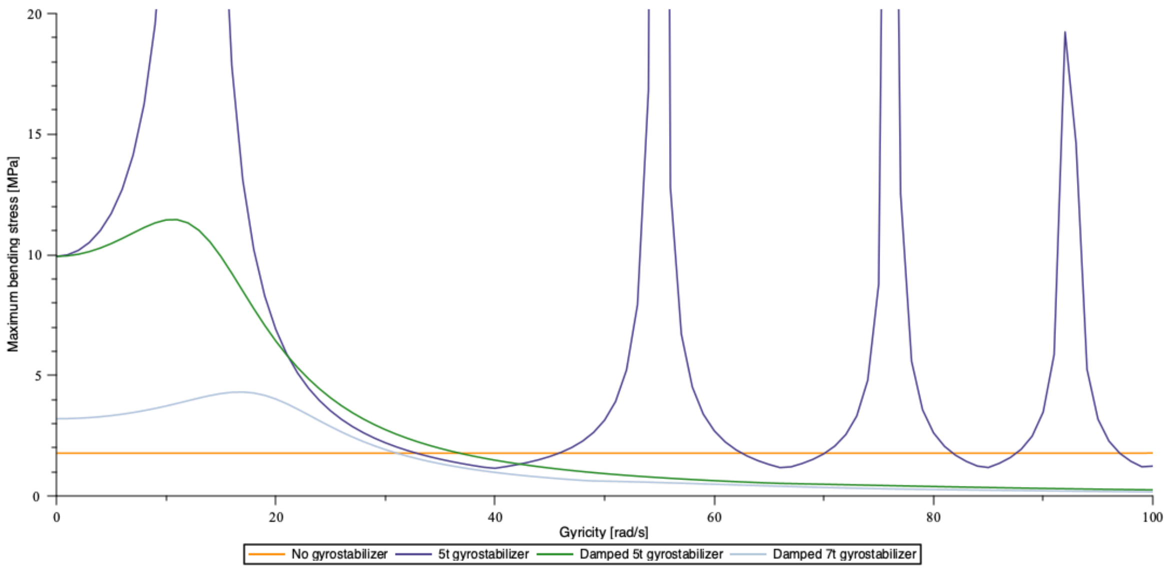

Figure 7.10: Maximum bending stress for different gyricities of damped gyrostabiliser | side-to-side direction

From these results, it can be concluded that from a certain value of rotational velocity, which depends on the parameters of the system, the gyrostabiliser reduces, in fact, the absolute maximum stress response of the turbine.

Finally, we evaluate the response angle θ. The angle is plotted as a function of wave frequency and gyricity, which can be seen in figure 7.11.

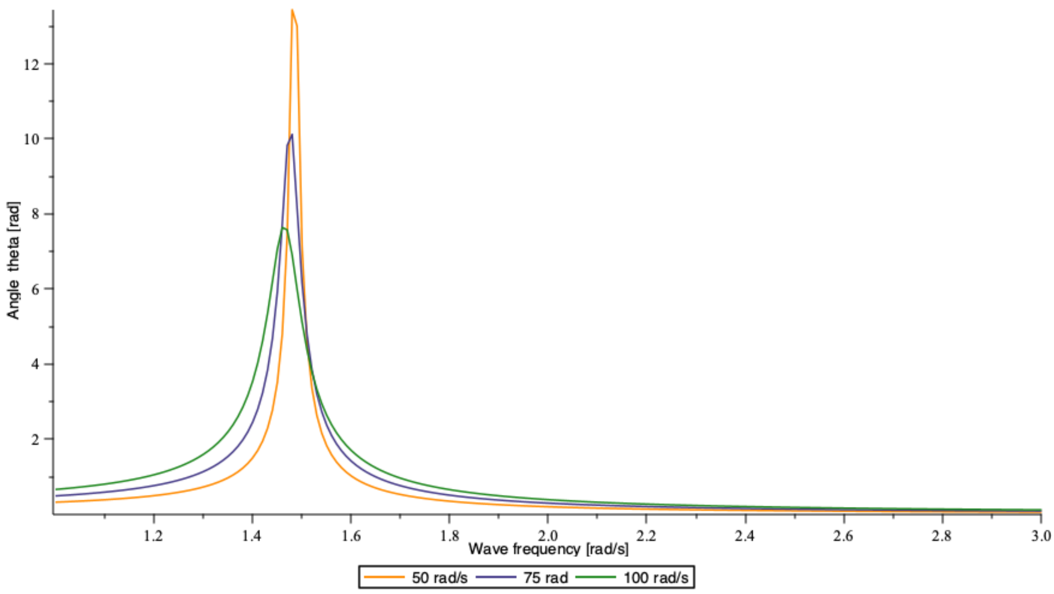

Figure 7.11: θ frequency response plot

In general, and especially around the natural frequency, large rotations are observed. The assumption of small angles, and the linearisation that follows, can be questioned based on these results. The linearisation due to small angles for $sin(\theta) = \theta$ is visualized in figure 7.12a. In this figure it can be seen that for small angles the resulting values are close enough to be considered equal.

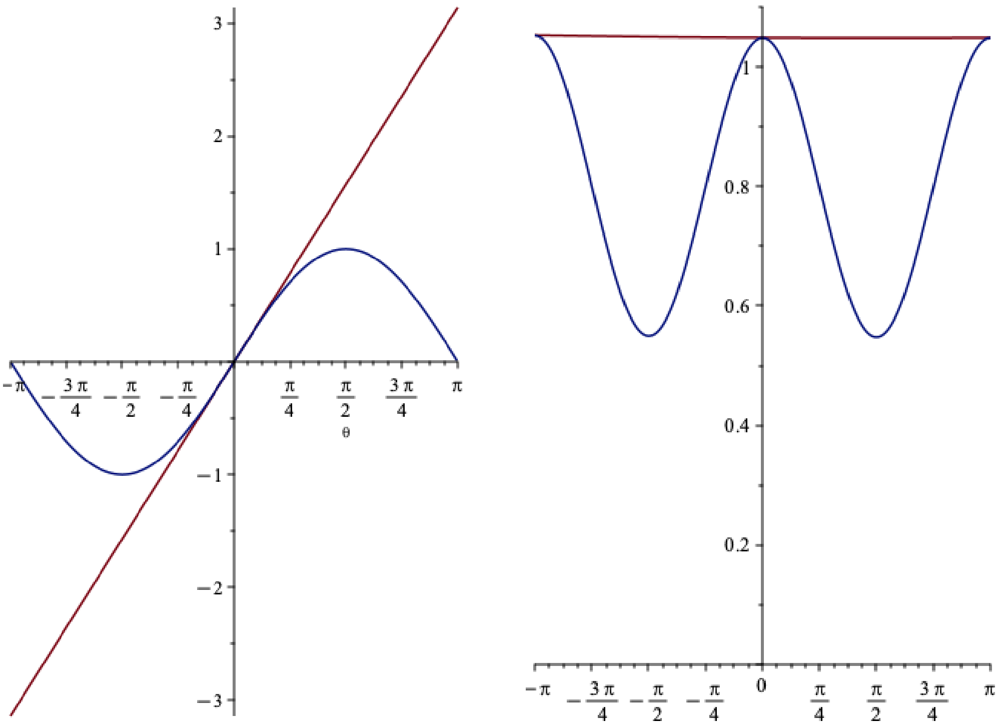

(a) $sin(\theta) = \theta$ **(b)** Gyrostabiliser equation of motion

Figure 7.12: Visualization of linearisation

Figure 7.12b presents the normalized values of the linearised and non-linearised angles, θ, from the Lagrangian in equation 6.10, where the horizontal line represents the and linearised equation. The linearisation is valid only for angles near -π, 0, and π. Consequently, the effectiveness of the gyrostabiliser in enhancing the system's overall stability may be overestimated when relying on this linearisation. To accurately assess this effect, the non-linearised Lagrangian should be utilized to solve the system in the time domain. This solution can then be compared with the frequency-domain solution provided in this study.

8 Conclusions and Recommendations

This chapter presents the main conclusions derived from the research conducted. Following this, the limitations of the analysis are discussed, and recommendations for future research are provided.

8.1. Conclusions

The conclusions are split up into the two main parts of this research. Here, the two main research questions given in section 1.2 will be answered.

8.1.1. Lighter topside

The worldwide demand for offshore renewable wind energy has experienced an exponential growth, driven by the need for clean energy and global CO2 reduction goals. To support this growth, the industry must focus on producing more efficient, reliable, and cost-effective turbines, thereby lowering the levelised cost of energy (LCOE). One innovative approach is the Delft Offshore Turbine (DOT) hydraulic pump, which replaces traditional, heavier components such as the gearbox and generator, reducing the weight of the turbine's topside by up to 50%.

In this research, two bottom founded support structures for a designated locations in the North-Sea are designed. One with the conventional topside mass, and one with the lighter DOT topside mass. For comparison reasons, the tower design is kept the same for both designs. The research is set up to answer the question:

"What are the effects of a lighter topside on the support structure of a bottom founded offshore wind turbine?"

As main conclusion, the lighter topside reduces the steel requirements for the monopile, with the ultimate limit state (ULS) check becoming the primary constraint. Interestingly, for the conventional turbine, the limiting factor is the target natural frequency. The parameters of both designs are repeated in table 8.1. A reduction in **13% steel** is achieved in overall steel usage for the lighter topside.

Throughout the design process for both cases, the same optimization method was applied. First, the diameter of the monopile was increased, followed by the wall thickness.

Table 8.1: Parameters support structure

Parameter	Symbol	DOT	Conventional	Unit
Tower length	L_T	65	65	m
Slipjoint length	L_{SJ}	9	9	m
Monopile length	L_{MP}	31	31	m
Embedded length	L_{emb}	18	18	m
Diameter tower top	$D_{T,t}$	3	3	m
Diameter tower bottom	$D_{T,b}$	5.2	5.2	m
Diameter slipjoint top	$D_{SJ,t}$	5.2	5.2	m
Diameter slipjoint bottom	$D_{SJ,b}$	5.29	5.44	m
Diameter monopile	D_{MP}	5.29	5.44	m
Wall thickness tower	t_t	30	30	mm
Wall thickness slipjoint	t_{SJ}	60	60	mm
Wall thickness monopile	t_{MP}	50	58	mm
Slipjoint angle	α_{SJ}	0.6	1.5	°

The results of the ULS check are given in table 8.2. Both designs pass the test, where the DOT design unit check comes close to the limit. Therefore, it is concluded that the current design is limited by the ULS Von Mises yield check.

Table 8.2: Results ULS analysis. **with respect to mudline*

	DOT	conventional
Von Mises yield check [-]	0.967	0.821
Max. Von Mises yield location* [m]	-1.2	-1.2
Global buckling check [-]	0.882	0.779
Max. global buckling location* [m]	-0.3	-0.3

The results of the Fatigue Limit State (FLS) are given in tables 8.3. The checks are performed only for a unidirectional wind profile. This means that only vibrations in the for-aft direction are considered and no wind-wave misalignment is included in the results. This way, all bending stress cycles accumulate at one point in the structure, which is a conservative approach. Not taking into account wind-wave misalignment is therefore allowable.

Table 8.3: Results FLS analysis

S-N curve	DOT	Conventional
B2	0.35	0.23
C	1.22	0.78
C1	2.11	1.35
C2	3.72	2.39

The model developed in this research, despite its simplified nature, is currently focused on altering only the monopile dimensions while keeping the tower unchanged. This is done for two reasons: to clearly visualize the relation between topside mass and support structure dimensions and for production reasons coming from Delft Offshore Turbine. However, this model has the potential to be extended to optimize the entire support structure of the turbine, including both the tower and the monopile, to achieve the most efficient design.

8.1.2. Gyrostabiliser

In this research, a simplified dynamic model representing the support structure of a bottom-founded offshore wind turbine is developed. A gyrostabiliser is integrated into the nacelle to study its effect on the system's dynamics. The model aims to capture the steady-state response to wave forcing, which is the primary contributor to fatigue in offshore structures. The dynamics of the system are analyzed in the frequency domain to provide insights into how the gyrostabiliser influences the overall stability and fatigue resistance of the structure. This model is set up to answer the research question:

"How effective are gyroscopic dampers in reducing wave-induced vibrations in bottom founded offshore wind turbines?"

Due to the minimally damped side-to-side motion of the topside, we aim to reduce the motion in this direction. The investigation into the use of a gyrostabiliser for reducing side-to-side displacement, and thus stresses, in offshore structures reveals mixed outcomes. Initially, it was found that a passive gyrostabiliser without a damper does not significantly reduce these stresses, contrary to expectations. However, it does show potential as a frequency-skipping tool. By varying the disk gyricity the natural frequency of the system changes. By adjusting the spinning velocity of the disk based on the incoming wave frequency, making it an active system, the overall response can be improved.

When a rotational damper and spring are incorporated into the system, the gyrostabiliser becomes more effective. In this configuration, the passive system successfully dampens both displacements and bending stresses. This reduction of bending stress at the mudline, for a particular configuration, is shown in figure 8.1. Tuning the system can easily be done by altering the disk's spinning velocity, offering flexibility in adapting to different conditions. The optimal gyricity of the disk depends on several parameters, including its mass, radius, and the values of the rotational damping and spring.

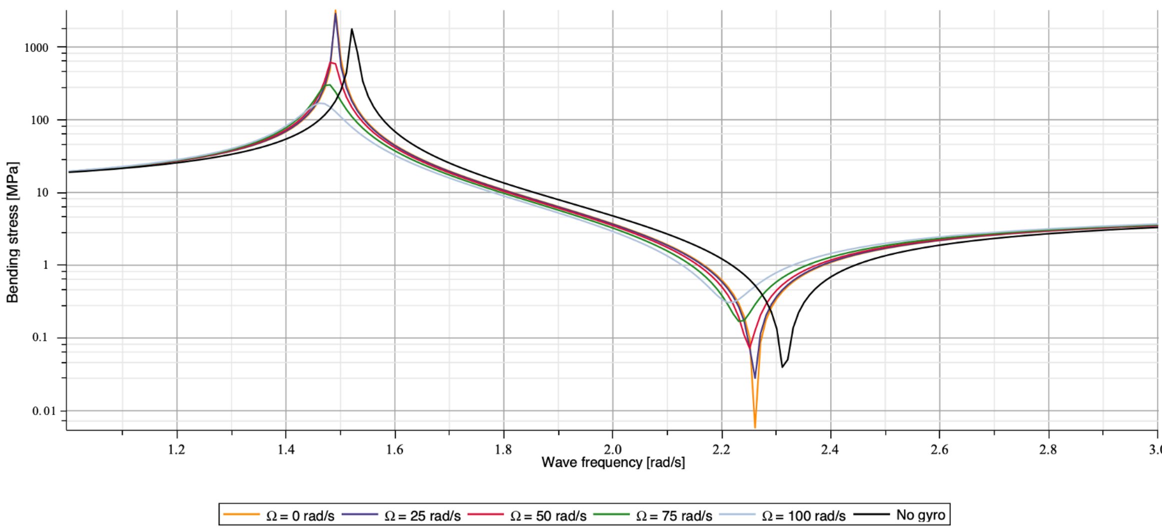

Figure 8.1: Stress Frequency Response Function gyricity alteration damped 7000kg gyrostabiliser| side-to-side direction

Reducing side-to-side vibrations has further advantages, particularly regarding the incoming wind angle. By stabilizing the platform, the apparent wind angle experienced by the blades is optimized, potentially enhancing the efficiency of energy conversion. This indicates that a properly tuned gyrostabiliser can contribute to both structural integrity and performance in offshore wind turbines.

When the gyrostabiliser is compared to conventional passive mass dampers (PMDs), several advantages and disadvantages emerge. gyrostabilisers are typically lighter and more compact than PMDs, making them easier to integrate into existing designs. Their ability to be tuned via the rotational speed of the disk adds a level of adaptability not present in PMDs. Here, the tuning is done by altering the structural parameters of the damping system. However, this tuning comes with the risk of hitting the precession frequency, which could result in increased displacement rather than stabilization. Moreover, gyrostabilisers are mechanically more complex than PMDs, leading to higher maintenance requirements.

8.2. Recommendations

To build upon the findings of this research, several areas warrant further investigation. First, the methodology for frequency skipping using the gyrostabiliser should be explored in more depth. This globally involves the process: (1) measuring the incoming wave frequency, (2) determining the required rotational velocity of the gyrostabiliser disk, and (3) adjusting the disk's spin rate accordingly. An important aspect to consider here is the speed at which the disk can be accelerated to the desired rotational velocity. Understanding the time frame and limitations of this acceleration is crucial for implementing an effective frequency-skipping strategy.

Second, the energy consumption associated with this sequence also needs to be evaluated. It is essential to quantify the energy requirements for adjusting the disk's rotational velocity in real-time and assess whether this approach is feasible for practical application. Additionally, the overall complexity and financial implications of this technique should be analyzed. The potential benefits, such as extended structural lifetime due to reduced bending stress at critical locations or the possibility of using less expensive steel, as indicated in table 8.3, should be weighed against the costs involved.

Third, exploring the application of this gyrostabilization technique for floating offshore wind turbines is also recommended. Floating structures have different - and often more extreme - dynamic characteristics compared to bottom founded turbines. The effectiveness of the gyrostabiliser in such scenarios could lead to further innovations in wind turbine design. Moreover, the effects of bottom-founded offshore wind turbines in deeper waters should be investigated. These turbines experience larger forces and internal moments, potentially amplifying the benefits of gyrostabilization in enhancing structural resilience.

Fourth, to enhance the gyrostabiliser's effectiveness further, the implementation of a second gyrostabiliser is suggested. A dual gyrostabiliser setup could not only reduce vibrations in the side-to-side direction but also address vibrations in the fore-aft direction. This comprehensive stabilization approach may significantly improve the structural dynamics and efficiency of offshore wind turbines.

Lastly, solving the system in the time domain is recommended to capture the transient response. This approach would allow for a more accurate assessment of the validity of linearisation, applied due the assumption of small vibrations, on the overall accuracy of the model.

References

[1] International Renewable Energy Agency. *World Energy Transitions Outlook 2022: 1.5°C Pathway*. 2022. ISBN: 9789292604295. URL: `www.irena.org`.

[2] International Energy Agency. *Offshore Wind Outlook 2019: World Energy Outlook Special Report*. Tech. rep. 2019. URL: `www.iea.org/t&c/`.

[3] energydata.info. *Global Wind Atlas*. 2021.

[4] *SJOR-PUBLIC REPORT TSE HE 2016 Title: Slip Joint Offshore Research*.

[5] Tyler Stehly, Philipp Beiter, and Patrick Duffy. *Cost of Wind Energy Review*. Tech. rep. 2019. URL: `www.nrel.gov/publications.`.

[6] W. Kooloos. *Limiting mechanisms for the torque density of wind turbine drivetrains*. Tech. rep. 2019.

[7] Mehdi Soleymani and Mahdi Norouzi. "Active gyroscopic stabilizer to mitigate vibration in a multimegawatt wind turbine". In: *Wind Energy* 24.7 (July 2021), pp. 720–736. ISSN: 10991824. DOI: `10.1002/we.2599`.

[8] DNV GL. *STANDARD DNV GL AS Loads and site conditions for wind turbines*. Tech. rep. 2016. URL: `http://www.dnvgl.com`.

[9] IEC. *Wind energy generation systems-Part 3-1: Design requirements for fixed offshore wind turbines*. Tech. rep. 2019.

[10] IEC. *Wind turbines-Part 1: Design requirements*. Tech. rep. 2005. URL: `www.barghnews.com`.

[11] Fugro. *Netherlands Enterprise Agency*. URL: `https://offshorewind.rvo.nl/cms/view/3ce5f11f-d39c-4de4-a877-6daf6b945c5c/wind-en-water`.

[12] Jung Tae Lee, Hyun Goo Kim, Yong Heack Kang, and Jin Young Kim. "Determining the optimized hub height of wind turbine using the wind resource map of South Korea". In: *Energies* 12.15 (July 2019). ISSN: 19961073. DOI: `10.3390/en12152949`.

[13] "[15200450 - Journal of Applied Meteorology and Climatology] Determining the Power-Law Wind-Profile Exponent under Near-Neutral Stability Conditions at Sea". In: ().

[14] Det Norske Veritas. *DET NORSKE VERITAS AS Design of Offshore Wind Turbine Structures*. Tech. rep. 2014. URL: `www.dnvgl.com.`.

[15] L. Arany, S. Bhattacharya, S. Adhikari, S. J. Hogan, and J. H.G. Macdonald. "An analytical model to predict the natural frequency of offshore wind turbines on three-spring flexible foundations using two different beam models". In: *Soil Dynamics and Earthquake Engineering* 74 (July 2015), pp. 40–45. ISSN: 02677261. DOI: `10.1016/j.soildyn.2015.03.007`.

[16] H.G. Poulos and E.H. Davis. "Piles Foundation Analysis And Design". In: *Rainbow Bridge Book Co.* (1980).

[17] K Terzaghi. "Coefficients Of Subgrade Reaction". In: *Geotechnique* 5.4 (1955), pp. 41–50.

[18] Laszlo Arany, S. Bhattacharya, John Macdonald, and S. J. Hogan. "Design of monopiles for offshore wind turbines in 10 steps". In: *Soil Dynamics and Earthquake Engineering* 92 (Jan. 2017), pp. 126–152. ISSN: 02677261. DOI: `10.1016/j.soildyn.2016.09.024`.

[19] Saleh Jalbi, Masoud Shadlou, and Subhamoy Bhattacharya. "Practical Method to Estimate Foundation Stiffness for Design of Offshore Wind Turbines". In: *Wind Energy Engineering: A Handbook for Onshore and Offshore Wind Turbines*. Elsevier Inc., May 2017, pp. 329–352. ISBN: 9780128094297. DOI: `10.1016/B978-0-12-809451-8.00016-3`.

[20] Sebastiaan Paul Mulders, Tobias Gybel Hovgaard, Jacob Deleuran Grunnet, and Jan-Willem van Wingerden. "Preventing wind turbine tower natural frequency excitation with a quasi-LPV model predictive control scheme". In: (May 2019). DOI: 10.1002/we.2447. URL: http://arxiv.org/abs/1905.10158%20http://dx.doi.org/10.1002/we.2447.

[21] Peter Frohboese and Christian GL Schmuck Garrad Hassan. *THRUST COEFFICIENTS USED FOR ESTIMATION OF WAKE EFFECTS FOR FATIGUE LOAD CALCULATION*. Tech. rep. 2010.

[22] J R Morison, M P O'brien, J W Johnson, and S A Schaaf. *THE FORCE EXERTED BY SURF'ACE W AVES ON PILES THE FORCE EXERTED BY SURF ACE WAVES ON PILES*. Tech. rep. 1950. URL: http://onepetro.org/JPT/article-pdf/2/05/149/2238818/spe-950149-g.pdf/1.

[23] Swagata Bisoi and Sumanta Haldar. "Dynamic analysis of offshore wind turbine in clay considering soil-monopile-tower interaction". In: *Soil Dynamics and Earthquake Engineering* 63 (2014), pp. 19–35. ISSN: 02677261. DOI: 10.1016/j.soildyn.2014.03.006.

[24] Leon Harland and Jan Vughts. "Analytical expression for the first natural period of a stepped tower". In: (1996).

[25] Jian Hong Wan, Rui Bai, Xue You Li, and Si Wei Liu. "Natural Frequency Analysis of Monopile Supported Offshore Wind Turbines Using Unified Beam-Column Element Model". In: *Journal of Marine Science and Engineering* 11.3 (Mar. 2023). ISSN: 20771312. DOI: 10.3390/jmse11030628.

[26] Djillali Amar Bouzid, Subhamoy Bhattacharya, and Lalahoum Otsmane. "Assessment of natural frequency of installed offshore wind turbines using nonlinear finite element model considering soil-monopile interaction". In: *Journal of Rock Mechanics and Geotechnical Engineering* 10.2 (Apr. 2018), pp. 333–346. ISSN: 16747755. DOI: 10.1016/j.jrmge.2017.11.010.

[27] Eurocode 3. *EN 1993-1-1: Eurocode 3: Design of steel structures - Part 1-1: General rules and rules for buildings*. 2005.

[28] DNV AS. *DNV-ST-0126 Support structures for wind turbines*. Tech. rep. 2021.

[29] DNV GL. *OFFSHORE STANDARD DNV GL AS Design of offshore steel structures, general-LRFD method*. 2015. URL: www.dnvgl.com..

[30] DNV AS. *OFFSHORE STANDARDS Metallic materials*. Tech. rep. 2023.

[31] V. V. (Vladimir Vasil'evich) Bolotin. *Mechanics of fatigue*. CRC Press, 1999, p. 463. ISBN: 0849396638.

[32] DNV AS. *RECOMMENDED PRACTICE Fatigue design of offshore steel structures*. Tech. rep. 2019.

[33] DNV AS. *OFFSHORE STANDARDS Structural design of offshore units*. Tech. rep. 2024.

[34] Fabian Vorpahl, Hans-Georg Moll, and Hans-Gerd Busmann. *Dynamics of Support Structures for Offshore Wind Turbines in Fully-coupled Simulations-Influence of Water Added Mass on Jacket Mode Shapes, Natural Frequencies and Loads*. Tech. rep. 2010. URL: https://www.researchgate.net/publication/267711968.

[35] A.R.M. Wolfert. "Wave effects in one-dimensional elastic systems interacting with moving objects". In: (1999).

[36] Robert Fontecha, Frank Kemper, and Markus Feldmann. "On the determination of the aerodynamic damping of wind turbines using the forced oscillations method in wind tunnel experiments". In: *Energies* 12.12 (2019). ISSN: 19961073. DOI: 10.3390/en12122452.

[37] RVO. *F-1*. Tech. rep.

[38] Lilin Wang, Lizhong Wang, and Yi Hong. "Mitigation of side-to-side vibration of a 10MW monopile offshore wind turbine under misaligned wind and wave conditions by an active torque control". In: *Journal of Sound and Vibration* 574 (Mar. 2024). ISSN: 10958568. DOI: 10.1016/j.jsv.2023.118225.

[39] E. A. Bossanyi. "Individual Blade Pitch Control for Load Reduction". In: *Wind Energy* 6.2 (Apr. 2003), pp. 119–128. ISSN: 1095-4244. DOI: 10.1002/we.76.

[40] Zili Zhang, Søren R.K. Nielsen, Frede Blaabjerg, and Dao Zhou. "Dynamics and control of lateral tower vibrations in offshore wind turbines by means of active generator torque". In: *Energies* 7.11 (2014), pp. 7746–7772. ISSN: 19961073. DOI: 10.3390/en7117746.

[41] Gordon M. Stewart and Matthew A. Lackner. “The impact of passive tuned mass dampers and wind-wave misalignment on offshore wind turbine loads”. In: *Engineering Structures* 73 (Aug. 2014), pp. 54–61. ISSN: 01410296. DOI: 10.1016/j.engstruct.2014.04.045.

[42] Xin Tong, Xiaowei Zhao, and Shi Zhao. “Load reduction of a monopile wind turbine tower using optimal tuned mass dampers”. In: *International Journal of Control* 90.7 (July 2017), pp. 1283–1298. ISSN: 13665820. DOI: 10.1080/00207179.2015.1124143.

[43] Matthew A. Lackner and Mario A. Rotea. “Passive structural control of offshore wind turbines”. In: *Wind Energy* 14.3 (Apr. 2011), pp. 373–388. ISSN: 10954244. DOI: 10.1002/we.426.

[44] J M Jonkman. *Dynamics Modeling and Loads Analysis of an Offshore Floating Wind Turbine*. Tech. rep. 2007. URL: http://www.osti.gov/bridge.

[45] Nicholas C. Townsend and Ramanand A. Shenoi. *Gyrostabilizer vehicular technology*. 2011. DOI: 10.1115/1.4004837.

[46] Jörg Friedrich Wagner. *From Bohnenberger’s Machine to Integrated Navigation Systems, 200 Years of Inertial Navigation*. Tech. rep. 2005. URL: https://www.researchgate.net/publication/239922979.

[47] Masaaki Yamadal, Hiroto Higashiyama, Masao Namikill, Yukihiko Kazacy, and Kiyoshi Uesu·. *ACTIVE VIBRATION CONTROL SYSTEM USING GYRO-STABILIZER*. Tech. rep. 1996.

[48] Samuel J Ling, Jeff Sanny, and Moebs William. *University Physics Volume 1*. Tech. rep. OpenStax, 2021.

A

Derivation of critical wave loads

In this appendix the derivation from the water surface elevation to the critical wave loads acting on the substructure is given [8].

The drag force and inertia force of the wave per unit length give the wave force per unit length. This equation is given in A.1, where C_D and C_m are the drag and inertia coefficient, respectively. And ρ_w is the density of the seawater at the site.

$$dF_{wave}(z,t) = dF_D(z,t) + dF_I(z,t) = \frac{1}{2}\rho_w D_S C_D w(z,t)|w(z,t)| + C_m \rho_w A_S \dot{w}(z,t) \tag{A.1}$$

To obtain the total drag and inertia force, we integrate over the full submerged length. The moment of the wave around the seabed is then easily derived.

$$F_{\text{wave}}(t) = \int_{-S}^{\eta} dF_D dz + \int_{-S}^{\eta} dF_I dz \tag{A.2}$$

$$M_{\text{wave}}(t) = \int_{-S}^{\eta} dF_D(S)\,dz + \int_{-S}^{\eta} dF_I(S)\,dz \tag{A.3}$$

The maxima for the drag and inertia induced wave loads occur at different times, hence we determine them separately. The peak load for the drag occurs when $t = T_S/4$ and $\eta = H_m/2$. Contrary, the peak load for the inertia governed load occurs at $t = 0$ and $\eta = 0$. Filling in these time-instances and performing the integration, the equations for the drag force and moment then become:

$$F_{D,\max} = \frac{1}{2}\rho_w D_S C_D \frac{\pi^2 H_S^2}{T_S^2 \sinh(kS)} P_D(k,S,\eta) \tag{A.4}$$

$$M_{D,\max} = \frac{1}{2}\rho_w D_S C_D \frac{\pi^2 H_S^2}{T_S^2 \sinh(kS)} Q_D(k,S,\eta) \tag{A.5}$$

Where P_D and Q_D are defined in A.6 and A.7 and are both functions of the wave number, water depth and wave elevation at the considered instant of the maximum load.

$$P_D(k,S,\eta) = \frac{e^{2k(S+\eta)} - e^{-2k(S+\eta)}}{8k} + \frac{S+\eta}{2} \tag{A.6}$$

$$Q_D(k,S,\eta) = \left(\frac{S+\eta}{8k} - \frac{1}{16k^2}\right)e^{2k(S+\eta)} - \left(\frac{S+\eta}{8k} + \frac{1}{16k^2}\right)e^{-2k(S+\eta)} + \left(\frac{S+\eta}{2}\right)^2 + \frac{1}{8k^2} \tag{A.7}$$

The same holds for the inertia governed loads:

$$F_{I,\max} = \frac{1}{2}\rho_w C_m D_S^2 \frac{\pi^3 H_S}{T_S^2 \sinh(kS)} P_I(k,S,\eta) \tag{A.8}$$

$$M_{I,\max} = \frac{1}{2}\rho_w C_m D_S^2 \frac{\pi^3 H_S}{T_S^2 \sinh(kS)} Q_I(k,S,\eta) \tag{A.9}$$

$$P_I(k,S,\eta) = \frac{\sinh(k(S+\eta))}{k} \tag{A.10}$$

$$Q_I(k,S,\eta) = \left(\frac{S+n}{2k} - \frac{1}{2k^2}\right)e^{k(S+\eta)} - \left(\frac{S+\eta}{2k} - \frac{1}{2k^2}\right)e^{-k(S+\eta)} + \frac{1}{k^2} \tag{A.11}$$

Finally, the drag and inertia coefficient can be determined. These are generally functions of the Reynolds number, the Keulegan-Carpenter number and the relevant roughness.

$$C_D = C_{DS} * \psi(C_{DS,KC}) \tag{A.12}$$

Where the drag coefficient for steady-state flow C_{DS} may be taken as

$$C_{DS} = \begin{cases} 0.65 & \text{for } k/D < 10^{-4} \text{ (smooth)} \\ \frac{29+4\log_{10}(k/D)}{20} & \text{for } 10^{-4} < k/D < 10^{-2} \\ 1.05 & \text{for } k/D > 10^{-2} \text{ (rough)} \end{cases} \tag{A.13}$$

Due to marine growth, we take $k = 0.02$. The wake amplification factor ψ in equation A.13 can be determined by looking at the curves in figure A.1. The Keulegan-Carpenter number, for deep water, can be gives as

$$KC = \pi * \frac{H}{D_{mp}} \tag{A.14}$$

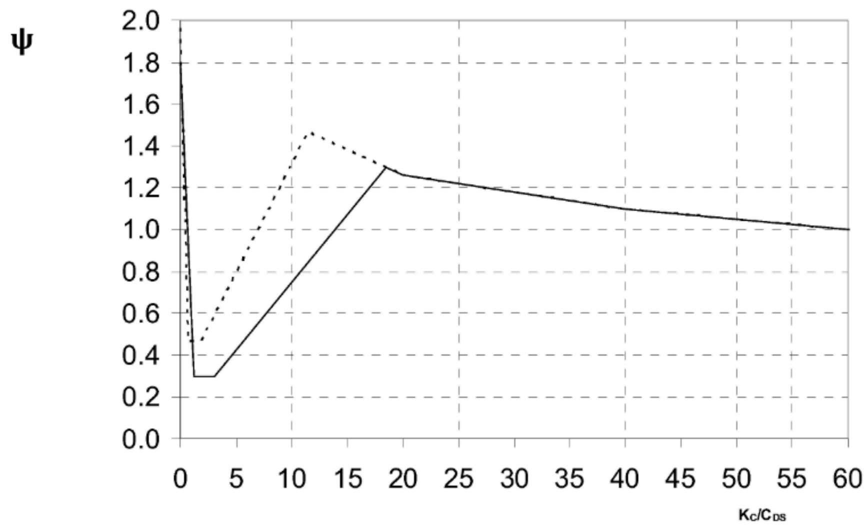

Figure A.1: Wake amplification factor for smooth (solid line) and rough (dotted line) roughness

The loads of relevant wave scenarios are given in table 3.1.

B
Derivation of rotational matrix

This appendix shows the derivation of the rotational matrix given in equation 6.6.

The goal is to find the rotational matrix to go from the global coordinate system to the fixed coordinate system of the body. In this way, we can multiply the simply postition vector in the body fixed with the rotational matrix, to find the postition vector in the desired global coordinate system. The rotations of freedom from the disk are: 1) the rotation around the x-axis with angle θ, 2) the rotation around the y-axis with angle ψ and 3) the rotation around the z-axis with angle η. To obtain the total rotational matrix, the rotation matrices around the 3 degrees of freedom are multiplied.

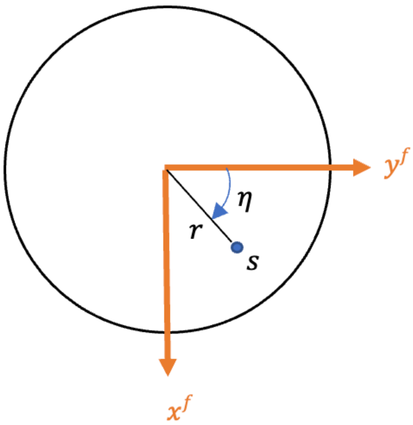

Figure B.1: Topview of flywheel

Rotation matrix from the x'-frame to the global coordinate system for an angle θ as depicted in figure B.1:

$$Rot_\theta = \begin{bmatrix} 1 & 0 & 0 \\ 0 & cos(\theta) & -sin(\theta) \\ 0 & sin(\theta) & cos(\theta) \end{bmatrix} \tag{B.1}$$

Rotation matrix from the y''-frame to the y'-frame for an angle ψ as depicted in figure B.1:

$$Rot_\psi = \begin{bmatrix} cos(\psi) & 0 & sin(\psi) \\ 0 & 1 & 0 \\ -sin(\psi) & 0 & cos(\psi) \end{bmatrix} \tag{B.2}$$

Rotation matrix from the z'''-frame to the z''-frame, for an angle η as depicted in figure B.1:

$$Rot_\eta = \begin{bmatrix} cos(\eta) & -sin(\eta) & 0 \\ sin(\eta) & cos(\eta) & 0 \\ 0 & 0 & 1 \end{bmatrix} \tag{B.3}$$

To obtain the total rotational matrix we apply:

$$Rot_{tot} = Rot_\eta \cdot Rot_\psi \cdot Rot_\theta \tag{B.4}$$

to become:

$$\begin{bmatrix} \cos(\eta)\cos(\psi) & -\sin(\eta)\cos(\theta) + \cos(\eta)\sin(\psi)\sin(\theta) & \sin(\eta)\sin(\theta) + \cos(\eta)\sin(\psi)\cos(\theta) \\ \sin(\eta)\cos(\psi) & \cos(\eta)\cos(\theta) + \sin(\eta)\sin(\psi)\sin(\theta) & -\cos(\eta)\sin(\theta) + \sin(\eta)\sin(\psi)\cos(\theta) \\ -\sin(\psi) & \cos(\psi)\sin(\theta) & \cos(\psi)\cos(\theta) \end{bmatrix} \tag{B.5}$$